Integrated vertical modulator onto VCSEL for ultra high speed optical interconnects

Lucas Laplanche

THÈSE

En vue de l'obtention du
DOCTORAT DE L'UNIVERSITÉ DE TOULOUSE

Délivré par l'Université Toulouse 3 - Paul Sabatier

Présentée et soutenue par

Lucas LAPLANCHE

Le 21 décembre 2023

Modulateur vertical intégré à un VCSEL pour les interconnexions optiques ultra-rapides

---

Ecole doctorale : **GEETS - Génie Electrique Electronique,Télécommunications et Santé : du système au nanosystème**

Spécialité : **Photonique et Systèmes Optoélectroniques**

Unité de recherche :
LAAS - Laboratoire d'Analyse et d'Architecture des Systèmes

Thèse dirigée par
Guilhem ALMUNEAU et Christophe VIALLON

Jury

M. Christophe PEUCHERET, Rapporteur
M. Laurent CERUTTI, Rapporteur
Mme Sophie BOUCHOULE, Examinatrice
M. Guilhem ALMUNEAU, Directeur de thèse
M. Christophe VIALLON, Co-directeur de thèse

Table

List of Acronyms

ACP Air Cushion Press

ALD Atomic Layer Deposition

BCB Benzocyclobutene

BtB Back-to-Back

CCPECVD Capacitive Coupled Plasma-Enhanced Chemical Vapor Deposition

DBR Distributed Bragg Reflector

DMT Discrete Multi-tone Transmission

DUT Device Under Test

EAM Electro-Absorption Modulator

FIB Focus-Ion Beam

FP Fabry–Pérot

FTIR Fourier-Transform Infrared Spectroscopy

GSG Ground-Signal-Ground

HPC High Performance Computer

ICMBE International Conference on Molecular Beam Epitaxy

ICPRIE Inductively Coupled Plasma Reactive Ion Etching

IoT Internet of Things

MBE Molecular Beam Epitaxy

MMF Multimode Fiber

NRZ-OOK Non-Return-to-Zero On-Off Keying

OBO On-Board Optical

PAM-4 4-level Pulse-Amplitude Modulation

PIC Photonic Integrated Circuit

PVD Physical Vapor Deposition

QAM-OFDM Quadrature Amplitude Modulation with Orthogonal Frequency-Division Multiplexing

QCSE Quantum-Confined Stark Effect

QW Quantum Well

RF Radio Frequency

SD-FEC Soft-Decision Forward Error Correction

SEM Scanning Electron Microscope

SNEAM Surface-Normal Electro-Absorption Modulator

TEM Transmission Electron Microscopy

TLM Transfer Length Method

TMM Transfer-Matrix Method

VCSEL Vertical Cavity Surface-Emitting Lasers

VNA Vector Network Analyzer

VOD Video On Demand

List of Figures

List of Tables

1 Abstract

The exponential increase in internet traffic has created an ongoing demand for faster data access and dedicated infrastructures, including data centers and high-performance computing (HPC) facilities. Due to challenges related to uptime, thermal considerations, cost constraints, and electrical efficiency, these infrastructures have widely adopted VCSELs, which possess a theoretical bandwidth limit of approximately 35GHz. To surpass this bandwidth limitation, we suggest utilizing an Electroabsorption modulator integrated onto a VCSEL. Electroabsorption modulators have a theoretical maximum bandwidth of approximately 100GHz, and integrating them with VCSELs offers the advantage of a single component for simplified implementation, addressing the specific constraints of data centers and HPCs. Initially, five distinct structures are designed using analytical simulations, considering optical behavior, charge carrier dynamics, and interactions between the optical cavities of the Electroabsorption Modulator (EAM) and the VCSEL to optimize the absorption contrast ratio. Subsequently, the device's fabrication has been reviewed and enhanced, particularly focusing on the steps involving epitaxy and oxide aperture. Finally, the setup for RF characterization has been refined to consider the high impedance of the device and accurately extract its transfer function. The structures grown by epitaxy all exhibit a Fabry-Perot resonance very close to the targeted 850nm, achieved through specific in-situ measurements. The VCSEL oxidation process results in a precise aperture of 2um, facilitated by in-situ monitoring. Finally, the EAM achieves a bandwidth of 47GHz, surpassing the previously recorded highest performance for an EAM-VCSEL (29GHz). The EAM-VCSEL demonstrates promising results, competing favorably with other technologies. Its inherent integration of light emission and optical absorption for data transmission facilitates easy implementation, particularly in areas where VCSELs are already established. Moreover, the insights presented in this thesis indicate significant untapped potential for further improvement and enhanced performance.

L'augmentation exponentielle du trafic Internet a créé une demande constante d'accès plus rapide aux données et d'infrastructures dédiées, y compris les centres de données et les installations de calcul à haute performance (HPC). En raison des défis liés au temps de fonctionnement, aux considérations thermiques, aux contraintes de coût et à l'efficacité électrique, ces infrastructures ont largement adopté les VCSEL, qui possèdent une limite de bande passante théorique d'environ 35 GHz. Pour dépasser cette limite de bande passante, nous proposons d'utiliser un modulateur d'électroabsorption intégré à un VCSEL. Les modulateurs d'électroabsorption ont une largeur de bande maximale théorique d'environ 100 GHz, et leur intégration à des VCSEL offre l'avantage d'un composant unique pour une mise en œuvre simplifiée, répondant aux contraintes spécifiques des centres de données et des HPC. Dans un premier temps, cinq structures distinctes sont conçues à l'aide de simulations analytiques, en tenant compte du comportement optique, de la dynamique des porteurs de charge et des interactions entre les cavités optiques du modulateur d'électro-absorption (EAM) et le VCSEL afin d'optimiser le rapport de contraste d'absorption. Ensuite, la fabrication du dispositif a été revue et améliorée, en se concentrant particulièrement sur les étapes impliquant l'épitaxie et l'ouverture de l'oxyde. Enfin, la configuration pour la caractérisation RF a été affinée pour tenir compte de l'impédance élevée du dispositif et extraire avec précision sa fonction de transfert. Les structures obtenues par épitaxie présentent toutes une résonance Fabry-Perot très proche des 850 nm visés, obtenue grâce à des mesures in situ spécifiques. Le processus d'oxydation du VCSEL permet d'obtenir une ouverture précise de 2um, facilitée par un contrôle in situ. Enfin, l'EAM atteint une largeur de bande de 47 GHz, surpassant la performance la plus élevée précédemment enregistrée pour un EAM-VCSEL (29 GHz). L'EAM-VCSEL démontre des résultats prometteurs, rivalisant favorablement avec d'autres technologies. Son intégration inhérente de l'émission de lumière et de l'absorption optique pour la transmission de données facilite la mise en œuvre, en particulier dans les domaines où les VCSEL sont déjà établis. En outre, les idées présentées dans cette thèse indiquent un potentiel inexploité important pour des améliorations supplémentaires et des performances accrues.

2 Introduction and context

The persistent need for faster data access has been driving the growth of massive data centers and the development of delivery infrastructure to meet increasing demands. The growth of internet traffic has surged by a magnitude of 10^7, from 1995 to 2020 as it can be seen in figure 1. From 2018 to 2023, it has been estimated that the population with internet access has increased by 35%, the number of devices connected to IP networks went from 2.4 to 3.6 per capita, the share of machine to machine connections grew from 33% to 50% to reach 14.7 billion devices, and the fixed broadband speed more than doubled [1]. Moreover, the emergence of $4K$ television broadcasts, video conferences, remote working, and the increasing amount of gaming and streaming users are a driving force to the global bandwidth growth [2]. Since 2005 the global internet traffic doubled every two years, while the single channel line rates doubled every four years [2]. This difference between supply and demand leads to a greater need for additional interconnects to fulfill the demand gap.

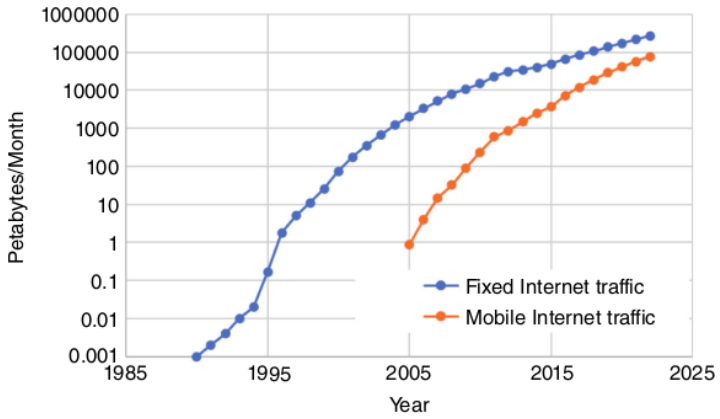

Figure 1: Fixed and mobile traffic in petabytes per month (from [2]).

The most crucial data communication sectors where optical transceivers are involved are datacenters using High-Performance Computers (HPC) and telecoms. In 2021, the Yole Développement group forecasted [3] that the optical transceiver revenue in datacoms will grow from $9.6 in 2020, to $15.1 in 2026, with a compound annual growth rate of 19% for the datacoms. The challenges met by HPC and datacenters led to the mass adoption of Vertical Cavity Surface-Emitting Lasers (VCSEL) as a solution. To date, to address the challenges of advancing data rates, industrial and research groups are increasingly exploring combinations of VCSELs with complex encoding formats or alternative technologies. To present the topic, and legitimize our solution, this introduction chapter is organized as follow:

The first section presents the main sector experiencing an increase of the data growth (datacenters and HPCs), and why their technical constraints led to the adoption of

VCSELs as a solution, and what constrains must be taken into account when researching an alternative solution.

The second section presents the latest development of VCSELs in direct modulation with different encoding format as a solution for data transmission, and their limits.

The third section presents the integration of a Electro-Absorption Modulators (EAM) within the VCSEL vertical structure as an alternative, and how they can outperform the limitations of direct modulation VCSELs.

The fourth section presents the physics behind the operation of VCSELs and EAMs, including the principles of the absorption phenomena and the actuation by an applied electric field.

2.1 Data centers and High-Performance Computers

A data center is a centralized facility that houses and manages computer systems, networking equipment, and storage systems to store, process, and distribute large volumes of data for various purposes. They have been built worldwide in response to the bandwidth requirements generated by applications like e-commerce, video-on-demand (VOD), video conferencing, data storage, and the Internet of Things (IoT). Their size can range from a small dedicated room in an office to a whole building of several hundreds of thousands square meters. Currently the ten biggest data centers account for a total of $2.3Mm^2$ filled with racks, switches, and optical fibers and interconnects. Several constraints are to take into account when building or managing a datacenter such as the cost, the uptime, the cooling, and cable management. Since the cost difference between optical and electrical interconnects has eroded in the past decades, and fiber optic cabling offer more flexibility, reduction in size and weight, and less electromagnetic interferences, optical interconnects have been widely adopted in data centers. Moreover, the reduction of congestion offered by the less cumbersome fiber cable provides more volume for airflow, and thus allow for better cooling solutions.

HPCs are networking clusters made out of multiple parallel processors, requiring very fast interconnects. They are typically used for high-level simulation such as car crashes, molecular interaction for drug design, cosmology, and cloud-computing, where the need for high-performance parallelism is even more critical. In 2022, the HPC "Frontier", has achieved the exaflop for the first time (10^{18} floating-point operations per second) [4]. The adoption of optical interconnects for HPC since 2008 was primarily driven by three factors: the capacity to compactly integrate transceivers onto the processor and memory boards (using On-Board Optical (OBO) technology), the mechanical flexibility of optical fibers (which provides the same benefits previously explained in the case of data centers), and the fact that the total computing is limited by latency in transmitting the data between processors and memory. Since the connectivity bandwidth increases proportionally with the total processing capability, it is a rule of thumb that an HPC requires $1B/FLOP$ data rate, making the exaflop computer requiring approximately one million $100Gbit/s$ links. Around the world, data centers and HPC centers are believed to currently employ close to one billion VCSELs [5].

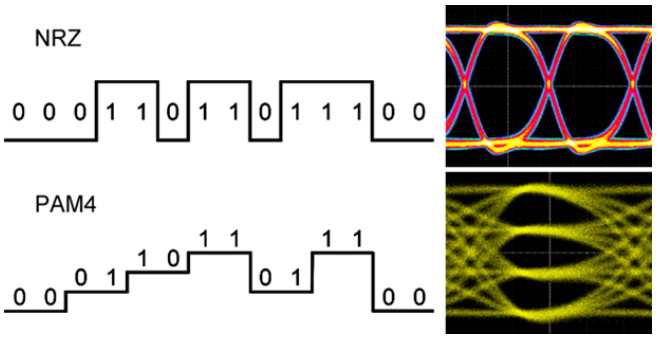

Figure 2: NRZ and PAM-4 encoding format diagram with their respective open-eye diagrams

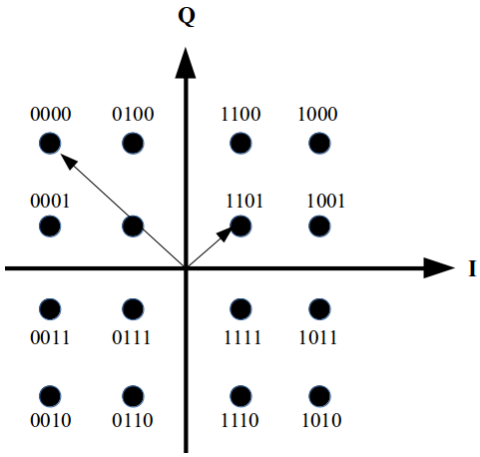

Figure 3: Graph representing the 16-QAM encoding format with example constellation points

2.2 Advancement of VCSEL for direct modulation applications

2.2.1 Encoding formats

When a VCSEL is directly modulated in order to transmit optical data from a current signal, several choices of data encoding are possible. Typically, with VCSELs for data communication, there are three common encoding methods [6]:

- NRZ-OOK: Non-Return-to-Zero On-Off Keying is the standard logic signal format. The data is encoded with two logic levels with two light powers (figure 2). This is the most simple encoding strategy and can be used with a VCSEL by employing the simplest circuitry. It has the lowest spectral efficiency: typically $1bit/s/Hz$ in the case of pulse shaping.

- PAM-4: 4-level Pulse-Amplitude Modulation (figure 2). The data is encoded in the amplitude of a series of signal pulses with four different levels. PAM-N format (N being the modulation order) increases the spectral efficiency by a factor of $log_2(N)$ within the same allowable bandwidth, but requires a better Signal-to-Noise Ratio (SNR) than for other 2-levels formats in order for the transmission to keep being error-free. This can lead to a more complex driving circuitry than the NRZ-OOK format.

- QAM-OFDM: Quadrature Amplitude Modulation with Orthogonal Frequency-Division Multiplexing. In QAM, the data is encoded by Amplitude Modulation

(AM) on two carriers of the same frequency, but that are phase shifted from each other by 90° (Quadrature condition). The OFDM scheme implements the QAM on multiple carrier frequencies. The M-QAM-OFDM is a much more complex encoding format than NRZ-OOK or PAM-N, but it exhibits a larger spectral efficiency (up to $log_2(M)bit/s/Hz$), and typically requires complex driving circuitry such as nonlinear equalizers, complex digital-analog converters,...

2.2.2 VCSELs using NRZ-OOK encoding

NRZ-OOK was the earliest data encoding format applied to VCSELs for data communication. It is still used in most of the articles about VCSEL characterization since it provides a simple and universal baseline for performance comparison among VCSELs, unlike other formats that might rely on varying circuitry and make the comparison biased. In 2008, Westbergh et al. [7] achieved 25 $Gbit/s$ with a large oxide aperture VCSEL in NRZ-OOK. A year later, Blokhin et al. [8] realized an oxide-confined VCSEL with a smaller aperture that achieved $40Gbit/s$. Beginning in 2010, with the increasing implementation of optical interconnects in datacenters and HPCs, reports on data transmission focused not only on the back-to-back (BtB) but also on various lengths of multimode fiber (MMF) conditions. In 2011, Moser et al. [9] got $25Gbit/s$ with an oxide confined VCSEL over $100m$ of OM3 MMF. Westbergh's group [10] demonstrated a modulation bandwidth of $28GHz$ with a $7\mu m$ oxide confined VCSEL, achieving an NRZ-OOK transmission of $47Gbit/s$ BtB, and $44Gbit/s$ over $50m$ of MMF. In 2013, the same goup [11] enhanced the impedance matching and the modulation efficiency of their previous configuration by including several aluminium layers with different oxide confined apertures, and reached $55Gbit/s$ in BtB and $43Gbit/s$ on $100m$ MMF. Finally, $80Gbit/s$ over $2m$ MMF and $72Gbit/s$ over $50m$ has been achieved by Chorchos et al. in 2020 [12].

In less than 15 years, the VCSEL in NRZ-OOK transmission has almost doubled its data rate. However the NRZ-OOK struggles reaching the $100Gbit/s$ cap because of its low spectral efficiency. Only two solutions can go beyond this data rate, either setting several VCSELs in an array to aggregate the whole data rate, or choosing a different encoding format such as PAM-4 or QAM-OFDM.

2.2.3 VCSELs using PAM-4 and QAM-OFDM encoding

A lot of different encoding formats allows to increase the spectral efficiency. In comparison to the NRZ-OOK, PAM-4 typically exhibits a doubled data rate, which unlocks the $100Gbit/s$ cap. Using PAM-4 with VCSELs trace back to 2011 with Szczerba et al., having achieved $30Gbit/s$ over $200m$ of MMF, and $25Gbit/s$ over $300m$ of MMF with an

oxide-confined VCSEL [13]. More recently (2020), Huawei Technologies Co. achieved $200Gbit/s$ over $100m$ of MMF with PAM-4 on a VCSEL using a nonlinear equalizer, PR signaling, and a noise cancellation module [14]. In 2021, Lo et al. reached $96Gbit/s$ in BtB and $70Gbit/s$ over $100m$ of MMF thanks to a pre-emphasis technique which compensates the amplitude degradation and the phase variation originating from the channel response [15].

With the development of 5G, the fifth-generation technology standard for broadband cellular networks, VCSELs became a potential choice to link the wired with the wireless access network. Indeed, several companies like Seoul Viosys [16] have started to provide VCSEL-based solutions as front-haul transmitters between the Distributed Unit and the 5G antennas where distance ranges from several hundreds of meters up to $20km$. Typically, the QAM-OFDM is choosen for this kind of emerging applications because of its very high spectral efficiency. Indeed, the achieved data rate for transmission with MMF can reach up to $100Gbit/s$ with a $20GHz$ bandwidth VCSEL. For instance, in 2021, IV-Systems [17] reached $224Gbit/s$ with a VCSEL with a bandwidth of only $30GHz$. They achieved this by employing Discrete Multi-tone Transmission (DMT), which involves dividing the signal into discrete subcarriers. Each of these subcarriers is subsequently modulated with QAM, and finally, soft-decision forward error correction (SD-FEC) is applied.

Complex driving circuitry implies an increase in cost, electrical consumption, generated heat and adds some bulkyness, which are critical parameters when it comes to the data center or HPC applications. Currently data-centers have steadily transitioned their data encoding format from NRZ-OOK towards PAM-4. Since M-QAM-OFDM has started to emerge in the wireless base stations, it might as well make its way to data centers and HPCs.

2.3 EAMs potential as an alternative solution

2.3.1 State-of-the-art of surface modulated EAMs

As already stated, the data rate reached with a VCSEL light source has consistently increased. The research on VCSEL now seems to trend towards metallic doping to improve the resistance, optimizing the capacitance through the oxide aperture, and sometimes upgrading the driving circuitry. Increasing the VCSEL bandwidth beyond $35GHz$ could not been demonstrated [6] [18]. In order to increase the data rate, two methods are available, either setting several VCSEL chips, or using a data encoding format with higher spectral efficiency.

In order to improve the data rate and go beyond the physical intrinsic limit of

VCSELs, one possibility is to separate the emission and the optical modulation as two distinct functions. While the VCSEL is used as a constant source of light emission, an Electro-Absorption Modulator (EAM) is used as a device dedicated to the optical modulation. EAMs have a much higher theoretical bandwidth than VCSELs [19], and require less driving power. However having two devices instead of one, and the requirement of optical alignement can still be seen as too cumbersome for the emerging optical data communications applications. This is why we propose a third approach with a device which separates the emission and modulation functions, but integrate them as one single component.

Surface-normal EAM (SNEAM) structures, also called asymetric Fabry-Perot EAMs, can transmit data by modulating the absorption of the light that passes through them using the Quantum-Confined Stark Effect (QCSE). The QCSE describes the variation of light absorption in a Quantum Well (QW) when it is biased by an electric field. The region where the QCSE happens typically has around 20 quantum wells, and is interposed between highly reflective DBRs. They are different to standard planar EAMs, as the incident light has to be quasi-perpendicular. They are designed to operate at the surface-normal direction, meaning that light enters and exits the device perpendicular to its surface, making them particularly suitable to work in pair with VCSELs.

Surface normal EAMs have several advantages over other types of modulators. First, their surface-normal operation simplifies the device packaging and integration into optical systems. They can be easily coupled with other components such as lasers, fibers, and detectors. Second, their compact size and low power consumption make them suitable for high-density integration in photonic integrated circuits (PICs). Finally, surface normal EAMs offer high modulation speed, making them useful for high-speed optical communication systems.

In 2014 Audet et al. demonstrated the first surface-normal $SiGe$ EAM fabricated entirely on standard silicon substrates [20]. Rather than trying to achieve the highest bandwidth, their focus was to make a device that could be integrated with CMOS circuitry. They reached a bandwidth of $3.5GHz$. Recently, in 2020, Iannone et al. demonstrated a $14GHz$ bandwidth in a packaged version of their SNEAM, and $65GHz$ with the unpackaged version [21]. With PAM4 modulation, over a fiber transmission of $23km$ they obtained a $44Gb/s$ rate, and $160Gb/s$ over $2km$. At the same time, Grillanda et al. achieved $25Gbit/s$ on their packaged SNEAMs and $107Gbit/s$ with the bare chip version [22].

2.3.2 State of the art of integrated modulator VCSEL

As the VCSEL and the surface normal EAM both are a Fabry-Pérot optical cavity structure that consist of a section of quantum wells interposed between DBRs, they

can easily be integrated on each other. When epitaxially grown, the two cavities can be accordingly aligned while using the same materials.

Since the light in a cavity is confined and reflected back and forth multiple times, it produces a standing wave pattern at a certain frequency, so-called cavity resonance frequency. Since we have two cavities, we actually have two standing waves. When their frequencies are identical, the two cavities are coupled. But if the cavities are detuned by modifying the length of one of them, the two modes show a different frequency. If the frequencies are too far from each other, the EAM is unable to absorb the photons coming from the VCSEL.

In 1997, Pellandini et al. [23] investigated the effects of coupling a cavity to a VCSEL, and showed that their device could either achieve lasing at two wavelengths, or display temporal instabilities and wavelength switching depending on the detuning. This coupling is an important constraint on the design of such a structure, and have far-reaching influence on device performance.

Eisden et al. achieved in 2007 a bandwidth of $17GHz$ for a $980nm$ VCSEL with an integrated EAM [24]. In 2014, Dalir et al. realised a structure which integrates the EAM laterally, on the side of the VCSEL, and reached a bandwidth of $35GHz$ at a wavelength of $850nm$ [25]. Finally, in 2018 Marigo-Lombart et al. demonstrated a vertically integrated EAM on a VCSEL with a bandwidth of $29GHz$ [26].

2.4 VCSELs and EAMs operation principle

2.4.1 Semiconductor lasers

Lasers work by amplifying light through positive feedback. In the case of a VCSEL, the feedback is created by reflecting mirrors called Distributed Bragg Reflectors (DBR), and the optical gain is obtained through stimulated emission in Quantum Wells (QW). The figure 4 shows the cross-section of a typical oxide confined VCSEL, which is the most common VCSEL structure. This structure is composed of a backside n-type electrical contact (in light yellow), a n-type $GaAs$ substrate (in light purple), a n-type DBR (in cyan shades), a QW active region (in vivid pink), the oxydation layer (indigo), the p-type DBR, and the p-type electrical contact.

2.4.1.1 Stimulated emission

The purpose of a VCSEL is to achieve an emission of coherent light, where all the photons share the same wavelength, polarisation and direction of propagation. In

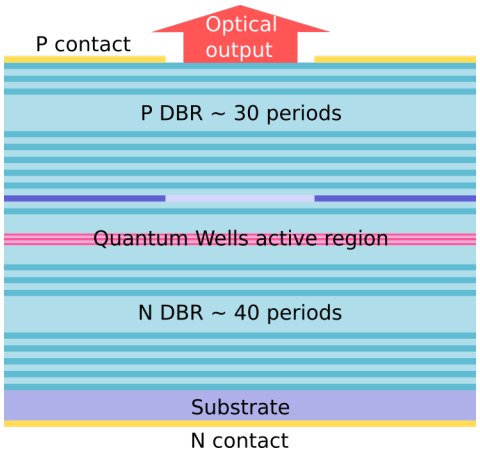

Figure 4: Cross-section diagram of an oxide-confined VCSEL.

semiconductors, the interaction between photons and electrons can be categorised into three types of optical processes:

- Spontaneous Emission: an electron in conduction band recombines with a hole in valence band. During recombination, the electron releases its excess energy as a photon. This emitted photon has an energy close to the energy bandgap of the material. Spontaneous emission is the underlying mechanism behind light emission in light-emitting diodes (LEDs), where the recombination of electrons and holes produces photons.

- Stimulated Emission: this occurs when an incident photon interacts with an electron in the conduction band, causing it to transition to the valence band and recombine with a hole. The emitted photon shares the same properties (frequency, polarisation, and phase) as the incident photon, resulting in coherent or in-phase radiation. The term "stimulated" emphasizes that this type of emission requires the presence of photon density in the active region of a light-emitting device, and the upper energy level must have a higher carrier density. Stimulated emission is the process exploited in laser operation, as it leads to the amplification and coherent output of light.

- Absorption: when a photon with energy greater than the band gap of the semiconductor material interacts with the material, it can transfer its energy to an electron in the valence band. This energy transfer excites the electron, promoting it into the conduction band.

Let us consider a two-level system with two energy levels E_1 and E_2, the energy of the photon E is equal to the energy difference $E = E_2 - E_1$ called band gap. According to the Planck-Einstein relation, the energy of the photon is given by $E = h\nu$, where

h is Planck's constant, and ν is its frequency. The probability per unit of time for an atom to transition from a high energy level E_2 to E_1 spontaneously emitting a photon is given by the Einstein coefficient A_{21}. With n_2 being the density of atoms at energy level E_2, the rate W_{21} at which a transition occurs between two states from spontaneous emissions is:

$$W_{21} = A_{21} n_2 \tag{1}$$

Since stimulated emission involves the presence of an incident photon, the rate of stimulated emission W_{21}^s depends on the photon density u_λ and the probability B_{21} for an electron to transition from state 2 to state 1 follows:

$$W_{21}^s = B_{21} n_2 u_\lambda \tag{2}$$

Finally the rate W_{12} at which absorption occurs is given by the probability B_{12} for an electron to transition from state 1 to state 2, the density n_1 of atoms at state 1, and the photon density:

$$W_{12} = B_{12} n_1 u_\lambda \tag{3}$$

At thermal equilibrium, the rate of upward and downward transitions are equal:

$$W_{12} = W_{21} + W_{21}^s \tag{4}$$

2.4.1.2 Population inversion

At thermal equilibrium $n_1 > n_2$ according to Boltzmann statistics, which is why upward and downward transition rates are equal. In order to achieve the emission of coherent light, not only the sum of downward transitions must be superior to the upward ones, but the stimulated emission must be predominant. This can only be achieved if $n_2 > n_1$, and is called the population inversion condition. In a two-level system, the population inversion is close to impossible to achieve. For the purpose of fulfilling this condition, several theoretical choices are possible. In the case of a VCSEL, this is achieved at the expense of some band gap engineering using quantum wells in a p-i-n diode heterojunction.

2.4.1.3 Quantum well Lasers

The typical structure of VCSELs is a p-i-n junction, with a few quantum wells within the intrinsic region. A quantum well is a potential well with a thickness on the order of the de Broglie wavelength of an electron. This is achieved with a layer (the

well) of a few nanometers thick, placed between two layers (the barriers) with a higher band gap.

When unbiased, the structure is at charge equilibrium. The probability that a state is occupied at an energy level E, or the average number of electrons per state follows the Fermi-Dirac distribution:

$$f(E) = \frac{1}{1 + \frac{exp(E-E_F)}{k_B T}} \tag{5}$$

E_F is the Fermi level, a state which has 50% chance of being occupied. Here at charge equilibrium, this level is in the middle of the band gap.

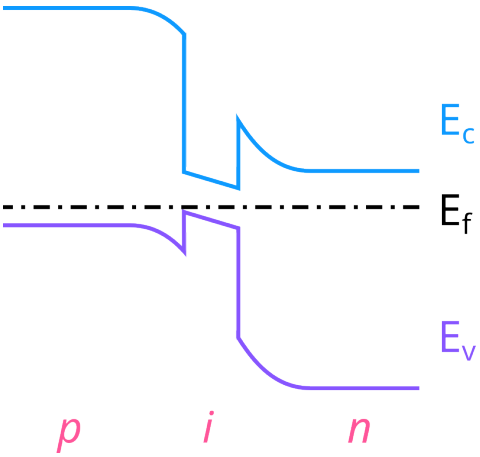

(a) Unbiased at thermal equilibrium.

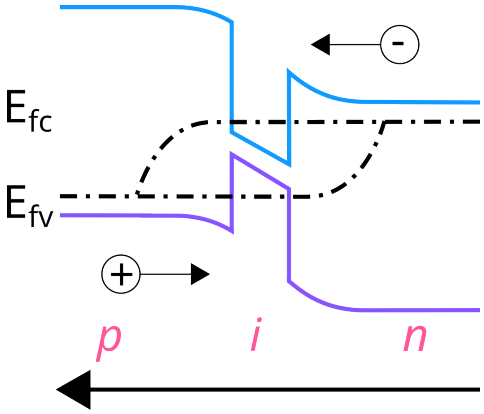

(b) Forward bias with quasi-Fermi level splitting.

Figure 5: Conceptual Energy Band Diagram for p-i-n Junction with Quantum Well, Including Fermi Levels.

When the structure is biased, charges are injected, and the equilibrium is broken. The intrinsic "i" region is flooded with charge carriers from the "p" and "n" regions allowing for high injection. The Fermi level splits in two quasi-Fermi levels, E_{Fn} for the electrons, and E_{Fp} for the holes. Figure 5a shows the band energy diagram with conduction band E_c and valence band E_v of a quantum well in a p-i-n junction with and without bias, and the induced Fermi-level splitting.

The Fermi-Dirac integral gives the concentration of charge carriers n as a function of the Fermi-Dirac distribution, and the density of states $g(E)$:

$$n = \int f(E)g(E)dE \tag{6}$$

In this configuration, the condition for population inversion is [27]:

$$\begin{cases} E_{Fn} > E_c \\ E_{Fp} < E_v \end{cases}$$

which is achieved in a quantum well under bias located in the intrinsic region as it can be seen in figure 5b.

Due to the well thickness being in the order of magnitude of the de Broglie electron wavelength, the charge carriers experience quantum confinement. This means that, theoretically, at low concentrations, their energy levels become discretized into specific values known as subbands. As charge carriers predominantly occupy these subbands, quantum wells exhibit a significantly higher carrier density and offer more available states at the band edges. Consequently, this results in shorter pumping times, enabling faster on/off switching, and lower threshold currents with reduced sensitivity to temperature variations [27]. Moreover, the carrier confinement prevents the injected electron and hole pairs from going through the depletion region without recombining, which leads to a higher emission power.

Figure 6 shows the energy band diagram and structure of the active region of a typical VCSEL.

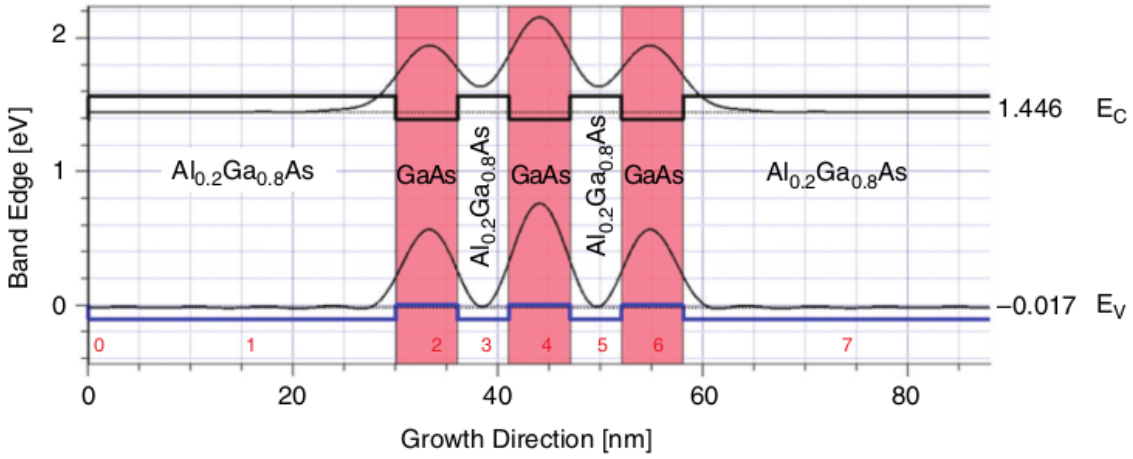

Figure 6: Energy band diagram of three $6nm$ $GaAs$ QW (in light red), the conduction band (black) and valence band (blue), and the electron and hole wavefunctions (from [28]). The band gap ($E_c - E_v$) of the QW structure is $1.46eV$ ($\sim 850nm$).

2.4.1.4 Optical Feedback

Achieving population inversion for lasing requires a second condition: increasing the density of photons that are in-phase within the optical cavity. This is accomplished through the use of an arrangement of mirrors that enclose the gain medium, to create an optical feedback. The objective here is to reflect the incident photons back into the cavity using two highly reflective mirrors. This reflection process shifts the main type of emission from spontaneous to stimulated. It is mandatory for these mirrors to

be parallel to each other, while the emitted light is perpendicular to them. Optical feedback requires:

- an optical gain superior to the losses due to absorption, scattering or mirrors imperfection,
- the length of the optical cavity (L), to be equal to a multiple of half the wavelength λ of the electromagnetic wave to create resonance:

$$L = \frac{\lambda q}{2n} \tag{7}$$

With n being the refractive index of the medium, and q an integer.

By confining light within the cavity and reflecting it multiple times, standing waves are generated at specific wavelength which are called modes. An optical cavity can emit several modes, each with its own wavelength. There are two types of modes: longitudinal modes, which are determined by the length of the cavity, and transverse modes, which are determined by the diameter of the cavity. In the case of a VCSEL, only one longitudinal mode close to the wavelength of emmission remains, as the cavity is very short. As for the transverse modes, it is possible to reduce their number by decreasing the cavity diameter or by adding restrictive windows within the cavity. In VCSELs, this is usually achieved by placing a thin oxidisable layer inside the cavity [29]. The layer is then oxidised by the sides and creates an optical aperture. The oxide aperture also provides current confinement with low-leakage current and reduced scattering losses [30].

2.4.1.5 VCSEL

Vertical Cavity Surface Emitting Lasers (VCSELs) distinguish themselves from traditional edge-emitting semiconductor lasers by having a cavity design perpendicular to the wafer surface, resulting in surface emission. They are commonly produced using Molecular Beam Epitaxy (MBE) or Metal-Organic Vapour Phase Epitaxy (MOVPE). The optical cavity of a VCSEL is a conventional Fabry-Pérot cavity, with Distributed Bragg Reflectors (DBR) on both sides. These DBRs are created by growing a multi-layered, periodic structure with alternating quarter-wavelength layers of materials with different refractive indices. As a result, they can achieve a reflectivity exceeding 99.9%. The epitaxial growth of the vertical active region limits its thickness, leading to a VCSEL cavity length of around $100nm$ Despite this shorter cavity length than the edge-emitting semiconductor lasers, the incorporation of the highly reflective DBRs ensures the optical feedback. $AlGaAs$ VCSELs typically have a top DBR of ≈ 30 periods, and a bottom DBR of ≈ 40 periods. The active region has an optical thickness multiple of half of the emission wavelength, and includes 3 quantum wells of 5 to $15nm$ in

order to provide the gain, with confinement barriers of $\approx 10nm$ containing 20 to 40% of aluminium. The wavelength of emission is of course linked to the band gap of the quantum wells, which is $1.463eV$ for $848nm$.

VCSELs have gained popularity over other alternatives for several compelling reasons. The manufacturing and integration of VCSELs into wafers align well with detectors and various circuitry. Their reduced threshold currents result from the relatively compact size of the active region. They exhibit high reliability and extended lifetimes. VCSELs can undergo comprehensive testing while still on the wafer, enabling early detection and removal of defective batches, ultimately reducing costs and increasing yield. The vertical design of VCSELs allows for the creation of VCSEL arrays, which is especially useful in applications such as LiDAR for increased power output. They are compatible with cost-effective LED packaging and can even replace LEDs in certain applications. Integration into systems using Chip-on-board technology is feasible, and their high power efficiency alleviates thermal constraints when integrated with other systems. Furthermore, VCSELs produce circularly symmetric far-field profiles, exhibit no astigmatism, and have low divergence, making them easily coupled with optical fibers. Additionally, when equipped with the appropriate oxide aperture, VCSEL emission can be single longitudinal mode, rendering them compatible with single mode fibers. These latter points explain why VCSELs are particularly well-suited for optical communication applications.

2.4.2 EAM basic principles

2.4.2.1 Bulk absorption

Static absorption The optical absorption refers to the process by which a material absorbs electromagnetic energy from incident photons and subsequently transforms it. In the context of semiconductor crystals, absorption involves the interaction between a photon with a specific energy and an electron within the crystal. This interaction elevates the electron to a higher energy level, a phenomenon referred to as a transition. These transitions can take various forms, including band-to-band transitions, excitonic transitions, and transitions involving impurities within the material. The absorption coefficient α is defined as the relative rate of decrease in light intensity L along its path, for a given photon energy hv:

$$\alpha(hv) = \frac{1}{L(hv)} \frac{dL(hv)}{dx} \tag{8}$$

Typically, the absorption refers to the interaction between a photon and an electron in the valence band, which results in the electron gaining enough energy to move from

the valence band to the conduction band. In this case, the absorption coefficient is proportional to the probability of transition of state B_{12} (from equation 3), the density of initial states n_1, and the density of empty final states n_2 for all different transitions between states with a difference of energy equal to the photon energy hv:

$$\alpha(hv) = A\Sigma B_{12} n_1 n_2 \tag{9}$$

The absorption coefficient is related to the refractive index by the extinction coefficient. Let us consider the radiation to be a plane wave of angular frequency ω propagating in the x direction with a velocity v, the magnitude of the electric field $\mathcal{E}$ given by:

$$\mathcal{E}(x,t) = \mathcal{E}_0 \text{exp}\left[j\omega\left(t - \frac{x}{v}\right)\right] \tag{10}$$

complex refractive index $\overline{n}$ is given by

$$\overline{n} = n + jk \tag{11}$$

$$\text{With: } \begin{cases} n : \text{real refractive index} \\ k : \text{extinction coefficient} \end{cases}$$

The velocity of propagation v in the medium is:

$$\overline{v} = \frac{c}{\overline{n}} \tag{12}$$

Therefore:

$$\frac{1}{\overline{v}} = \frac{n}{c} + \frac{jk}{c} \tag{13}$$

By substituting equation 13 into 10, we can obtain the fraction of the incident power available after propagating a distance x:

$$\frac{P(x)}{P(0)} = \frac{\mathcal{E}^2(x)}{\mathcal{E}^2(0)} = \text{exp}(-\frac{2\omega k x}{c}) = \text{exp}(-\alpha x) \tag{14}$$

Finally, the absorption coefficient α is related to the extinction coefficient k by:

$$\alpha = \frac{2\omega k}{c} = \frac{4\pi k}{\lambda} \tag{15}$$

where λ is the wavelength in free space.

Casey et al. [31] have calculated the absorption coefficients for n and p type $GaAs$ for photon energy in the range of 1.3 to $1.6eV$ (a range of wavelength from 775 to $950nm$) as it can be seen in figure 7.

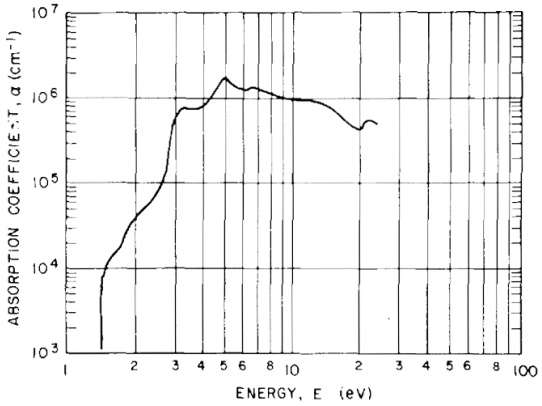

(a) Bulk unintentionally doped.

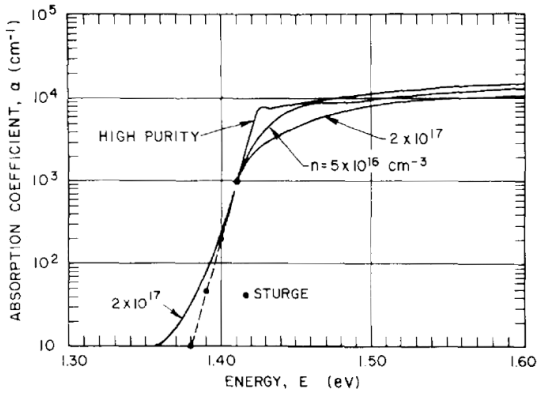

(b) For different doping levels.

Figure 7: Absorption coefficient in $GaAs$ at 297K from [31]

The figure 7b is a zoom on the figure 7a, with different doping concentrations. It can be seen that increasing the doping concentration decreases the absorption above the bandgap ($1.424eV$), and decreases it below through a tail broadening effect.

Increasing the doping concentration also smooth the absorption peak located slightly below the bandgap in the high purity case, which corresponds to the heavy-holes excitonic peak. This smoothing of the absorption peak tends to be a problem, as it reduces the absorption contrast, which in the case of EAM needs to be maximized. An exciton is a pseudo-particle which consists of a pair of an electron and a hole that are attracted to each other through Coulomb attraction. Since the exciton is in a slightly lower energy state than the unbound hole–electron, its energy is slightly inferior to the value of the bandgap, which is why this excitonic peak is located below the bandgap energy. This excitonic peak will play an important role in the EAM-VCSEL structure, so the tail broadening effect will need to be taken into account in order to balance a trade-off between optical and electrical properties of the device.

Modulation of absorption in bulk When an electric field is applied to a bulk semiconductor, the electrons and holes wavefunctions become Airy functions ([1] in figure 8a), which includes a 'tail' ([2]) extending to the forbidden zone ([3] in red). In figure 8a, we can see the tail of the electrons wavefunction extending to the left in the bandgap, and the holes wavefunction extending to the right. This increases the overlap between the wavefunctions, thus increasing the optical absorption.

However, this Franz-Keldysh effect can only be achieved with very strong electric fields, usually requiring hundreds of volts. This amount of voltage not being compatible with typical miniaturized photonic devices, using this effect to achieve absorption modulation has to be discarded.

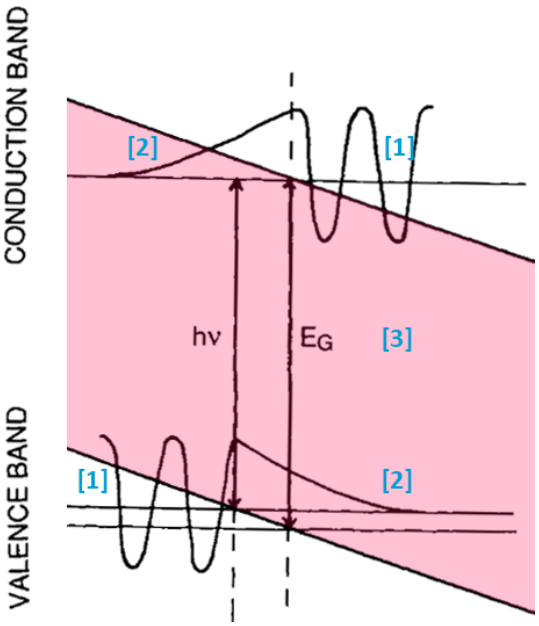

(a) Band-diagram in the case of a bulk material, depicting the Franz-Keldysh effect.

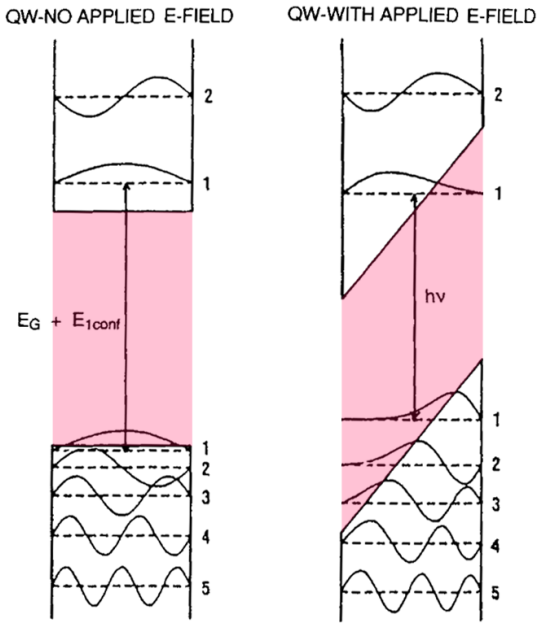

(b) Wavefunctions corresponding to the first and second levels in a quantum well, depicting the quantum-confined Stark effect.

Figure 8: Band-diagrams including electrons and holes wavefunctions of a semiconductor material polarised by an electric field from [32].

2.4.2.2 Quantum wells absorption

An alternative to modulate the absorption is to take benefit of the quantum confinement through bandgap engineering. Intrinsic $GaAs$ has a bandgap of $1.424eV$, and according to [33], $Al_xGa_{1-x}As$ bandgap follows:

$$\begin{aligned} x < 0.45 \quad & 1.247x + 1.424 \quad eV \\ x > 0.45 \quad & 0.143x^2 + 0.125x + 1.9 \quad eV \end{aligned} \tag{16}$$

For instance for a material composed of $Al_{0.3}Ga_{0.7}As$, its bandgap will be around $1.8eV$. By encasing a layer of $GaAs$ between two layers of $AlGaAs$, since the bandgap energies of these materials are different, we obtain a local minimum of potential energy ($GaAs$) surrounded by two higher potentials ($Al_xGa_{1-x}As$) called a potential well. If the thickness of the low potential layer is of the same magnitude as the de Broglie wavelength, quantum confinement occurs, and the energy level values become discrete and are called 'energy subbands' as seen in figure 8b.

When an electric field is applied to a quantum well, the wavefunction of the electrons becomes tilted, shifting towards the side of the well with the lowest potential.

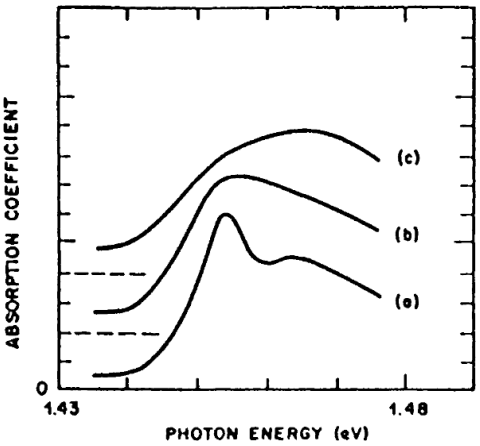

(a) In the case of an electric field parallel to the layers of (a) to (c), 0, 1.6×10^4, $4.8 \times 10^4 V.cm^{-1}$

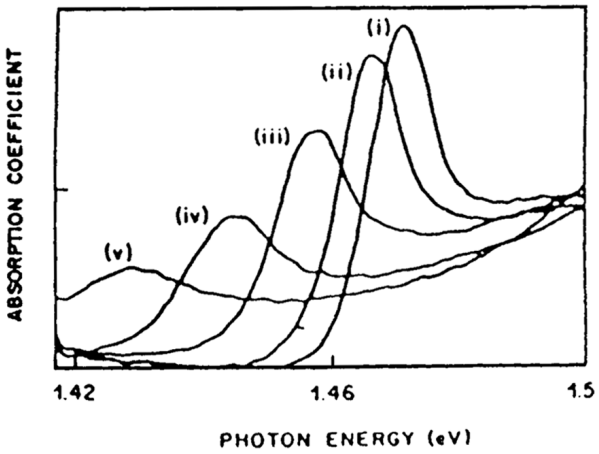

(b) In the case of an electric field perpendicular to the layers of (i) to (v), 0, 6×10^4, 1.1×10^5, 1.5×10^5, $2 \times 10^5 V.cm^{-1}$

Figure 9: Quantum-confined Stark effect on absorption for $9nm$ quantum wells for different electric fields [34].

Conversely, the wavefunction of the holes shifts towards the other side, as illustrated in Figure 8b. This phenomenon is known as the Quantum-Confined Stark Effect (QCSE). The QCSE alters the degree of overlap between the wavefunctions, consequently modifying the probability of photon absorption.

Applying the electric field either parallel or perpendicular to the quantum well layers leads to distinct modifications in absorption behavior. When an electric field is applied in parallel, as depicted in Figure 9a, we observe a slight increase in absorption, accompanied by broadening of the excitonic peak. Conversely, with a perpendicular electric field (as shown in Figure 9b), absorption decreases, and the excitonic peak both broadens and undergoes a redshift. Hence, a perpendicular electric field yields a more pronounced absorption modulation, making it particularly suitable for electro-absorption devices.

2.5 Conclusion

The ever-increasing demand for faster data access, propelled by a significant rise in internet usage and bandwidth-intensive activities, is leading to the expansion of data centers, HPCs. The current trend in order to meet the data rate demand surge is a combination of VCSEL technology, complex encoding formats and driving circuitry. In order to improve the data rate, and better answer the constraints met in datacenters and HPCs, we propose a different approach, with the EAM-VCSEL, where the emitting and the modulation sections are as decoupled as possible. This allows us to go beyond the

inherent limit of direct modulation VCSELs while having a single integrated component.

The work realised in this manuscript itself is a continuation of a previous thesis work led at LAAS-CNRS by L. Marigo-Lombart. First of all it is important to improve the design while taking into account the latest advancements on the understanding of the tricky coupling between cavities [19]. Moreover, since the coupling is very sensitive to cavities thicknesses (L. Marigo-Lombart had trouble achieving repeatability on this point), a method to achieve a systematic precise coupling is investigated. Since the earliest design exhibited a very high impedance, the reduction of electrical losses in the extrinsic part of the device is addressed. The critical steps of the manufacturing process have been improved, especially the SiO_x lift-off, and the plasma etching. Finally, it is important to characterise the coupling post-epitaxy in order to estimate the yield of optimal coupling devices.

The work presented in this manuscript is heavily focused on the modulator itself. The second chapter focuses on the design and the modelling of the EAM-VCSEL. Then we explain how to improve the absorption dynamic by maximizing the QCSE, and reduce the impact of parasitic effects which are detrimental to the modulation such as the DBR impedance and the coupling. The third chapter presents the fabrication of the device. It includes a review of all the manufacturing steps from epitaxy to the final component with an hindsight of the most critical parts such as the oxide aperture and the BCB packaging. The problems met and their solution are detailed. Finally the last chapter presents the characterisation of the EAM, including its high-frequency operation.

3 Design and modelling

The purpose of this chapter is to investigate how to design the EAM-VCSEL in order to maximize the optical response for a given electrical command. Since the modulation of the optical absorption relies on the QCSE, on an electrical point of view, only the stack of MQWs intrinsically contributes to the modulation of absorption. Ideally, the bias should only be applied at the limits of this zone, but for the ease of fabrication, it has to flow through the DBRs.

Regarding the zone which is intrinsic to the modulation (the MQWs), the absorption peak shift per unit of electrical bias needs to be maximized in order to achieve the highest contrast ratio. Moreover, the quantum wells have an inherent limit of how many charge carriers they can hold. When a QW is saturated, it cannot absorb anymore photons and no more absorption can occur. Therefore the evacuation of charge carriers must be eased as it limits the modulation rate.

The DBRs participate in the confinement of light in the EAM, but do not contribute directly to the absorption modulation. Thus, on an electrical point of view, they are extrinsic to the absorption electrical command.If their resistance is too high, the slightest parasitic capacitance introduces a high time constant limiting the bandwidth. Because DBRs are heterojunctions, they inherently possess such a high resistance, which needs to be minimized.

The first section focuses on the region which is intrinsic to the modulation. We present a model to calculate the absorption as a function of the MQWs physical properties and a given electric field, to design the stack and optimise the modulation depth. We also investigate how to improve the electrical charge carrier dynamics to increase the bandwidth.

The second section presents a method to design the region which is extrinsic to the QCSE to optimise the light confinement. We also present the grading interfaces of the DBRs to decrease their resistance.

The third section presents the different structures of EAM and EAM-VCSELs. We also investigate how to design the best coupling between the EAM and the VCSEL.

3.1 EAM cavity design

3.1.1 Absorption modelling

Since the EAM-VCSEL relies on the quantum-confined Stark effect, we need to be able to calculate the absorption while considering the different parameters we can afford to modify, namely the shape and dimensions of the quantum well, the amount of aluminium in the confinement barriers and the perpendicular electric field.

Several types of quantum well exist, mainly regular wells or coupled wells. Coupled wells typically have a slightly better absorption peak movement rate than regular wells [35]. However, Marigo-Lombart et al. [36] showed that the bandwidth of an EAM-VCSEL was limited by the DBR impedance rather than the quantum wells. Moreover, as we will see in section 3.1.3, the bandwidth is also limited by the charge carrier escape time which is the same in the case of coupled and non-coupled quantum wells. We made an attempt at simulating the device using Sentaurus with finite element method, but we encountered significant challenges during the simulation process, leading to inconsistent results and difficulties in achieving convergence to a solution. Therefore, we choose to focus on regular quantum wells, with a model for electro-absorption developed by Lengyel et al. [37], which is perfectly suitable as a design-tool for multiple quantum well optical modulators. It is a fast semi-empirical model that allows us to calculate the absorption within a quantum wells as a function of the parameters of interest: the aluminium content within the confinement barriers, the QW thickness, and the applied electrical field.

The results of this model are depicted in figure 10. We can see that decreasing the potential barrier redshifts the absorption peak without decreasing it (figure 10a). Decreasing the quantum well thickness slightly increases the absorption peak and blueshift it (figure 10b), which is because the confinement increases. And finally, the absorption peak slightly decreases and undergoes a redshift when the electric field increases (figure 10c), which is consistent with figure 9b. On figure 10c, at $90 kV.cm^{-1}$, the absorption peak reaches a high level of absorption of $1.7.10^4 cm^{-1}$ at $848nm$. At this same wavelength, with an electric field of $30 kV.cm^{-1}$, the peak shifts, and the absorption at $848nm$ decreases to a low level of $0.3.10^4 cm^{-1}$. This redshift of the exciton peak is the main effect that will be used to achieve strong absorption. This makes the electro-absorption modulator a device that could be considered as normally-on.

Since this model only calculates the analytical solutions for the heavy-holes carriers, the absorption cannot be calculated for the light-holes. Thus the wavelength range is limited to energies around the excitonic peak and below. Indeed we can see in figure 10 that the absorption cannot be calculated $\approx 5nm$ below the excitonic peak wavelength. This is not a problem as the excitonic peak provides the strongest absorption and is

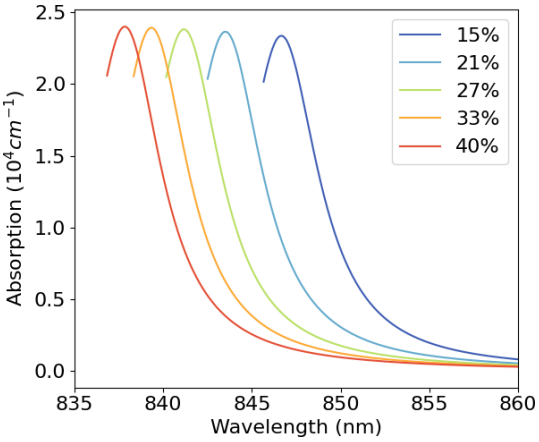

(a) For several confinement barrier aluminium contents.

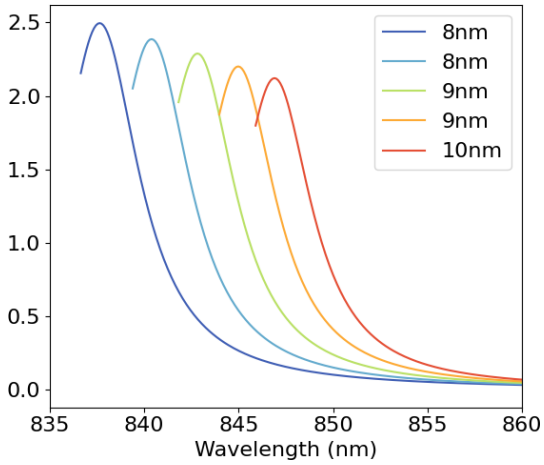

(b) For several quantum well widths.

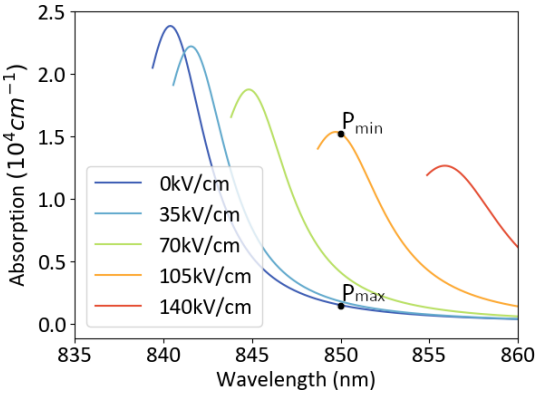

(c) For several electric fields.

Figure 10: Spectral dependence of absorption of a single quantum well for different aluminium concentrations in the confinement barrier (a), quantum well widths (b), and applied electric fields (c).

the zone of interest. Lengyel's model will also have trouble dealing with very small potential barriers and quantum well widths, as one can see in figure 11, but again this is not a problem as the optical configuration is within the calculation range.

3.1.2 Modulation depth optimisation

As explained in the previous part, the purpose of the electro-absorption modulator is to provide a light output with two or more different optical powers, which is achieved by using different values of absorption. To provide the best contrast ratio, the EAM needs to be optimised so that the minimal electrical potential difference result in the maximum absorption modulation. The relationship between the optical, electrical and logical behaviour of a modulator used for two-level (on-off) output modulation is summarised

in table 1.

Electro-absorption modulator state	Off	On
Output signal Boolean value	0	1
Optical power output	P_{min}	P_{max}
Absorption	α_{max} α_{off}	α_{min} α_{on}
Electric field applied	E_{max}	E_{min}

Table 1: Summary of the parameters of an electro-absorption modulator functioning at two levels (on-off) of output signal.

The ability of the modulator to achieve its purpose is typically described by the modulation depth η (or modulation index) following [38]:

$$\eta = \frac{P_{max} - P_{min}}{P_{min}} \tag{17}$$

Or by the contrast ratio (in dB):

$$C_r = 10log_{10}\frac{P_{max}}{P_{min}} \tag{18}$$

Since the modulator is fed with a constant source of light from a VCSEL, the difference between these output powers result from the amount of absorption that occurs within the EAM cavity. Chin et al. [39] [40] showed that, in the case of an electroabsorption modulator, the modulation depth and the contrast ratio depends on the ratio m_α following:

$$m_\alpha = \frac{\alpha_{\text{off}} - \alpha_{on}}{\alpha_{\text{on}}} = \frac{\Delta\alpha}{\alpha_{\text{on}}} \tag{19}$$

m_α is a normalised value quantifying how much the absorption increases, thus in order to improve the modulation depth, m_α needs to be maximised. However, this factor does not take into account the variation of the electric field, even though $\Delta\alpha$ depends on the variation on the electric field $\Delta E = E_{max} - E_{min}$. This is important and needs to be taken into account since generally, the larger the $\Delta\alpha$, the larger is the required ΔE.

The modulator capacitance, named C, forms a low-pass filter, with a bandwidth limited by a time constant τ representing the amount of time required to charge and discharge the capacitor. τ is given by the amount of charges:

$$\tau \approx \frac{Q}{I} = \frac{C\Delta V}{I} \tag{20}$$

with V being the bias voltage, and I the current.

Chin et al. finally show that $C\Delta V$ is strongly influenced by m_α, and another factor m_E taking into account the electric field swing:

$$m_E = \frac{\Delta E^2}{\Delta \alpha} \tag{21}$$

The factor m_E quantify how much the electric field increases for a given variation of absorption. And so, for the purpose of high contrast ratio , m_E needs to be minimised, while m_α needs to be maximised, which can be summarised using the following factor of merit:

$$f_{merit} = \frac{m_\alpha}{m_E} = \frac{\Delta \alpha^2}{\alpha_{\text{on}} \Delta E^2} \tag{22}$$

This figure of merit can be extracted from the Lengyel model for a set of different confinement barriers aluminium content, quantum well width, and the delta of the electric field, and thus find the optimal configuration of the quantum wells as depicted in figure 11.

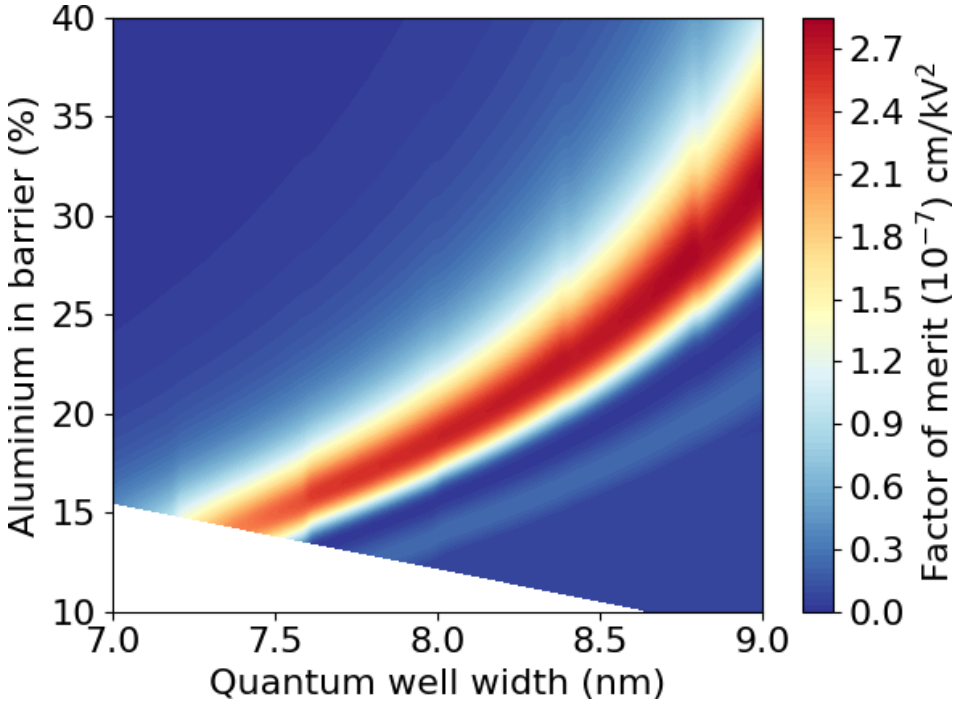

Figure 11: Figure of merit of a single quantum well of the electroabsorption modulator for a delta electric field of $80 - 60 kV.cm^{-1}$ at a wavelength of $850nm$.

The area of interest with a high factor of merit is in red, giving a set of possible optimized configurations for the quantum well and confinement barrier parameters, while

the blue areas correspond to configurations to be avoided. The left-hand corner corresponds to the limit of the Lengyel model. Typical electroabsorption modulators usually have quantum well with a thickness around $9nm$ to $12nm$ [41] [42], and confinement barriers with around 30% aluminium content. But as our figure of merit shows, the content of aluminium can be reduced if the thickness of the quantum well is reduced accordingly.

3.1.3 Escape time

When a photon is absorbed in a quantum well, it generates a free carrier. Therefore, when the modulator is in a state of high absorption, the concentration of charge carriers increases. However, because the quantum well does not have infinitely high potential barriers, the charge carrier concentration is limited. Once this limit is reached, further absorption is prevented [43] [44]. Hence, maintaining the desired absorption level requires optimizing the evacuation of charge carriers to prevent quantum well saturation.

The charge carriers can escape the quantum well through two known effects: quantum tunneling and thermionic emission. In quantum tunneling, a particle can cross the potential barrier if its wavefunction can propagate through it. Tunneling depends on the potential barrier height and the thickness of the confinement barriers. However, the thickness of the confinement barriers cannot be reduced, as doing so would deconfine charge carriers and negate the benefits of quantum confinement.

Thermionic emission refers to thermally-excited charge emission processes, which occur in our case when charge carriers overcome the work function of the confinement barrier due to thermal energy. This emission is directly dependent on temperature and the height of the potential barrier. Given that quantum tunneling is negligible in the proposed stack due to the thickness of the barriers, charge carrier evacuation primarily relies on thermionic emission.

The mean amount of time required for a charge carrier, such as an electron or a hole, to escape the quantum well is known as the escape time, denoted here as τ_i with i representing the particle type. Reduction in the escape time of photo-generated charge carriers has been investigated by Shin et al. [45]. The quantum tunnelling escape-time τ_{E_i} can be calculated following:

$$\frac{1}{\tau_{E_i}} = \sqrt{\frac{k_B T}{2\pi m_i^* L_w^2}} \exp\left(-\frac{H_i(F)}{k_B T}\right) \tag{23}$$

While the thermionic escape-time τ_{T_i} can be calculated following:

$$\frac{1}{\tau_{T_i}} = \frac{n\hbar^2\pi}{2m_i^* L_w^2} \exp\left(-\frac{2L_b\sqrt{2m_{bi}^* H_i'(F)}}{\hbar}\right) \tag{24}$$

k_B is the Boltzmann constant, m_i^* is the effective mass of holes or electrons, L_w is the quantum well thickness, $\hbar$ the Plank constant and L_b the confinement barrier thickness. $H_i(F)$ is the field dependent barrier height given as follows:

$$H_i(F) = Q_i \Delta E_g - E_i^{(n)} - \frac{|e| F L_w}{2} \tag{25}$$

Q_i is the electron charge, ΔE_g the band discontinuity, $E_i^{(n)}$ the particle's ground state energy, and F the electric field. The total escape-time can finally be calculated:

$$\frac{1}{\tau_i} = \frac{1}{\tau_{E_i}} + \frac{1}{\tau_{T_i}} \tag{26}$$

The total escape-time as a function of the aluminium content is given in figure 12a. As expected, this value is higher for the holes, because their affinity is lower than the electrons one. We can see that by reducing the aluminium content of only 10%, the escape time for heavy holes can be reduced by an order of magnitude in the case of the heavy holes. On the other hand, one can see in figure 12b that the quantum well width has a minor influence on the carrier escape time.

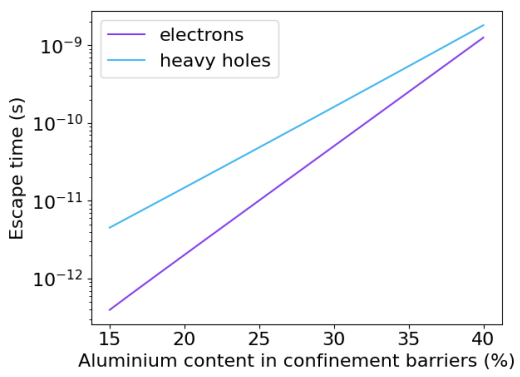

(a) As a function of aluminium content in the confinement barriers with quantum wells of $8.3nm$ width.

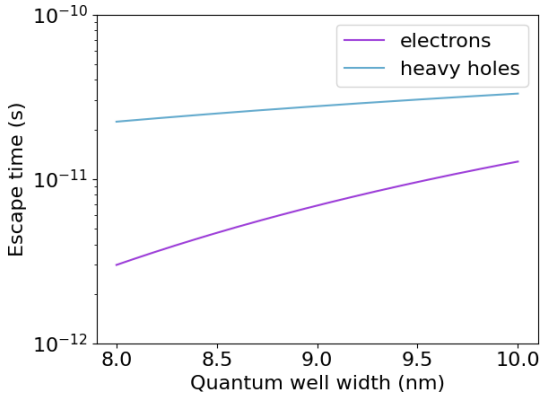

(b) As a function of quantum well width with 22% aluminium content in the confinement barriers.

Figure 12: Escape time for heavy holes and electrons of a single $GaAs$ quantum well with $AlGaAs$ confinement barriers of $10.3nm$ width and no electric field.

Thermionic emission could be enhanced by introducing gradings between the quantum wells and confinement barriers. Shikawa et al. [46] demonstrated the effectiveness of this approach in terms of energy shift under applied voltage, using a grading in the quantum well with aluminum content ranging from 0% to 30%. However, this method complicates the epitaxial process and reduces absorption due to decreased confinement. Alternatively, the potential barrier height can be reduced by lowering the aluminum fraction within the confinement barrier [47].

Typical $AlGaAs$ VCSEL and EAM structures include confinement barriers with a fraction of aluminium within the range of 30 to 40%, but in our case, this value could be reduced to achieve better charge evacuation if no major drawbacks with the other design method is obtained.

The escape time of charge carriers is directly related to the maximum modulation frequency of a device, as it dictates how quickly charge carriers can be removed from the quantum well. A longer escape time may result in a slower evacuation of charge carriers, imposing a limit on the maximum modulation frequency. Conversely, a shorter escape time enables the device to switch between low and high charge carrier densities more rapidly, facilitating a higher maximum modulation frequency. In fact, with an escape time of $\tau = 1.10^{-11}s$, we can establish an upper limit for the modulation frequency, denoted as f_{max}:

$$f_{max} = \frac{1}{\tau} = 100GHz \tag{27}$$

3.1.4 Cavity structure

The absorption of the cavity is proportional to the amount of quantum wells. To provide modulation performances comparable to EAMs for edge emitter lasers, the cavity would need to be more than a hundred micrometers thick [48]. Since this order of magnitude cannot be grew by epitaxy, one possibility is to encase the cavity by an asymmetric Fabry Perot structure [49]. This confines the light, increasing the probability of interaction between the photons and the quantum wells.

Section 3.1.3 showed us that a lower value of aluminium content than usual (for instance 20% instead of 30%) leads to better charge carrier evacuation. And chapter 3.1.2 provides us a set of single quantum wells and confinement barriers configurations to optimise the modulation depth that are compatible with the results from chapter 3.1.3. Considering a 22% aluminium confinement barrier, the figure of merit 11 suggests a quantum well thickness of $8.3nm$.

The active region, comprising Multiple Quantum Wells (MQWs), is situated within the optical cavity of the EAM. This region is surrounded by Distributed Bragg Reflectors (DBRs). To ensure constructive interferences and transparency at the desired application wavelength of $850nm$, the length of the MQW stack must be a multiple of the half-wave thickness:

$$d_{cavity} = m\frac{\lambda}{2n} \tag{28}$$

If we consider the previously described quantum wells configuration, with confinement barriers of $10nm$, the mean Al content is around 12%, and the mean index of refraction

is $n = 3.51$. We choose a cavity length of 4 times the half-wave thickness, thus:

$$d_{cavity} = 4\frac{\lambda}{2n} = 483nm \tag{29}$$

This imply that the cavity will contains 24 confinement barriers and 25 quantum wells with $36nm$ of cladding layers as summarised in table 2.

Layer	Aluminium content	Thickness
Cladding	22%	$18nm$
Quantum Well x25	0%	$8.3nm$
Confinement barrier x24	22%	$10nm$
Cladding	22%	$18nm$

Table 2: Electroabsorption modulator cavity structure.

3.2 EAM distributed Bragg reflectors design

3.2.1 Transfer matrix method

To design and optimize the structure of the EAM-VCSEL, we require a method for calculating the device's reflectivity. For this purpose, we employ the Transfer Matrix Method (TMM), a semi-analytical technique utilized to analyze the transmission and reflection of light as it traverses through complex structures, particularly those consisting of multiple layers with varying optical properties. In our case, TMM is applied to study how light propagates through the EAM. Conceptually, the structure is treated as a stack of layers with distinct optical characteristics (see Figure 13). This method enables us to compute the electromagnetic field components, $\vec{E_i}$ and $\vec{H_i}$, at each layer interface.

Each layer is described by a matrix equation M_i that represents its optical properties depending on refractive n_i index and thickness L_i:

$$M_i = \begin{pmatrix} m_{11} & jm_{12} \\ jm_{21} & m_{22} \end{pmatrix} = \begin{pmatrix} \cos\delta_i & \frac{j}{\eta_i}\sin\delta_i \\ j\eta_i\sin\delta_i & \cos\delta_i \end{pmatrix} \tag{30}$$

Where:

$$\delta_i = \frac{2\pi}{\lambda_0} n_i L_i \cos\theta_i \tag{31}$$

The subscripts "i" "s" respectively denotes the i-th layer, and the output medium, $\lambda_0[m]$ is the wavelength of the incident ray, which is perpendicular thus $\theta = 0$. η_m

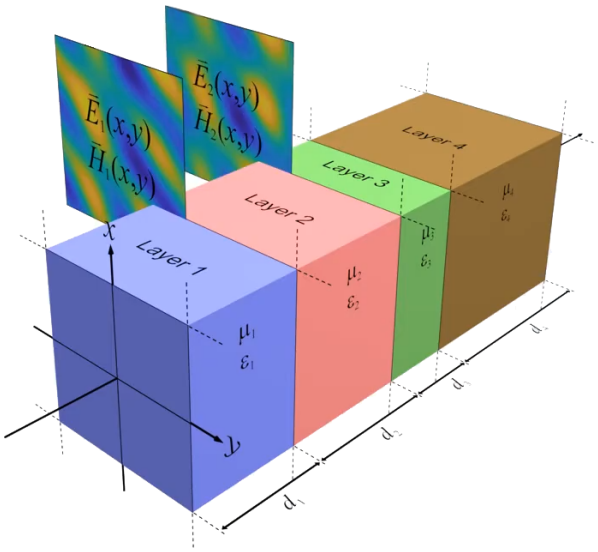

Figure 13: Diagram of a stack of layers illustrating how the TMM is applied. The TMM calculate the electromagnetic field at each layer interface (from [50])

and η_i are the effective refractive index of the incident medium and the i-th layer. We exclusively consider transverse electric polarisation, thus:

$$\eta_i = n_i \cos\theta_i = n_i \tag{32}$$

By multiplying the transfer matrix of every layer together, we can compute the global transfer-matrix M_G that describes the optical behaviour of the whole structure:

$$M_G = \prod_{i=1}^{L} M_i \tag{33}$$

We then obtain the amplitudes of the electrical component E_m and magnetic component H_m of the electromagnetic field in the incident medium m:

$$\begin{pmatrix} E_m \\ H_m \end{pmatrix} = M_G \begin{pmatrix} 1 \\ \eta_s \end{pmatrix} \tag{34}$$

Reflection and transmission coefficients of the whole structure are then calculated:

$$r = \frac{\eta_m E_m - H_m}{\eta_m E_m + H_m} \tag{35}$$

$$t = \frac{2\eta_m}{\eta_m E_m + H_m} \tag{36}$$

Finally, we obtain the intensity of the reflection and transmission coefficients of the device with:

$$T = \frac{\eta_s}{\eta_m}|t|^2 \tag{37}$$

$$R = |r|^2 \tag{38}$$

Throughout our study, we will extensively utilize the Transfer Matrix Method (TMM) to simulate and analyze the reflectivity of the structures under consideration for design purposes.

3.2.2 DBRs periods

An asymmetric Fabry-Perot structure is an optical arrangement designed for amplifying or filtering light. It comprises two Distributed Bragg Reflectors (DBRs) positioned on opposite sides of an optical cavity. These DBRs consist of layers with alternating high and low refractive indices, acting as mirrors that selectively reflect specific wavelengths of light. The range of reflected wavelengths, known as the bandwidth or plateau, is determined by the layers thicknesses, and the maximum reflectivity within this range is influenced by the number of DBR periods.

In an asymmetric Fabry-Perot structure, the two DBRs have different numbers of periods. The DBR with fewer periods is positioned on the side where the light is intended to exit the device, while the DBR with more periods is on the opposite side, where the light enters from the VCSEL. This configuration enables resonance within the cavity, facilitating the transmission of light through the DBR with fewer periods.

The amount of light reflected by the DBRs, named reflectivity, can be seen in figure 14. The difference between the bottom of the Fabry-Perot notch and the plateau decreases as the number of DBRs increases. A smaller number of periods leads to a broader resonance and a larger spectral operating bandwidth. It also decreases the impedance of the device since a DBR is a highly resistive heterojunction.

The number of periods of the top DBR typically ranges from 2 to 6 periods in electroabsorption modulators [51] [52] [53]. Marigo's design included 6 periods for the top DBR and 8 periods for the bottom DBR. In this configuration, the reflectivity of the Fabry-Pérot structure reaches a minimum of 20% in the notch, and is $10nm$-large at a reflectivity of 50% which is satisfactory. As a result, the number of DBRs considered for this work is unchanged from that of Marigo.

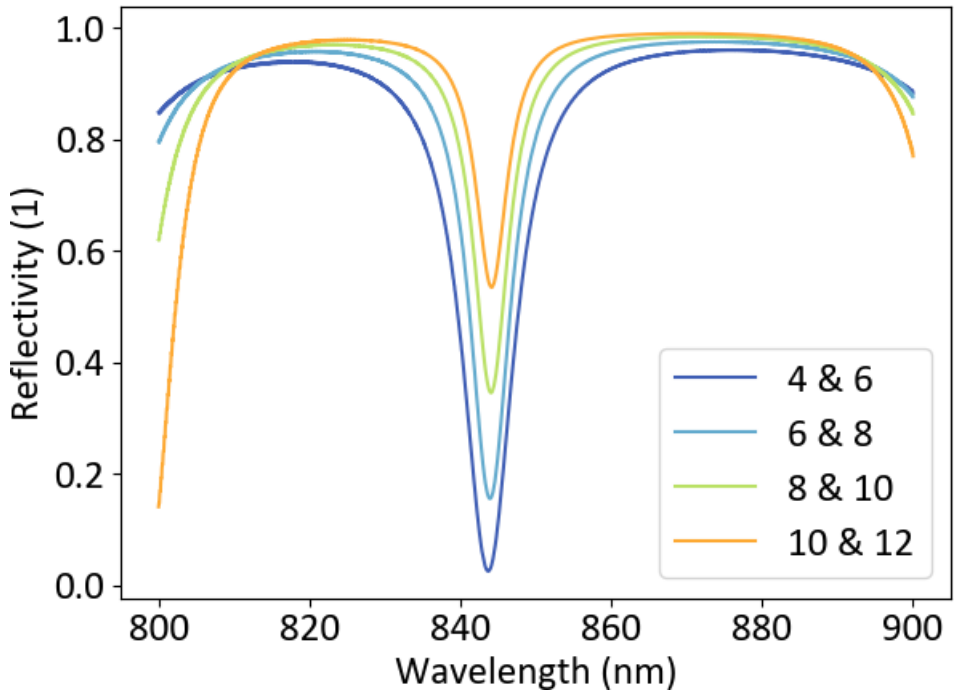

Figure 14: Reflectivity of the asymmetric Fabry-Perot structure for different periods of the DBRs cavity composition from table 3 (in legend resp. top and bottom amount of periods) without taking into account the electro-absorption (calculated using TMM).

3.2.3 Heterojunctions' grading

As explained in the introduction of this section, on an electrical point of view the DBRs are extrinsic to the modulation of absorption. Therefore the impedance of the DBR is detrimental to the performance of the EAM. Marigo estimated that the capacitance of the EAM's DBR introduced a time constant almost ten times slower than the one in the optical cavity [36].

The impedance of a material depends on the configuration of its conduction and valence bands. If the conduction band is rather flat, or has a fluctuation of around the thermal voltage, which corresponds to an electron kinetic energy of $25.8meV$ at $300K$, the resulting impedance will be rather low [54]. Since the band-edge difference between intrinsic $AlAs$ and $GaAs$ is around $130meV$ for the electrons and $600meV$ for the holes, the impedance that results from an heterojunction structure such as a Distributed Bragg Reflector is quite high.

The poor conductivity of a heterojunction stems from the abrupt potential change between a layer with high aluminum content and one with low content. An effective approach to reduce impedance is by minimizing potential spikes, which can be achieved by creating a gradient in aluminum content between the two layers. However, since the

maximum reflectivity of a Distributed Bragg Reflector is attained when the interfaces are most abrupt, introducing grading adversely affects the optical properties of the device, but not in a critical way for 6 or 8 periods.

During molecular beam epitaxy, when growing a layer of $AlGaAs$, we have an operable cell for each element, which provides the material necessary for the epitaxy. The growth speed of a layer and its ratio between aluminum and gallium content depend on the cell temperatures. To create a grading of $AlGaAs$ with a linear slope of aluminium content, the temperature of the cells would need to be continuously modified. Since temperature modification is quite time-consuming, and the epitaxy process is already long, costly, and subject to a global growth rate drift that would worsen with extended epitaxy, implementing such a method is not feasible. However, since we have two cells available for each of the Ga and Al elements—one dedicated to fast growth and the other to slow growth—we can produce $AlGaAs$ layers with aluminum compositions of either 0%, 15%, 90%, or 100%. This capability allows us to grow digital alloys [55], which involve creating short-period superlattices [56].Instead of adjusting the growth speed, we modulate the opening and closing times of the cells' shutters. This modulation results in an average composition that mimics an alloy with a continuous variation in composition. This digital alloy has equivalent electrical and optical properties to such a continuous alloy. Figure 15 shows the profile of a $20nm$-wide digital alloy grading

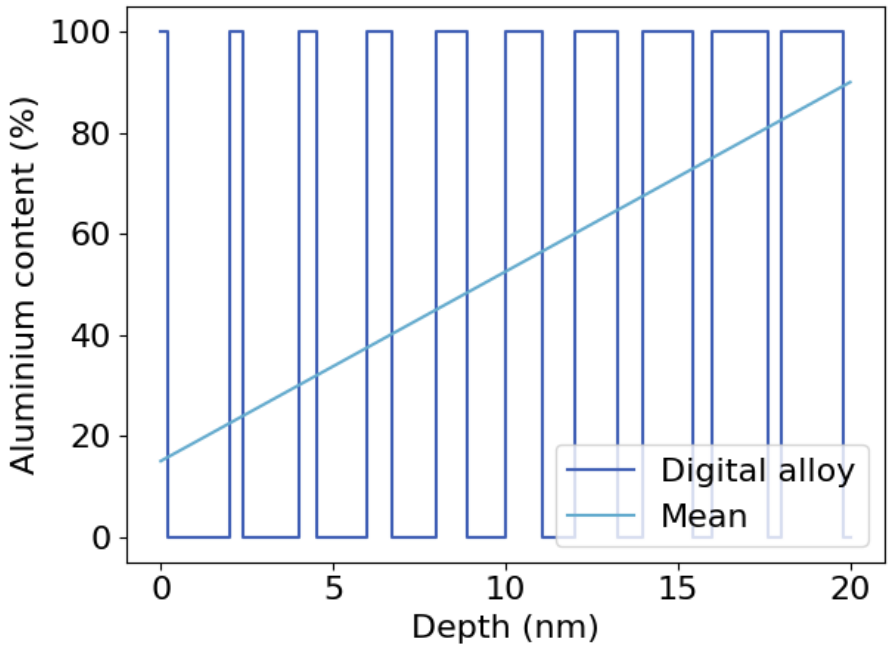

Figure 15: Aluminium profile of the grading of an heterojunction.

which can be introduced at a DBR interface, going from an average aluminium content

from 15% to 90%. The mean value is calculated by multiplying each layer thickness by its aluminium fraction over the $20nm$. This grading will be used at each interface between high aluminium fraction and low aluminium fraction layers of every DBR.

3.3 EAM-VCSEL design

3.3.1 EAMs designs

3.3.1.1 EAM structure 1: standard EAM

The standard structure of the electro-absorption modulator is based on the original design by Marigo Lombart. In accordance with section 3.2.2, the top DBR contains 6 periods, while the bottom one contains 8, with the introduction of $20nm$-thick digital alloy gradings at the interfaces. Regarding the optical cavity, as discussed in section 3.1.3 on charge carrier evacuation, the fraction of aluminum in the confinement barrier is reduced to 21%. To be consistent with our figure of merit (Figure 11), QWs thicknesses are set to $8.27nm$. Since the MQW stack must be a multiple of the half-wave thickness, the EAM optical cavity ends up containing 25 QWs, and claddings of $8nm$. Table 3 lists the layers of this structure.

Layer	Repetition	Al (%)	Doping ($at.cm^{-1}$)	Thickness (nm)
Top contact	1	0	N 5×10^{18}	50
Top DBR	1	90	N 2×10^{18}	69.9
Top DBR	6	15	N 2×10^{18}	60.7
Top DBR	6	90	N 2×10^{18}	69.9
Cladding	1	21	0	8
Quantum Wells	25	0	0	8.27
Confinement barriers	24	21	0	10.3
Cladding	1	21	0	8
Shared DBR	1	90	P 2×10^{18}	69.9
Shared DBR	8	15	P 2×10^{18}	60.7
Shared DBR	8	90	P 2×10^{18}	69.9
Middle contact	1	15	P 5×10^{18}	162.1
Shared DBR	1	90	P 2×10^{18}	69.9
Shared DBR	12	15	P 2×10^{18}	60.7
Shared DBR	12	90	P 2×10^{18}	69.9

Table 3: Layers of the EAM structure 1.

3.3.1.2 EAM structure 2: shared DBR bypassing

The impedance that is extrinsic to the absorption modulation could be reduced to zero if the electrodes of the EAM were placed at the ends of the EAM cavity. Shifting the top contact between the top DBR and the cavity would complicate the fabrication process, but moving the middle contact next to the EAM cavity would not require any additional fabrication steps. In this new configuration, the QWs, confinement barriers, and top DBR are identical, and the only difference comes from the location of the middle contact layer as seen in table 4.

Because the bottom DBR is essential for achieving resonance within the cavity, it is positioned beneath the contact layer. As a consequence, the top DBR of the VCSEL gains an additional 8 periods, resulting in increased resistance. However, regarding the VCSEL, the current must already pass through 55 DBR periods and a substrate that is $600\mu m$ thick. Therefore, the additional resistance introduced by these extra 8 DBR periods is negligible.

Layer	Repetition	Al (%)	Doping ($at.cm^{-1}$)	Thickness (nm)
Top contact	1	0	N 5×10^{18}	50
Top DBR	1	90	N 2×10^{18}	69.9
Top DBR	6	15	N 2×10^{18}	60.7
Top DBR	6	90	N 2×10^{18}	69.9
Cladding	1	21	0	8
Quantum Wells	25	0	0	8.27
Confinement barriers	24	21	0	10.3
Cladding	1	21	0	8
Middle contact	1	15	P 5×10^{18}	162.1
Shared DBR	1	90	P 2×10^{18}	69.9
Shared DBR	20	15	P 2×10^{18}	60.7
Shared DBR	20	90	P 2×10^{18}	69.9

Table 4: Layers of the EAM structure 2.

3.3.1.3 EAM structure 3: EAM with oxide aperture

As discussed in Section 2.3.2, an essential consideration when integrating two optical cavities, as in the EAM-VCSEL structure, is the coupling between these cavities. The coupling is theorised during the design phase and set during epitaxy. With the previous structures presented, once epitaxy is completed, there are no options for modifying the coupling. Here, we introduce a novel EAM structure that allows for post-epitaxy tuning of the coupling.

This new configuration builds upon the previous one, where a middle contact layer was positioned directly at the end of the EAM cavity. However, we introduce a new oxidisable layer within the optical cavity. This layer consists of a digital alloy with an average aluminum content of 98% and can be utilised to create an oxide aperture similar to conventional VCSELs, as explained in section 4.3.1. When this layer undergoes oxidation, its refractive index changes while its physical thickness remains constant, thereby altering the optical properties of the EAM cavity. Consequently, it allows us to make further adjustments to the coupling between the EAM and the VCSEL. Table 5 illustrates this novel structure.

Layer	Repetition	Al (%)	Doping ($at.cm^{-1}$)	Thickness (nm)
Top contact	1	0	N 5×10^{18}	50
Top DBR	1	90	N 2×10^{18}	69.9
Top DBR	6	15	N 2×10^{18}	60.7
Top DBR	6	90	N 2×10^{18}	69.9
Low Al layer	1	15	N 2×10^{18}	60.7
Oxide Aperture	1	98	N 2×10^{18}	30
High Al layer	1	90	N 2×10^{18}	28
Cladding	1	21	0	8
Quantum Wells	25	0	0	8.27
Confinement barriers	24	21	0	10.3
Cladding	1	21	0	8
Middle contact	1	15	P 5×10^{18}	162.1
Shared DBR	1	90	P 2×10^{18}	69.9
Shared DBR	20	15	P 2×10^{18}	60.7
Shared DBR	20	90	P 2×10^{18}	69.9

Table 5: Layers of the EAM structure 3.

3.3.2 VCSEL structure

The structure of the single-mode VCSEL closely resembles those found in existing literature, as illustrated in table 6. The VCSEL is grown on a $600nm$ N-type $GaAs$ substrate with a back contact. Initially, a $1\mu m$ buffer layer is grown to mitigate substrate defects. Following this, the first DBR with 35 periods is grown to achieve high reflectivity. The optical cavity consists of 3 QWs and confinement barriers with identical dimensions and aluminum fractions as those in the EAM structures. Subsequently, a 98% aluminum layer is added to create the oxide aperture, which controls the spatial distribution of emitted light. This layer is succeeded by the top VCSEL DBR, comprising 20 periods, shared with the EAM. As a result, in the case of EAM structures #2 and #3, this DBR features 20 periods before reaching the middle contact electrode. Conversely, in the case of the standard EAM structure #1, it consists of 12 periods.

Layer	Repetition	Al (%)	Doping ($at.cm^{-1}$)	Thickness (nm)
Middle contact	1	15	P 5×10^{18}	162.1
Shared DBR	20	90	P 2×10^{18}	69.9
Shared DBR	20	15	P 2×10^{18}	60.7
Oxide Aperture	1	98	P 2×10^{18}	30
High Al layer	1	90	P 2×10^{18}	28
Grading	1	60 → 30	0	90
Cladding	1	21	0	15
Quantum Wells	3	0	0	8.27
Confinement barriers	2	21	0	10.3
Cladding	1	21	0	15
Grading	1	30 → 60	0	90
Bottom DBR	1	90	N 2×10^{18}	69.9
Bottom DBR	35	15	N 2×10^{18}	60.7
Bottom DBR	35	90	N 2×10^{18}	69.9
Buffer	1	0	N 5×10^{18}	1000
Substrate	1	0	N 5×10^{18}	600 000

Table 6: Layers of the VCSEL structure.

3.3.3 EAM and VCSEL tuning

3.3.3.1 Coupling issues between the EAM and the VCSEL cavities

Because the VCSEL optical cavity is a resonant structure, it reflects light back and forth between the DBRs. These reflections create a superposition of waves traveling in opposite directions, leading to constructive interference and the formation of a standing wave pattern. This standing wave propagates into the EAM cavity, where it generates its own standing wave pattern. Figure 16 (a) displays the refractive indices of the EAM-VCSEL structure, with the VCSEL cavity in the middle and the EAM cavity on the left. The optical power distribution along the structure at the VCSEL mode is calculated using the TMM with scattering matrices, as shown in figure 16 (b). The TMM method with scattering matrices has been implemented in a python code based on the methodology described in [50] The light from the VCSEL extends and resonates within the EAM cavity, achieving nearly 100% of the power in the VCSEL cavity.

This case of very strong coupling between the cavities occurs when the emission mode of the VCSEL and the mode of the EAM share precisely the same peak wavelength. As a reminder, these two parameters are interconnected through the following equations:

$$\begin{cases} L_{VCSEL} = \frac{\lambda}{2n} \\ L_{EAM} = 4\frac{\lambda}{2n} \end{cases}$$

The cavities have a very strong coupling when they have a thickness tuned for the same peak wavelength. Thus, it follows that it is possible to reduce the coupling between the cavities by detuning them, i.e. by modifying the thickness of one of them [57]. By doing so to obtain a moderate coupling, we obtain the optical power profile displayed in figure 16 (*c*), where the power in the EAM cavity only reaches around 30% of the power in the VCSEL cavity.

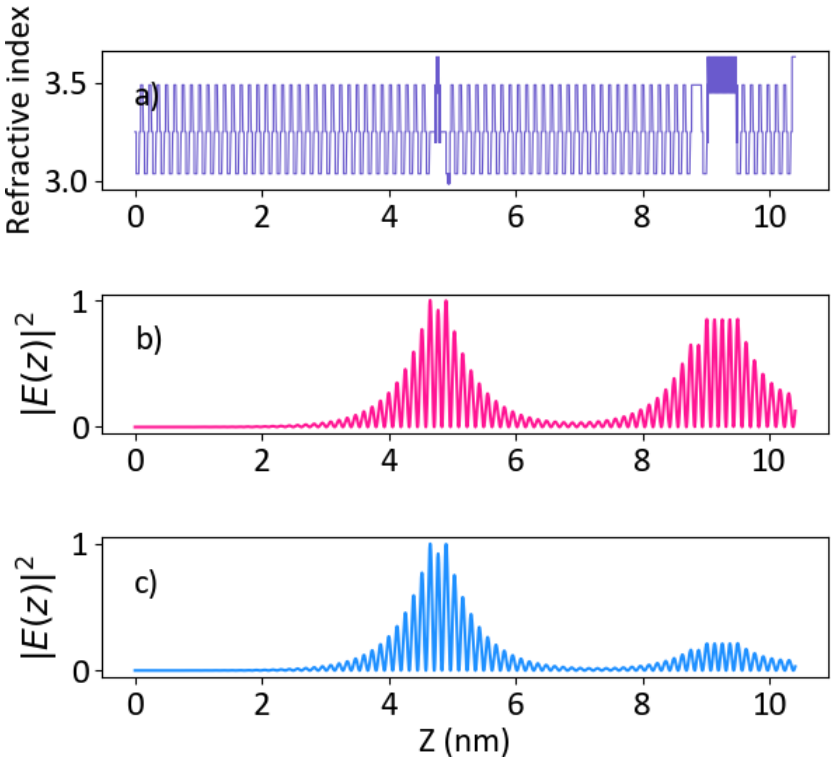

Figure 16: (a) Refractive index profile of the EAM-VCSEL structure with the VCSEL in the middle and the EAM on the left ; Optical power distribution along the device for the composed cavity mode situated primary in the VCSEL cavity for strong (b) and moderate (c) coupling.

One might be tempted to assume that having a strong coupling between the two cavities would be the optimal configuration, however, K. Panajotov and R. Schatz [19] have demonstrated otherwise. They conducted an analytical calculation of the Modulation Transfer Function (MTF) and open-eye diagram for a typical integrated EAM VCSEL structure under conditions of strong, intermediate, and weak coupling between the two cavities. Their findings suggest that, to achieve a higher modulation cut-off frequency, a moderate to weak coupling is more favorable.

Strong coupling can actually degrade performance because, in such cases, when the photons emitted by the VCSEL reach the EAM cavity, a portion of them reflects back into the VCSEL cavity, disrupting its behavior. This perturbation affects the

carrier density within the VCSEL cavity, resulting in irregular modulation limiting the bandwidth. However, as the difference in optical thickness between the two cavities increases, their coupling decreases, reducing the problematic back reflections.

This phenomenon is illustrated in Figure 17. The different colours corresponds to different bias points for the EAM losses $\alpha_{EAM} = 8500cm^{-1}$ (red), $6700cm^{-1}$ (magenta), $5100cm^{-1}$ (green), $3500cm^{-1}$ (blue), 1900 cm^{-1} (cyan), $500cm^{-1}$ (black). In the case of strong coupling (top figure), the modulation transfer function exhibits a declining slope, while in the case of moderate coupling (bottom figure), the response remains flat as the modulation frequency increases.

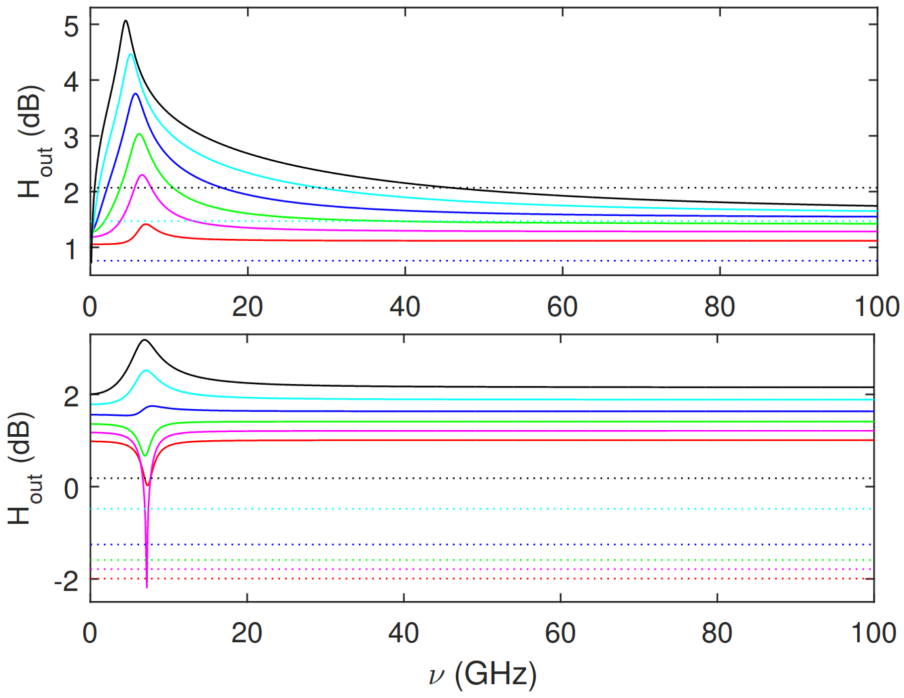

Figure 17: EAM losses α_{EAM} in the case of strong coupling (top) and weak moderate coupling (bottom). The dotted straight lines denote the 3 dB limit for the modulation curves with the same colour. [19]

V. Eisden et al. [58] showed that another method in order to decrease the coupling is to increase the amount of periods within the middle shared DBR that is located between the two cavities. However the amount of periods has to still be inferior to the bottom DBR one. Moreover increasing the periods of the DBR will increase the impedance in a section of the structure which does not participate in the absorption modulation, especially since the DBR between the two cavities is P-type doped. Therefore this structural change is not appropriate for the case of an EAM-VCSEL.

Decreasing the coupling between the two cavities can be achieved by offsetting their

respective Fabry-Perot resonance. The tuning is realised by modifying the thickness of the cladding layers, located at the extremities of a cavity.

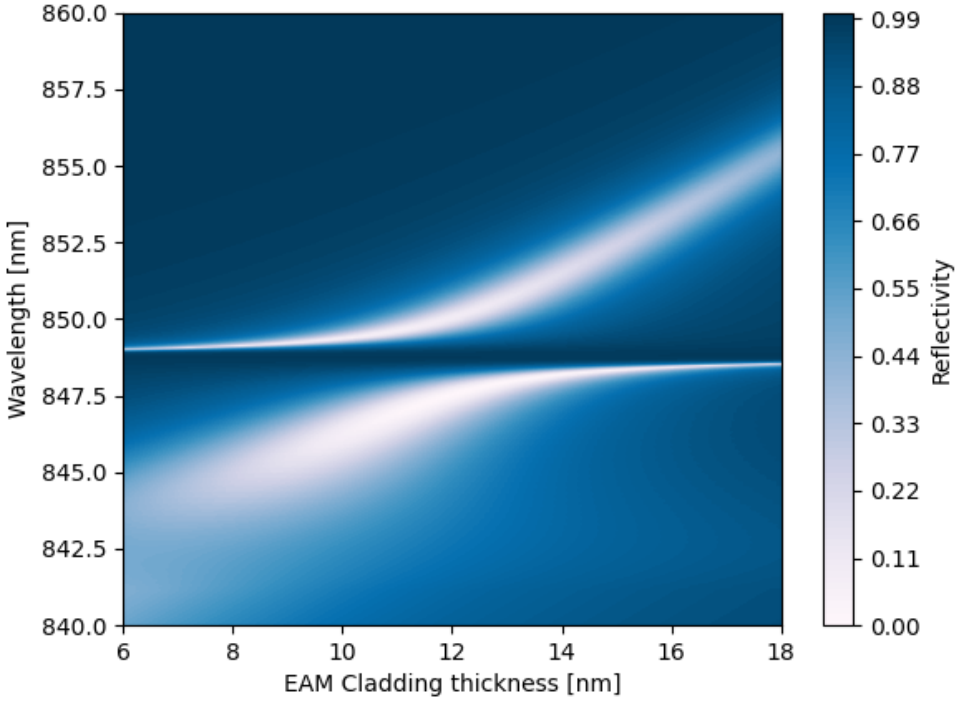

Figure 18: Modes of the coupled EAM-VCSEL, as a function of the detuning between the two cavities, by modifying the thickness of the cladding layers at the extremities of the EAM cavity. The horizontal mode belong to the VCSEL, while the diagonal one belong to the EAM.

Figure 18 illustrates the reflectivity of the EAM-VCSEL for various thicknesses of the cladding layers at the ends of the EAM cavity, resulting in different detuning conditions. The white areas represent low reflectivity zones, corresponding to Fabry-Perot resonances and, thus, the modes of the cavities. The horizontal modes pertain to the VCSEL, while the diagonal ones belong to the EAM.

This figure demonstrates an anti-crossing behavior, wherein, at maximum coupling (around $e_{CLADDING} \approx 12nm$), the two modes do not merge into a single mode. However, when coupling is at its maximum, the cavities strongly interact with each other. M. Brunner [59] explains that when the structure is designed in this manner, the device's behavior becomes unreliable. This underscores the importance of designing a device with weak to moderate coupling and the necessity of precise tuning during the epitaxy step.

3.3.3.2 Method for optimal coupling

To tune the cavities, we need to initially set the wavelength of the VCSEL mode. As depicted in Figure 10c paragraph 2.4.2.2, when the EAM is biased, the absorption undergoes a red-shift. Consequently, for the EAM to absorb the VCSEL light effectively, the wavelength of the EAM mode must be shorter than that of the VCSEL mode.

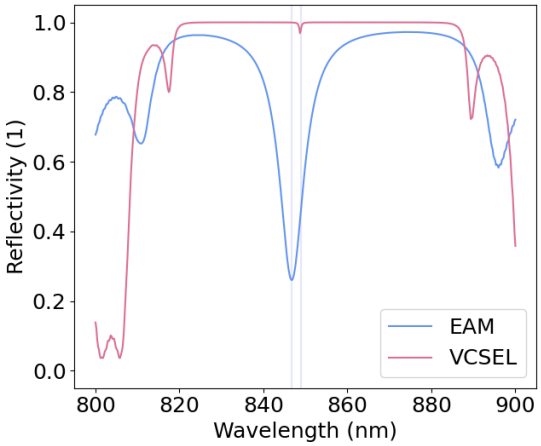

Figure 19: Reflectivity of the EAM (blue) and VCSEL (red) lone structures.

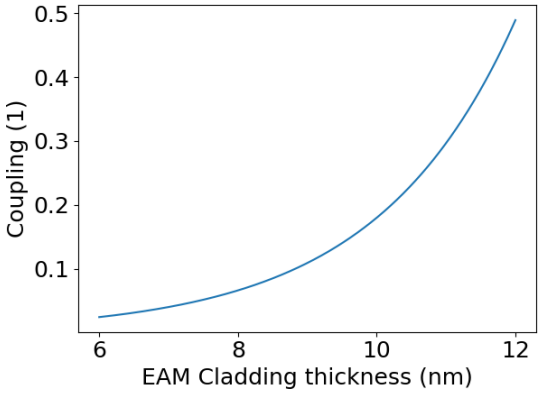

Figure 20: Coupling of the cavities as a function of the cladding layer thickness.

First, the VCSEL is configured independently by adjusting the cladding layers to a thickness of $15nm$. Then, the thickness of the final layer between the VCSEL cavity and the aluminum oxide layer must be modified to achieve a Fabry-Perot resonance at $850nm$, as illustrated in Figure 19 (red curve).

Next, the EAM is configured independently, and once again, the cladding layers are adjusted. This time, the goal is to achieve a Fabry-Perot resonance slightly below $850nm$. This is because the EAM mode needs to have a shorter wavelength than the VCSEL mode to ensure that the red-shifted absorption aligns with the VCSEL mode.

With both structures now prepared, they can be integrated into a single device. Finally, the EAM cladding layers must be modified to achieve the desired level of coupling. We define coupling as the ratio of the maximum electromagnetic amplitude in the EAM to that in the VCSEL (calculated at the VCSEL mode wavelength). In Figure 20, we present the coupling ratio as a function of the EAM cladding thickness. Moderate coupling is achieved at a ratio approximately between 0.1 and 0.3, which corresponds to a cladding thickness of around $9nm$.

With the appropriate configuration, we can compute the reflectivity of the entire structure using TMM, as demonstrated in Figure 21, and the electromagnetic amplitude

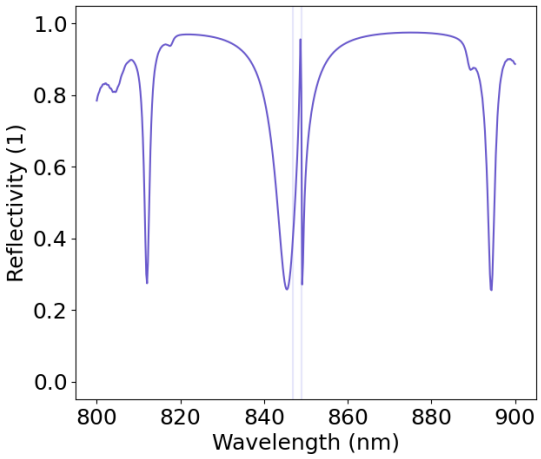

Figure 21: Reflectivity of the EAM-VCSEL structure. The vertical lines (lavender) are at the same location than in figure 19.

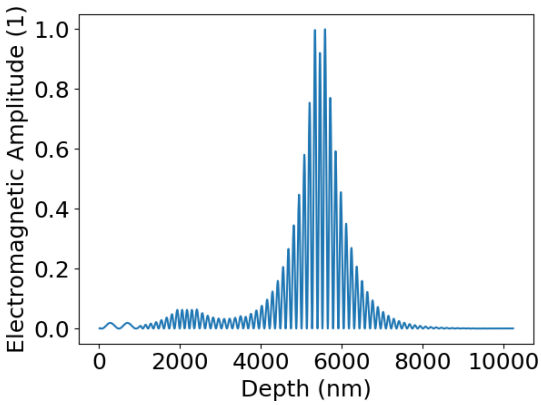

Figure 22: Electromagnetic amplitude along the EAM-VCSEL.

along the structure using TMM and scattering matrices, as shown in Figure 22. These results align with those obtained by K. Panajotov [19].

3.4 Conclusion

This chapter presented the design and the modelling of the EAM-VCSEL, while taking into account Marigo-Lombart's previous take on the design, and current trends on VCSEL, EAM and double cavity research. The purpose was to improve the original design to achieve better RF performances.

The configuration of the Quantum Wells (QWs) and confinement barriers has been optimised based on calculations of absorption modulation depth and charge carrier escape time. This optimisation aims to enhance the absorption contrast ratio and facilitate charge carrier evacuation. Two novel EAM-VCSEL structures have been designed. Both feature a contact layer positioned closer to the EAM cavity to reduce impedance and improve high-frequency performance. Additionally, one of these structures incorporates an oxide aperture within the EAM cavity, offering the potential for post-epitaxy tuning of the cavities. Furthermore, recent research findings on the issue of optical cavities coupling have been taken into consideration. The objective is to achieve weak to moderate coupling between the cavities to avoid any detrimental optical interactions that could hinder high-frequency operation.

To further enhance the EAM-VCSEL design, more advanced simulation methods may be required. In this chapter, we used analytical approaches to calculate reflec-

tivity, optical power distribution, and absorption. However, for a more comprehensive analysis of charge carrier dynamics and impedance, the implementation of finite element methods is recommended. This would enable us to explore additional solutions for improving absorption dynamics, such as coupled quantum wells. Ultimately, a combination of both analytical and discrete methods could help strike a better balance between electrical and optical trade-offs.

Our next phase of work involves the fabrication of our device. We need to ensure that each step preserves the integrity of our design and does not compromise its potential performance. Particular emphasis must be placed on the epitaxial process. Given the sensitivity of coupling to the thin cladding layers, it is imperative that the resulting structure closely matches our design specifications.

4 Fabrication

Given the widespread adoption of VCSELs across various domains of applications, their fabrication processes are now well-established and widely understood. However in the special case of the EAM-VCSEL, some essential steps remain challenging. The long lasting epitaxy of several hundreds of different layers requires rigorous calibration and monitoring. In the case of monomode emission, VCSELs require a precise oxidation of an aluminium layer to obtain an aperture of only a few micrometers. Also, for the sake of high frequency operation, the device requires a dedicated micro strip access pad with a polymerizable resist for isolation and packaging.

In the previous chapter on design and modelling, we discussed the critical properties of the EAM-VCSEL in order to improve its performances. We put emphasis on the detuning between the cavities, and the precise design of QWs and confinement barriers for maximum absorption contrast ratio, which strengthen the requirement of an accurate epitaxial growth. Moreover, as L. Marigot-Lombart's EAMs Fabry-Perot wavelength of its samples ranged from $830nm$ to $870nm$, we need to get more consistent toward a target of $850nm$.

This chapter tackles the topic of the EAM and EAM-VCSEL fabrication from epitaxy to packaging. In this context, the process is thought to be as close as possible to a standard VCSEL process in order to eventually become industry-compatible. However, we introduce some new specific steps to address the critical and unique properties of the EAM-VCSEL.

The first section presents the context of the epitaxy, as well as the specific in-situ monitoring methods we employed to improve our control on the Fabry-Perot resonnance and the detuning. This includes in-situ reflectivity and curvature measurements. We then proceed to present the resulting samples.

The second section presents the problematic of the mesa plasma etching. This step requires careful in-situ monitoring to end the etching at the targeted layer. We address challenges encountered and explore potential solutions.

The third section presents the aluminium oxide aperture to achieve VCSEL monomode emission, and how our in-situ monitoring system allow for a precise and reliable aperture.

The fourth section presents the process to create planar micro strip contacts for high frequency. The process involves the use of Benzocyclobutene (BCB), a dielectric and polymerizable resin for packaging. We survey our solutions to improve the planarity of the resin, its firmness post-curing, as well as decrease the contamination resulting from the plasma etching.

The fifth section presents the overall process with a description of all the details needed for the fabrication, as well as our improvements to make the rest of the process more reliable.

4.1 Epitaxy

4.1.1 Principle

The EAM VCSEL stack is grown using Molecular Beam Epitaxy (MBE) [60]. MBE is a method used to grow thin layers of semiconductors, metals or insulators. In this process, molecular or atomic beams of the material's constituent elements are directed onto a substrate surface that is kept at high temperature in ultra-high vacuum. As a result of the reaction between the beams and the substrate surface, a crystalline layer is formed. A molecular beam is emitted by an effusion cell, which contain a pure source material inside a crucible. The material is then heated at a specific temperature to create a material flux through evaporation. Increasing the temperature of a cell increases the evaporation of its material, and therefore the growth speed. The composition of the growing alloy depends on the set of opened effusion cells shutters.

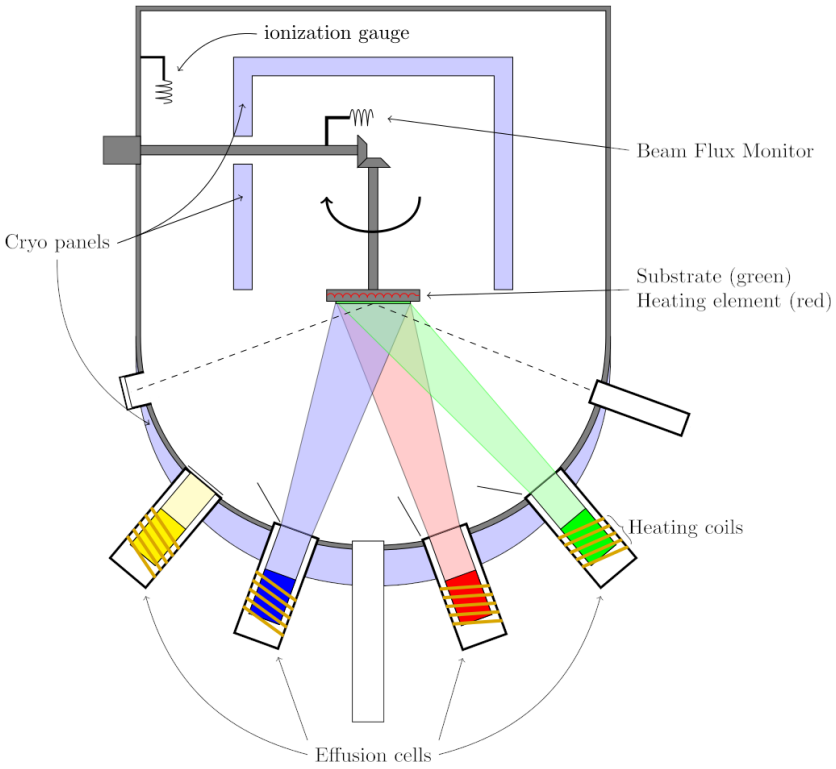

Figure 23: Schematic illustration of the essential parts of a MBE growth system from [61].

The system used is a MBE-412 manufactured by Riber. It consists of a ultra high-vacuum chamber, a substrate holder, a set of effusion cells or Knudsen cells each one equipped with a shutter enabling the blockage or not of the evaporated beam the beam as it can be seen in figure 23. The ultra-high vacuum environment ensures that the

material is transported within the reactor in a the shape of a beam. The substrate holder makes the substrate spins at a slow speed in order to help the deposition to be even and homogeneous on the surface. The most important surface processes involved in the epitaxy, illustrated in figure 24, are the following:

- Adsorption: atoms adhere to the surface of the substrate.
- Surface migration: atoms move around on the surface of the substrate and arrange themselves into a crystalline structure.
- Incorporation of the atoms into the already grown crystal lattice.
- Desorption: the atoms that fail to incorporate in the crystal lattice eventually leave the surface.

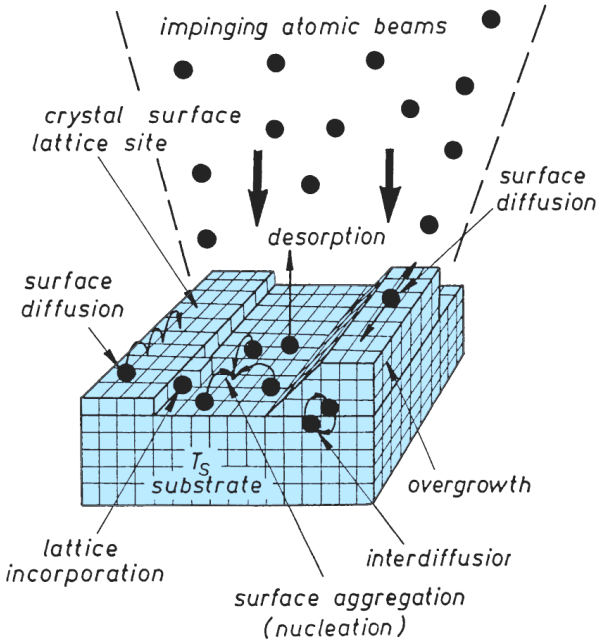

Figure 24: Schematic illustration of the surface processes occurring during film growth by MBE from [60].

The system includes two cells for each gallium and aluminium element, one cell with a slow growth rate and the other with a faster growth rate. Arsenic is evaporated at a constant rate in the chamber from another cell, and naturally combines with as much aluminium and gallium as possible in a crystalline form. The different cells used simultaneously and their combination to grow $Al_xGa_{1-x}As$ with the desired amount of aluminium is summarized in table 7. Considering the growth of gradings or $Al_{0.21}Ga_{0.79}As$ alloys, digital alloys are used as seen in section 3.2.3 and figure 15.

Effusion Cell	Growth rate ($\mu m/h$)	$Al_{0.9}Ga_{0.1}As$	$Al_{0.21}Ga_{0.79}As$	$Al_{0.15}Ga_{0.85}As$	Grading
Ga_{low}	0.1	*	*		*
Ga_{high}	0.85			*	
Al_{low}	0.15		*	*	
Al_{high}	0.9	*			*

Table 7: Effusion cells combinations used for the different $AlGaAs$ alloys grown during the MBE.

The growth rate of this process is typically around 1 monolayer per second or $1\mu m/h$, allowing for the impinging species to migrate on the growing surface resulting in a smooth surface. The substrate temperature is carefully controlled to ensure that the deposited atoms form a single-crystalline layer. Typical conditions for $AlGaAs$ MBE growth use a substrate temperature nearly around $550°C$.

N-type doping in $AlGaAs$ is achieved by simultaneously evaporating silicon from an effusion cell, following the same process used for growing aluminum, gallium, and arsenide components [62]. This involves the use of two separate cells: one for achieving a doping concentration of approximately $5 \times 10^{18} at.cm^{-3}$ and another for reaching a concentration of around $2 \times 10^{18} at.cm^{-3}$. It's important to note that in the MBE412 system, the maximum achievable silicon doping concentration is approximately $\approx 1 \times 10^{19} at.cm^{-3}$.

P-type doping is achieved by direct evaporation of carbon tetrabromide (CBr_4) [63] [64]. The process involves heating CBr_4 and employing a pressure control system to regulate the vapor flow, thereby achieving evaporation. The maximum carbon concentration in $AlGaAs$ achievable by the MBE412 system is $\approx 1 \times 10^{20} at.cm^{-3}$.

4.1.1.1 Wafer curvature

Curvature refers to the deviation of a curve or surface from being straight or flat, respectively. The curvature of a point on a differentiable curve is determined by the osculating circle, which is the circle that most closely approximates the curve in the vicinity of that point. For curves, the curvature of a circle κ is inversely proportional to its radius R, following:

$$\kappa = \frac{1}{R} \tag{39}$$

For instance, a straight line has a curvature equal to zero.

As it can be seen in figure 25, the lattice constant of $Al_xGa_{1-x}As$, which is the length of edges of the unit crystal cell, slightly increases with the fraction aluminium. The

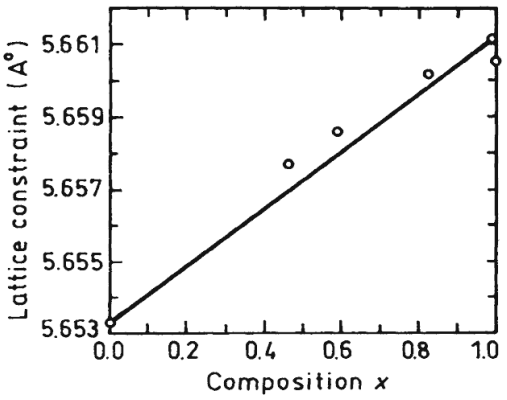

Figure 25: Lattice constant of $Al_xGa_{1-x}As$ as a function of the fraction of aluminium x [67].

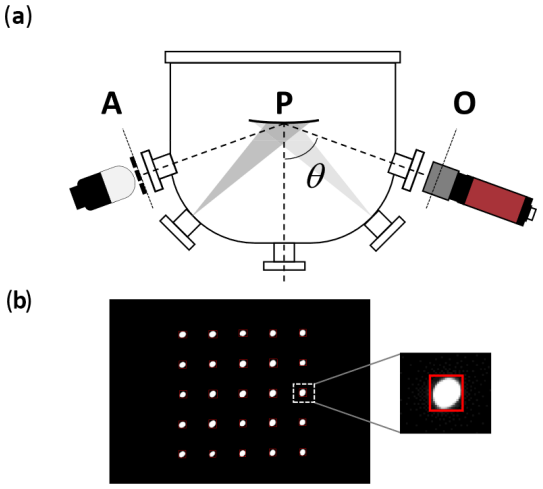

Figure 26: (a) Experimental configuration of the curvature measurement system. (b) Matrix of dots projected on the wafer [65].

lattice constant difference between different alloys of $Al_xGa_{1-x}As$ is at max 8×10^{-3}Å, which is low enough to have a low amount of lattice mismatch, however it stills have the effect to strain and bend the wafer. Thus, a curvature measurement during the epitaxy allows us to monitor and check the mean aluminium content deposited per time unit. Moreover, a loss of linearity of the curvature changes allows us to identify an erratic variation of an epitaxy parameter such as the growth rate, or the substrate temperature [65]. Additionally, K. Louarn [66] demonstrated that measuring the curvature is a useful method to verify that strained layers do not relax due to the formation of cross-hatch dislocations. This kind of brutal relaxation typically induces a sudden unexpected slope change in the curvature. Finally the curvature measurement can be compared to previous measurements of similar devices to confirm reproducibility, and prevent most epitaxy errors. While the structure is unconventionally thick for a structure grown by MBE, the lattice mismatch of the different alloys is generally low and no dislocations have ever been observed.

The experimental setup to measure the curvature during the epitaxy consists of a luminous object which projects a matrix of dots, and a camera with an objective (figure 26 a). The matrix of dots (figure 26 b) is projected on the wafer, and its reflection is captured by the camera. The reflected image is distorted by the curvature of the substrate, and the curvature coefficient is then calculated based on the comparison of the distance between each dots with the original image.

The real-time in-situ measurement of the wafer relative curvature is showed in figure 27. At $t = 0$, the epitaxy starts, and the measured curvature is the one from the factory substrate. A zero slope indicates that the material on the surface is intrinsic $GaAs$,

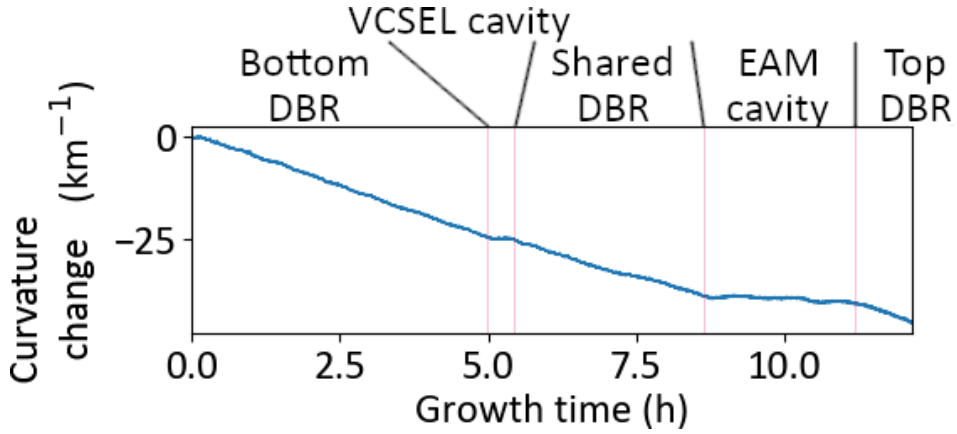

Figure 27: Real-time in-situ wafer relative curvature change of the EAM-VCSEL during the epitaxy.

and the growing layer has a perfect lattice-matching to the substrate, while increasing the amount of dopants or aluminium would create compression seen as a decreasing slope. The first slope between 0 and 5 hours of growth time corresponds to the bottom DBR, which has a mean aluminium content of 52.5%. The slope decreases at a rate of $-5.0 km^{-1}.h^{-1}$. When growing the shared DBR, the slope is of $-4.8 km^{-1}.h^{-1}$. The small difference between the slopes could be explained by the growth speed drift that the effusion cells typically undergo during a long lasting epitaxy. The optical cavities contain quantum wells and confinement barriers. Their average aluminium content is of 12% which is lower than the DBRs. Therefore when the optical cavities are grown, since the lattice constraint is inferior to the DBRs one, the curvature has a slope of $-0.7 km^{-1}.h^{-1}$ (between 9 and 11 hours of growth time).

The similarity in curvature slopes among the different DBRs suggests that they have been grown with a consistent mean aluminum content, indicating compliance with the designed structure. Since the wafer experiences less mechanical constraint when alloys with a lower fraction of aluminium are grown, the flattening of the curvature slope during the growth of optical cavities is consistent. Moreover, the results show no sudden unexpected change of the curvature which imply no major mechanical relaxation that would be detrimental to the device integrity.

4.1.2 Real-time in-situ measurements

4.1.2.1 Reflectometry

Before growing the actual structures, the epitaxy setup requires a calibration of the growth rates of each effusion cell involved, in order to ensure that the thicknesses of

the grown layers will be consistent with the designed structure. The principle of this calibration is to grow a basic DBR, and make an educated guess of the thicknesses of the individual layers by using X-ray crystallography and specific algorithms. The growth rate can then be deduced by considering the growth time of each layer. This method is not absolute, and the guessed growth rate can be off of a few percents, which is enough to deviate the FP resonance of an optical cavity of a few nanometers. Moreover, effusion cells experience a slight growth rate drift during the epitaxy, due to several factors such as source material depletion over time. This effect is all the more significant in the context of a long-lasting epitaxy, which is particularly relevant as EAM-VCSEL epitaxy processes typically span approximately 14 hours. As seen in section 3.3.3.1, the coupling between the optical cavities of the EAM-VCSEL is extremely sensitive to the layers thicknesses. This underscores the necessity of implementing a method to monitor and adjust the FP resonances during the growth process.

The reflectometry is a measurement of the reflectance of a mono or multilayer stack based on the refraction and absorption in materials and reflections/transmissions at the optical interfaces. During the epitaxy of the structures we used a real-time in-situ setup to measure the reflectance of the growing sample. The theoretical reflectivity of the structure as a function of the growth time can actually be simulated using the TMM. Thus, the measurement could be compared to the simulation to check whether the undergoing epitaxy is occurring as expected. However, one must note that the epitaxy is done at a temperature of around $550°C$, and to our knowledge, there currently are no correct models of the complex refractive index of $Al_xGa_{1-x}As$ at this temperature. The refractive index of $Al_xGa_{1-x}As$ at high temperatures have not been measured thoroughly and the proposed theoretical models are scarce and often not accurate. Nonetheless, the actual FP resonance a cavity can still be evaluated by comparing the reflectometry with previous measurements of similar structures. Typically, for an $Al_xGa_{1-x}As$ DBR with a plateau of high reflectivity centered at $850nm$ at room temperature, increasing the temperature to $550°C$ tends to redshift the center wavelength of the plateau to approximately $885nm$.

A broadband white light source is used to illuminate the wafer at an angle of incidence of 20°. The reflection is analyzed by an Avantes visible and near-infrared spectrometer. A polarizer is placed before the spectrometer in order to measure only the transverse-electric light.

The measured relative reflectivity as a function of growth time is shown in figure 28. The low relative reflectivity is colored in blue, and the high reflectivity is in white. At $t_{growth} = 0$, the epitaxy just starts, and we observe the low reflectivity of the bulk substrate. As the epitaxy progresses in growing the first DBR, we can see the DBR high reflectivity building up. Its maximum reflectivity increases, and its bandwidth narrows as the number of periods increases. The center of this bandwidth that can be used to predict the VCSEL FP resonance wavelength. Once the first DBR is done, the growth

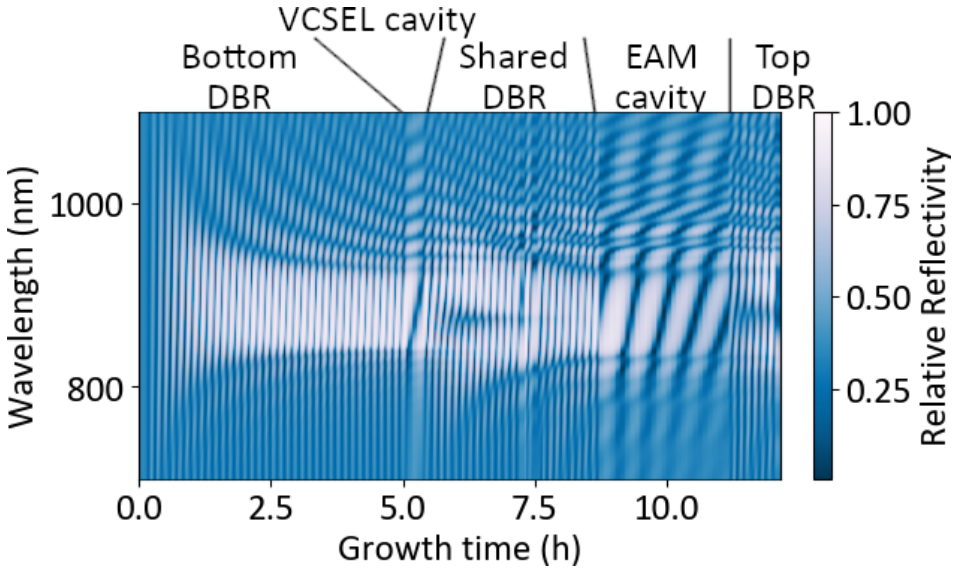

Figure 28: In-situ reflectometry of the EAM-VCSEL during the epitaxy.

of the VCSEL cavity starts. Since its layers are grown with the slow growth-rate cells, this step lasts longer so its corresponding zone in the spectrum is quite visible.

Real-time full spectrum reflectometry enables us to assess the central wavelength of the Distributed Bragg Reflector and consequently monitor the Fabry-Perot resonance wavelength within the cavities. Since the VCSEL mode resides at the midpoint of the DBR plateau, we can predict the actual wavelength of the mode before starting the growth of the VCSEL cavity. If the central wavelength deviates significantly from the target of $850nm$ (or $885nm$ at $550°C$), it becomes feasible to pause the epitaxy process and adjust the growth rate of the cells to realign the Fabry-Perot resonance.

To facilitate this, our simulation algorithm, which calculates the reflectivity of the structure using Transfer Matrix Method (TMM), incorporates a mechanism for recalculating the reflectivity of a given structure based on the growth rates of effusion cells. Consequently, when the growth rate of any selected effusion cell is modified, we can compute the new reflectivity and deduce the extent of the wavelength shift in the Fabry-Perot resonance. This information then guides the adjustment of the growth rate in a dichotomous manner. Once the corrected growth rate V_{T_2} is determined, the corrected effusion cell temperature T_2 can be calculated following:

$$V_{T_2} = V_{T_1} * \exp(\frac{T_2 - T_1}{T_0}) \tag{40}$$

or

$$T_2 = T_1 + T_0 \ln(\frac{V_{T_2}}{V_{T_1}}) \tag{41}$$

with T_0 being a constant representative of the cell, inferred based on previous calibrations, T_1 the current cell temperature, and V_{T_1} its current growth rate. This method

was used during the growth of the EAM-VCSEL 2 (sample A1398), and the results are discussed in the next subsection.

4.1.3 Epitaxy results

Table 8 lists the samples that have been grown by epitaxy, including the FP resonance of their optical cavities measured by FTIR (Fourier-Transform Infrared Spectroscopy). In total, five structures were realised. Two EAMs, one with a contact layer in the middle of the DBR shared by the optical cavities, and one with a contact layer between the EAM cavity and the shared DBR. Two EAM-VCSELs have been grown with the same configurations (a SEM picture of a FIB cut of EAM-VCSEL 1 is showed in figure 29). And finally a third EAM-VCSEL which include the possibility to realise an oxide aperture for the EAM to eventually be able to modify the tuning between the cavities post-epitaxy. On the bright side, the FP resonances are very close to the targeted $850nm$. The EAM FP resonances ranges from $848.4nm$ to $855.2nm$, while the VCSEL ones range from $841.5nm$ to $850.4nm$. This is a good improvement in comparison to Marigo-Lombart's results which ranged from $830nm$ to $870nm$, and has been made possible thanks to the deployed real-time in-situ measurements. On the downside, EAM-VCSELs 1 and 3 seems to have the FP resonance of their optical cavities merged, which is strongly detrimental to their potential performances. However, we should note that EAM-VCSEL 2 has a correct configuration, with an FP resonance of the EAM slightly inferior to the VCSEL one as intended. Since this sample is the one where we deployed our method to adjust the FP resonance of the cavities during the epitaxy by considering real-time in-situ reflectivity measurements, this result tends to confirm the importance of these measurements for our FP resonance adjusting method.

Structure	Sample	EAM FP (nm)	VCSEL FP (nm)	Properties
EAM 1	A1379	851.5		Contact in the middle of the shared DBR
EAM 2	A1380	855.2		Contact between the shared DBR and the EAM cavity
EAM-VCSEL 1	A1397	841.5	841.5	Contact in the middle of the shared DBR
EAM-VCSEL 2	A1398	848.4	850.4	Contact between the shared DBR and the EAM cavity
EAM-VCSEL 3	A1399	848.6	848.6	Include an oxide aperture in the EAM

Table 8: Table listing the different structures grown by epitaxy and the FP resonance of their cavities.

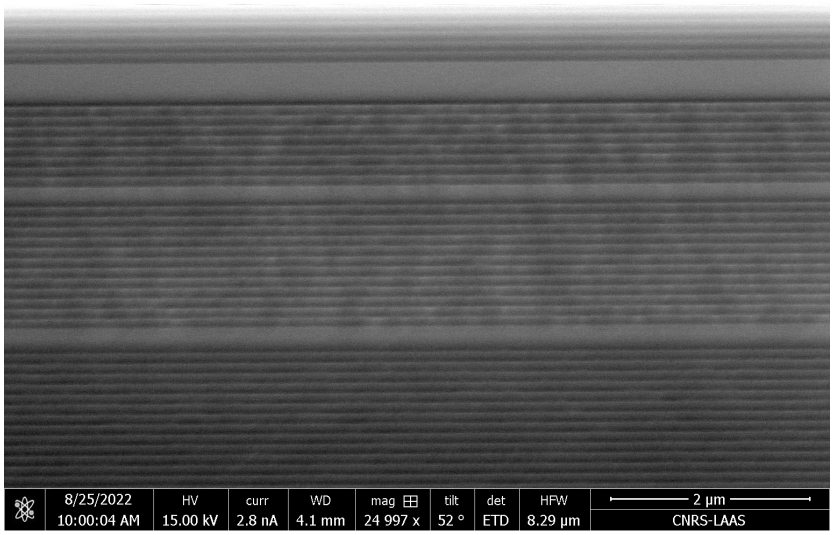

Figure 29: SEM picture of the FIB cut of the EAM-VCSEL 1 post-epitaxy.

The results of the epitaxy, the in-situ measurements, and their implications were presented at the 22nd International Conference on Molecular Beam Epitaxy (ICMBE 2022) [68].

4.2 Mesa etching

4.2.1 Plasma mesa etching principle

Once the epitaxy is done, the first step to realise the EAM-VCSEL device is to etch the EAM mesa. On the top of the will-be mesa, a ring of $50nm$ of titanium then $500nm$ of gold is deposited by evaporation for the purpose of the top contact. The high resistance of gold to the plasma will ensure a quality profile on the edges of the mesa. The inside of the ring, and thus the cap of the mesa, is protected by a photolithography of $2.4\mu m$ of $SPR700$ resist. The etch will go through the top DBR, the EAM cavity that contains the 25 quantum wells, until the $170nm$ thick layer dedicated to the middle contact is reached. The layers to etch are made out of $AlGaAs$ with a proportion of aluminium ranging from 0% to 85%. To serve this objective, we use a chlorine CL_2 $20sccm$ and nitrogen N_2 $50sccm$ plasma at $28°C$. It is mandatory that the etching is stopped as soon as the contact layer is reached, as etching the entirety or too much of this layer would make the electrical contact impossible. For this purpose an in-situ control of the etching is required, to ensure an optimal etching timing.

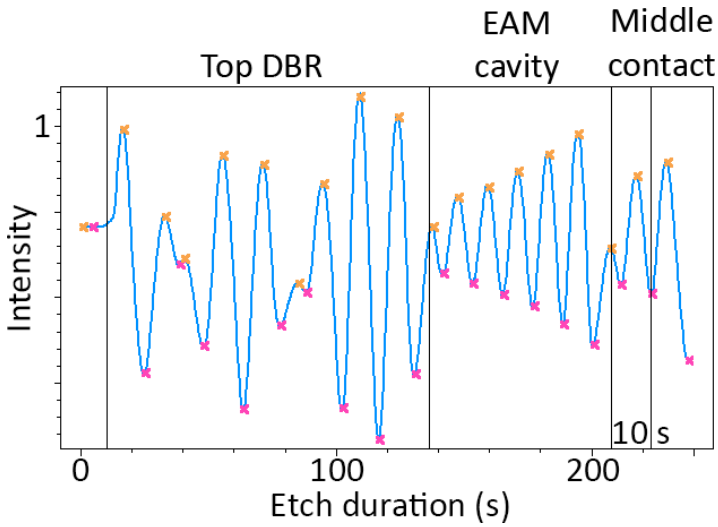

Figure 30: In-situ real time reflectometry signals of the end-point detection system during the plasma etching of the first mesa of the EAM-VCSEL. The window when the etching must be stopped is delimited by the black vertical lines.

4.2.2 In-situ etching depth monitoring

The in-situ real-time control of the etching depth is realised by reflectometry. As the etching of the layers progress, the reflectivity of the surface changes periodically. The result can be seen in figure 30 with the in-situ monitoring of the EAM from section 3.3.1.2. Etching the top DBR takes $\approx 150s$, while the EAM cavity takes $\approx 60s$ with an overall etch rate of $\approx 7nm/s$.

A problem that arises with our design is that the middle contact layer is only $170nm$ thick, which gives us a short window of approximately $10s$ at best to stop the etching at the right moment, before more than half of this layer has been etched. If we take into account the latency of the measurement, the plasma stop lag, and the human reaction time, such a timing is quite tedious. The solution would obviously be to make this layer thicker. As this layer is part of the middle DBR, its thickness $d = 170nm$ follows the quarter-wavelength condition: $d = (2k + 1)\lambda/4n$. Thus, to ensure a better timing control we could make it 5 or 7 times a quarter-wavelength thickness, i.e. $303.66nm$ or $425.12nm$.

4.2.3 Etching non-homogeneity

During plasma inductively coupled plasma (ICP) reactive ion etching (RIE), the etching depth can sometimes exhibit inhomogeneity on the surface, with faster etching occurring at the borders. This phenomenon is often referred to as the "border effect" or

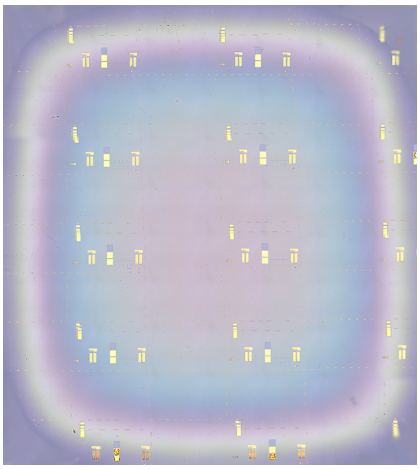

Figure 31: Microscope picture of the whole $6cm^2$ EAM-VCSEL sample after plasma etching of the first mesa.

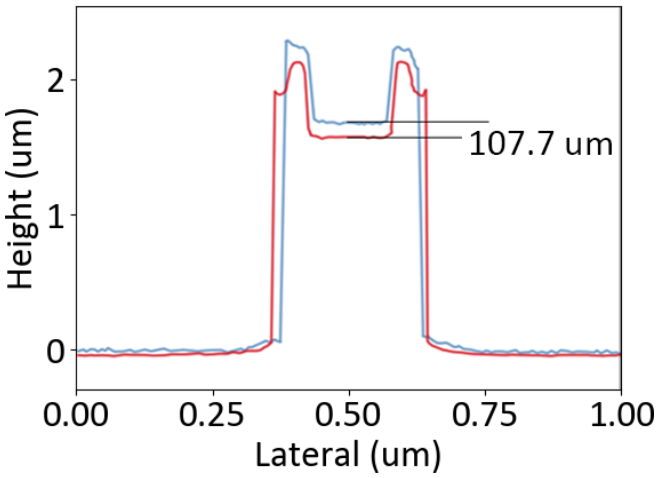

Figure 32: Optical profilometer measurement of two mesa after plasma etching. The mesa in blue is located at the center of the sample, while the red one is on the border.

"etch rate non-uniformity", and comes from factors described below. Figure 31 shows a wide-field microscope picture of the EAM-VCSEL sample right after the mesa etching. The sample displays large aureoles with gradients of colors, indicating a variation of reflectivity of the surface, coming from the variation of the etching depth. After investigation with an optical profilometer (figure 32), by comparing the mesas located in the center of the sample to the ones on the border, we measure a difference of height of $107nm$ that means about the same than the stop-etch layer thickness. There are several factors that could contribute to this behavior:

- In an ICP system, an RF (radio frequency) electromagnetic field is used to generate a plasma. The electric field distribution within the plasma chamber can vary, leading to non-uniform ion bombardment on the sample surface. Near the edges or borders of the sample, the electric field strength can be higher, resulting in enhanced ion bombardment and increased etch rate.

- The sample geometry itself can influence the etching profile and lead to variations in etch rate. For example, if the sample has sharp corners or edges, the electric field and plasma density can be enhanced in those areas, resulting in increased etching.

- When the sample is put in the ICPRIE reactor, it is bonded on a 6" silicon wafer susceptor with fomblin oil. However, $GaAs$ has a lower thermal conductivity than silicon, which means that it has reduced heat dissipation capabilities, and could exhibit temperature variations across the sample. This can affect the chemical reactions occurring during etching. Higher temperatures can increase the etching

rate, while lower temperatures can decrease it. Variations in temperature across the substrate can introduce depth non-uniformities.

The electric field edge effect can't be avoided and we can't afford to work on larger samples. One way to improve the homogeneity of the plasma etching, could be to investigate other cooling temperatures than the current $28°C$. This would require a lot of testing, as modifying the cooling temperature might require to tune the other plasma parameters such as electrical power, pressure and gas flow to obtain similar results. But the most simple way to solve this issue would be, again, to increase the contact layer thickness to avoid the difference of $100nm$ of etching depth to be negligible.

4.3 VCSEL oxide aperture

4.3.1 Principle and purpose

The most significant absorption of the EAM occurs within the excitonic peak, which is characterized by a narrow wavelength range. To achieve the highest absorption efficiency, it is crucial to ensure that the VCSEL incoming light's wavelength and spectral distribution superpose as much as possible with this excitonic peak. Optimizing our device to achieve the highest absorption contrast ratio implies a light emission in a single narrow mode: monomode emission of the VCSEL is mandatory. The suppression of parasitic transverse modes is achieved by confining light emission and charge carriers recombination in a diameter narrower than the VCSEL's mesa. Optical confinement relies on the principle of total internal reflection: when a light ray propagates in a high refractive index medium and reaches the interface with a low refractive index medium at an angle of incidence greater than the critical angle, it undergoes total reflection. This setup can be achieved using a thin layer of $AlGaAs$ with a high fraction of aluminium (above 95%), which is oxidized starting from the mesa sidewalls to form an iris [69]. The oxide is also highly dielectric, and conveys the current lines to the center of the mesa, which increases the concentration of charge carriers and the emission location. In the case of the EAM-VCSEL, single mode emission is required to achieve efficient and fast electro-absorption modulation. Monomode VCSEL emission can be achieved thanks to an oxide aperture with a diameter inferior to $5\mu m$.

Note that in the case of a standard VCSEL modulated by current, several different oxide aperture can be used in the design. They effectively increase the equivalent capacitor thickness, and thus, reduce the capacitance of the VCSEL, improving the impedance and increasing the bandwidth. In 2009, Y. Chang et al. [70] achieved a $35Gbit/s$ data rate with this tapered oxide aperture.

For the purpose of monitoring the oxidation, we designed several dedicated struc-

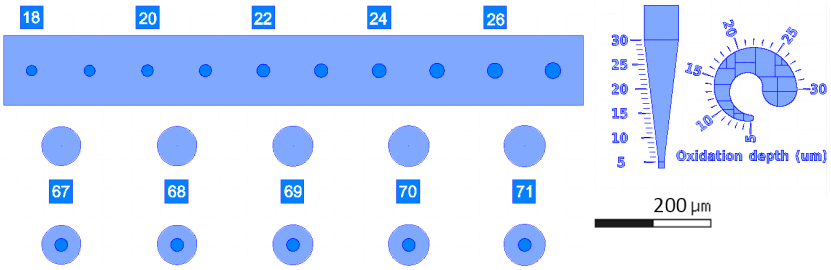

Figure 33: Dedicated mask pattern for aluminium oxidisation monitoring.

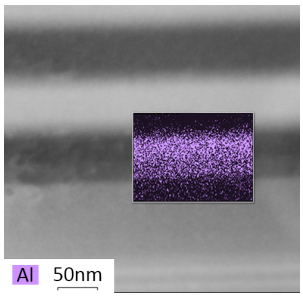

Figure 34: TEM analysis of the oxidisable aluminium layer.

tures depicted in the mask design shown in figure 33:

- A first row with EAM mesa without passivation or metal deposition on the top to monitor the oxidation of the EAM in the case of the structure section 3.3.1.3. The mesas diameters range from $18\mu m$ to $27\mu m$ which is the same range of the other EAM mesas.
- A second row with VCSEL mesas again without any passivation, and without the EAM mesa on top of it to be able to directly observe only the oxidation of the VCSEL. The mesas diameters range from $67\mu m$ to $71\mu m$.
- The third row consist in the regular EAM-VCSEL double mesas without any passivation or metal deposition on the top. They stand for comparison with the VCSEL mesas. The VCSEL mesas diameters range from $67\mu m$ to $71\mu m$, while the EAM mesa on top of them is $24\mu m$ wide.
- Finally we have two different designs on the right to be able to quantify the oxidisation rate.

To ensure that the amount of aluminium fraction incorporated during the epitaxy is high enough to achieve this process, we realized a Transmission Electron Microscopy (TEM) analysis on the corresponding layer (figure 34). This method can realise an analysis of the mean atoms content in a small location. While the oxidisable layer of the VCSEL was designed to have a ratio of aluminium to gallium of 98 : 2, the TEM anlysis measured a ratio of 94 : 6. However, this measurement is an average of the content in an area of a few tens of nanometers, and our oxidisable layer is only $30nm$. This can explain the difference between the intended design and the measurement. Nonetheless, we can conclude that our layer has an aluminium fraction of more than 94%, which is enough for the process.

The oxidation rate is essentially sensitive to two parameters: the aluminium fraction, and the oxidation temperature. High aluminium fraction $AlGaAs$ layers oxidize much

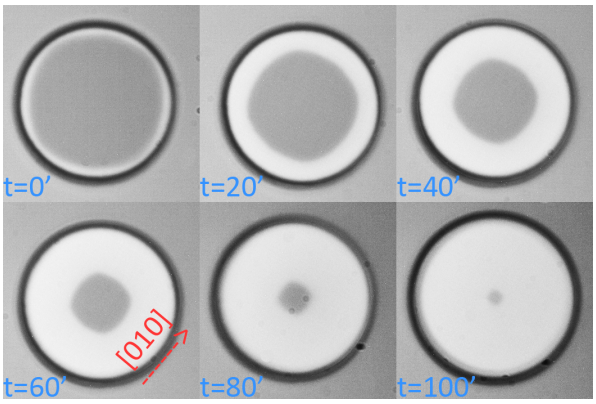

Figure 35: Top view of the creation of an oxide aperture as a function of time with $20min$ intervals of the VCSEL mesa.

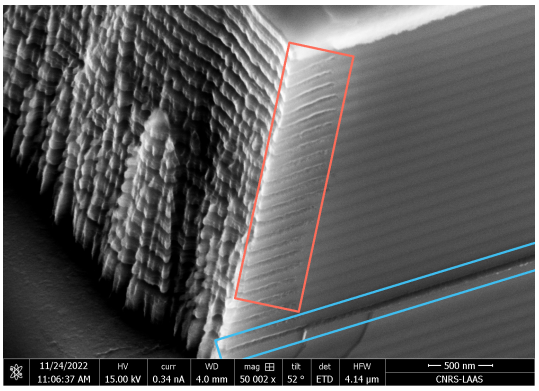

Figure 36: Focus-Ion Beam cut of an oxidised mesa.

faster that the others with lower aluminium fraction. The oxidation rate increases exponentially with the aluminium fraction. Since the aluminium fraction is set during the epitaxy step, and is not a parameter that can be controlled during the oxidation, the oxidation rate is controlled by the temperature set in the oven. However, this parameter is difficult to control, as the oxidation rate increases logarithmicaly with the temperature.

4.3.2 Aperture visualisation

This oxidation being so critical and difficult to achieve, we realize it with the help of an optical in-situ monitoring method. The oxidation oven, made by AET, exposes the sample to a pressure of $500mbar$ with a flux of $1L/min$ of N_2H_2, and $10g/h$ of H_2O, at a temperature of $400°C$ to $450°C$ depending on the desired oxidation rate. The in-situ real-time optical monitoring system to overwatch the oxidation is based on the variation of infrared reflectivity as a function of illuminating wavelength range between oxidised and non-oxidised $AlGaAs$ alloys [71]. It is composed of an infrared Sony XCGH280 camera, a microscope, and a spectrally resolved illumination system consisting of a halogen lamp and a monochromator delivering a narrow band filtered ($\approx 10nm$ wide) spectrum signal tunable over the $670 - 1000nm$ range.

Because of the infrared absorption of the upmost EAM layers, the oxidation of the oxide aperture in the VCSEL is difficult to visualize. To solve this, we use the dedicated pattern structures on the sample previously described, with only the VCSEL structure and a clear surface, where we can properly monitor the oxidation rate. The resulting oxidation is depicted in figure 35, with a top view of the VCSEL mesa during the process with a 20 minutes interval between each picture. We can see the reduction of

the aperture from a diameter of $67\mu m$ down to $2\mu m$ with an oxidation rate averaging $570nm/min$. This aperture can be visualised simply because oxidised and non-oxidised $AlGaAs$ alloys have a different refractive index. Note that the slightly diamond-shaped appearance of the oxide aperture is a result of the oxidation process, which spreads by diffusion at varying rates depending on crystal orientation.

Finally we realised a FIB cut of the VCSEL mesa in order to check the oxidation (figure 36). The oxide aperture layer is framed in blue, and spread as intended. We can also note that, as expected, the other layers with a lower aluminium content have been slightly oxidised over a distance of $\approx 400nm$ at best (red frame).

Since the oxidation might be sensitive to other parameters, such as different strain distribution between sole VCSEL and EAM-VCSEL vertical structure, we suspected that the oxidation kinetic could behave differently for the VCSEL mesa, compared to the EAM-VCSEL double mesas.

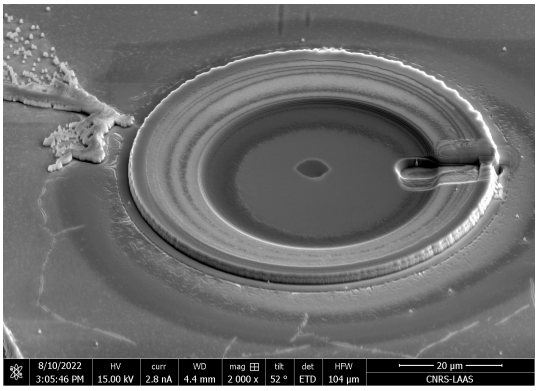

(a) VCSEL's etched mesa with visible oxide aperture.

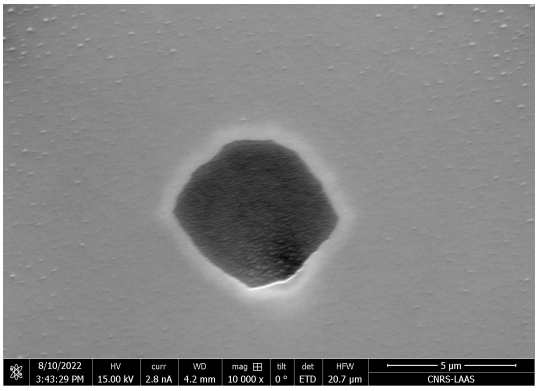

(b) Zoom on the oxide aperture of the sole VCSEL.

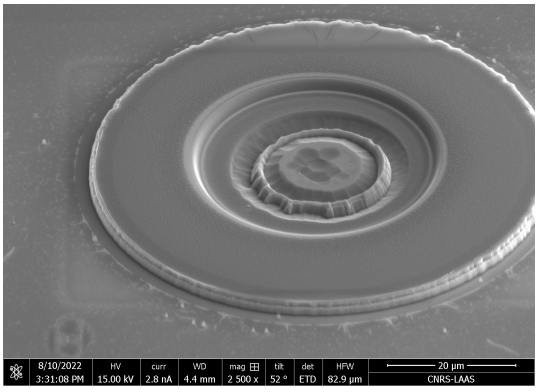

(c) EAM-VCSEL's etched double mesa with visible oxide aperture.

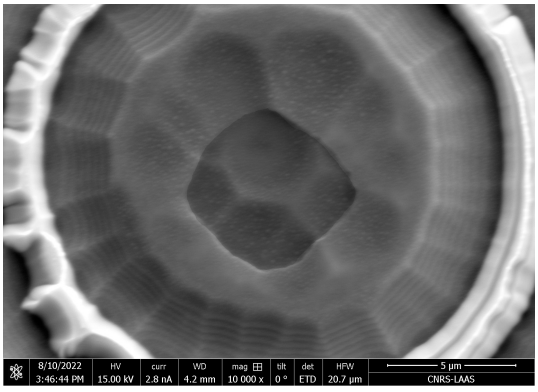

(d) Zoom on the oxide aperture of the EAM-VCSEL.

Figure 37: SEM picture of a FIB etch of the surface of a VCSEL mesa (top) and EAM-VCSEL double mesa (bottom) in order to observe the oxide aperture.

In literature, SEM cross sections of VCSEL mesas to observe the oxide aperture is quite common [72] [73] [74], but in our case, we need to check whether the in-situ observation of the oxide pattern is consistent with the real aperture. For this purpose, we locally etched the surface of the mesa by using Focus Ion Beam (FIB) until the AlO_x layer is reached (figure 37a). A zoom on oxidised region (figure 37b), shows the aperture, with its distinctive diamond shape due to the crystal orientation influence on the diffusion of oxygen during the process. The shape, as well as the diameter of $5\mu m$, is consistent with the in-situ observation.

Now of course, the FIB etch has been realised on an EAM-VCSEL structure as well. Since the etching had to be done all the way through the EAM, it has been subject to edge effects and dust or contamination masking (figure 37c). Nonetheless, once the AlO_x layer was reached (figure 37d), the aperture turned out to be identical to the VCSEL one. Thus, we can conclude that our in-situ measurement is consistent with the real aperture, and that the optimal aperture has been achieved for our sample.

The method for inspecting the oxide aperture using FIB in order to compare it to the in-situ visualisation tool was included in a publication that resulted from a collaboration with the Ph.D. student, N. Monvoisin [75].

4.4 BCB for planar micro strip contacts

4.4.1 BCB for microstrip transmission line

Due to the high bandwidth capabilities of an EAM-VCSEL device, which can extend beyond several tens of gigahertz (GHz), microstrip lines are essential to ensure optimal performance at such high frequencies. The structure of a microstrip transmission line consists of a conductive trace or strip placed on a dielectric substrate, with a ground plane located beneath the substrate. The conductive strip and the ground plane create a transmission line structure that supports the propagation of high frequency electromagnetic waves. Since our structure is a $4\mu m$ mesa and the microstrip lines require to be set on a planar dielectric, we need to apply a flat dielectric material to be able to deposit the microstrip line of the top contact at the same level than the mesa.

This can be achieved with Benzocyclobutene (BCB). It is a chemical compound that belongs to the family of cyclobutene derivatives. It is a high viscosity liquid at room temperature but can be converted into a solid through a curing process. BCB is highly resistant to heat, chemicals, and moisture. Itis also suitable for high frequency applications as it has a stable permittivity versus frequency, low loss tangent, relative low dielectric constant ranging from around 2.7 to 3.1.

The BCB can be applied on a sample with a simple spin-coater. However, after spin-coating the BCB display hills and valleys around the mesas that can reach more than $4\mu m$ of height due to the topography of our sample which features arrays of mesa. Moreover the high viscosity of BCB makes it impossible to end up with a thickness of only $4\mu m$. Indeed, the typical thickness of BCB after spin-coating is around $10\mu m$. Since the microstrip transmission line needs to be planar, it is mandatory to planarise the BCB surface, and etch it to the mesa height.

4.4.2 BCB planarisation

In order to planarise the BCB, we make use of a nano-imprint tool (NX-2500), as described in [76]. The front side of our sample is put in contact with a mold, and the pair is positioned inside the nano-printer, between two flat elastic cushions. The printer then inject gases an, the pattern of the mold imprints on the sample as the pressure increases. The sample is also heated in order to make the resin more fluid during the process, increasing the imprinting effectiveness. In our case, the mold is a simple $4inches$ silicon wafer passivated with hydrophobic and anti-adhesive perfluorodecyltrichlorosilane (FDTS), deposited by Atomic Layer Deposition (ALD) to ensure uniformity and homogeneity of the surface, as well as making the separation of the mold and the sample post nano-imprint more convenient.

This method called Air Cushion Press (ACP) offers significant advantages over traditional Solid Plate Press (SPP) techniques [77]. ACP utilizes conformable gas or fluid layers, ensuring uniform pressure distribution. It prevents lateral shift or rotation between the mold and substrate. ACP avoids "hot spots" caused by localized high-pressure regions. Additionally, the use of pressurized gas with lower thermal mass, combined with efficient heating and cooling implies significantly shorter thermal imprinting times, making ACP very efficient.

In his process, L. Marigo-Lombart set up the nano-imprint equipment to heat the sample at $80°C$ and apply a pressure of $250PSI$ for 6 minutes. However at this time, the temperature sensor was actually erratic, and thus the recipe was unreliable. After repairing the sensor, we realised a set of tests to investigate the optimal parameters. The choice of the temperature value implies a trade-off: higher temperature makes the resin more flexible during the nano-imprinting and improves the process efficiency, as well as make the separation with the mold easier, however, after the process, it makes the BCB harder and less sensitive to the photolithography. In this context, a temperature of $120°C$ showed us the best results. While prior to the nano-imprint, the hills height above the mesa reaches up to $4\mu m$, the planarization with these parameters decreases it down to $\approx 50nm$, while remaining compatible with the subsequent photolithography process.

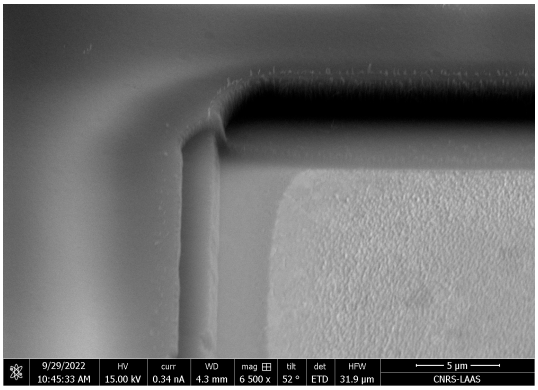

Figure 38: SEM picture of a via after BCB etching.

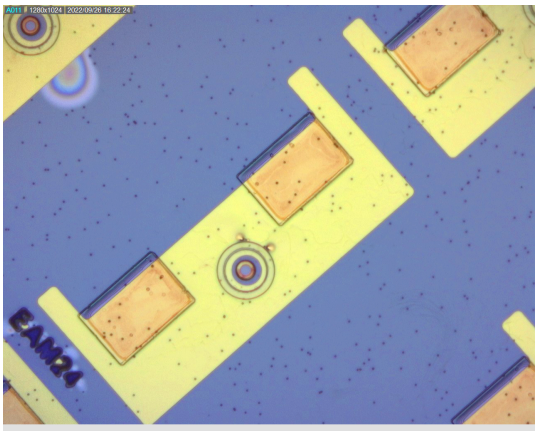

Figure 39: Picture of an EAM VCSEL after etching the BCB vias. An orange contaminant is visible inside the vias.

4.4.3 BCB etching

Right after the planarization, we need to realise vias through the BCB to allow the microstrip line to access the metallic ground plane. Since the BCB is a negative photoresist material, it can be patterned through photolitography to make the vias. The BCB is insulated at $360mJ/cm^2$ and then developed in DS3000 solvent for 10 minutes while being heated. BCB development is very sensitive to the temperature, as when developed at $32°C$, the vias are not fully opened, whereas they are completely opened when developed at $36°C$.

In case the via is not fully opened, we developed a simple process to ensure the opening of the vias down to the ground plane. First a photolithography with the same mask pattern than the BCB vias is realized but this time with $2.4\mu m$ of $SPR700$ resist. The principle is to plasma etch the BCB within the vias, while protecting the BCB elsewhere. The BCB is etched in a plasma of sulphur hexafluoride SF_6 and O_2, in an Inductive Coupled Plasma Reactive-Ion Etching reactor at $17°C$. Consequently, we need to control the etch time to make sure to stop the plasma before all the $SPR700$ has been etched. In this setup, $SPR700$ is etched at a rate of $\approx 8nm/s$, while the BCB has an etch rate of $\approx 4nm/s$. If there is still a lot of BCB at the bottom of the vias, this step can be reproduced several time until the vias are fully opened. Figure 38 shows a SEM picture of a via where the BCB has been etched using this method. Two $SPR700$ photolitographies were made as it can be seen by looking at the profile of the edges. At last, as seen on figure 39, the ground plane is visible and is obviously free of any trace of BCB.

4.4.4 BCB contamination

In order to protect the top mesa when BCB is etched, the sample has been passivated with a layer of SiO_x prior to coating the sample in BCB. Thus, once the BCB is etched, a step of SiO_x plasma etch is required. Initially, we used a plasma of tetrafluoromethane CF_4 to etch the SiO_x. Nonetheless, this tends to deposit an unknown orange contaminant on the surface of the metal contacts, as it can be seen in figure 39. Of course, this contaminant needs to be cleaned away to ensure the integrity of the microstrip line. First of all, etching the SiO_x with a plasma of CHF_3 instead of CF_4 greatly helps reducing the amount of contaminant. Moreover, using a $400W$ plasma of pure O_2 while protecting the sample with a metal cage for 2 minutes, completely removed the orange deposit. We could be worried that this O_2 plasma would etch the BCB but the manufacturer processing procedures for CYCLOTENE 4000 series [78] explain that BCB cannot be etched in pure O_2 or pure fluorine, but require a mix of the two gases. This document also states that O_2 plasma is not suited for BCB descumming, as the BCB contains silicon which is insensitive to O_2. Otherwise, since our previous step consists precisely in removing the silicon, we can consider the O_2 plasma to be appropriate.

4.5 Overall process

This subchapter presents and explains the overall process in order to fabricate the EAM-VCSEL device once the epitaxy is done, to make it ready for use with RF probes. The exact details of the processes for the fabrication of the EAM-VCSEL, including setups, configurations and chemicals quantities are provided in the process file in annex 8.1

4.5.1 EAM top contact

The first step consists in depositing metal on the contact layer of the EAM for the RF signal access as seen in figure 40. The metal pattern is also used as a hard mask for the plasma etching later. The mask's mesa patterns are arranged in arrays, with mesa diameters ranging from 18 to $27\mu m$.

- *Sample cleaning*: The sample with is cleaned with acetone as it is a powerful solvent that can effectively remove contaminants, and then rinsed with isopropanol in order to remove the acetone residue, leaving the sample clean and free from contaminants. The sample is then placed on a hot plate at $100°C$ in order to evaporate the remaining solvent, and make sure the sample is dehydrated.

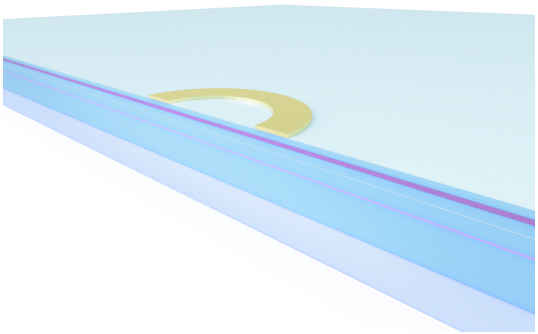

Figure 40: Section cut view of a 3D model of the post-epitaxial EAM-VCSEL after deposition of the top metal contact (in light yellow). The MQW are visible in pink.

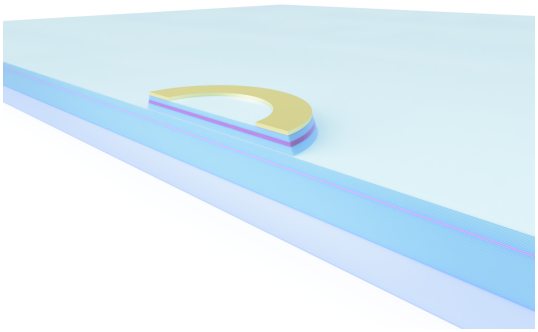

Figure 41: After plasma-etching of the first mesa.

- *Photolithography #1*: By spin-coating, we deposit $2.4\mu m$ of LOR30B resin, then $2.3\mu m$ of SPR700. The sample is then insulated with a mask aligner with a hard-contact. The SPR700 is a positive photoresist, while the LOR30B is not light-sensitive. Thus, after development in Mf Cd-26, the LOR30B is over-etched, creating an undercut which provides better solvent penetration for the lift-off process.

- *Metalization #1*: $AlGaAs$ in contact with air creates a native oxide layer that significantly degrades the electrical contact. Thus the sample is deoxidised with HCl:H_2O 1:10 for 1 minute right before introduction in the deposit frame. We deposit $50nm$ of titanium and then $500nm$ of gold. The metal is deposited by electron beam evaporation, as the evaporation process is more compatible with lift-off than sputtering.

- *Metal lift-off*: The lift-off is done with DMSO heated at $80°C$ as the LOR30B does not dissolve into acetone. The heat obviously fasten the process: typically after half an hour, the metal can be properly lifted by spraying acetone on the sample for a few minutes.

4.5.2 EAM mesa etch

The first mesa is etched down to the middle contact layer between the EAM and the VCSEL as seen in figure 41. The sample is protected by the metal deposited in the previous step, and a photoresist covering the emission window.

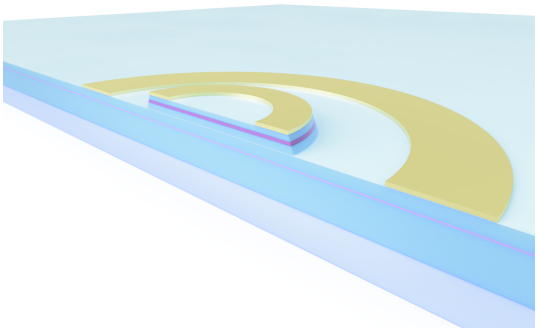

Figure 42: The metal for the middle contact has been deposited.

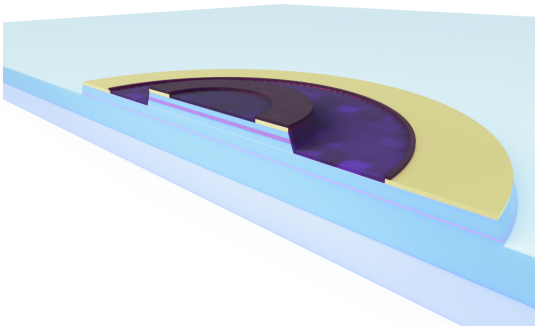

Figure 43: The first mesa is passivated by a deposit of $400nm$ of SiO_x (in deep purple).

- *Sample cleaning*
- *Photolithography #2*: As the purpose of this photolithography is to protect the areas that should not be etched, we only apply SPR700 with the same setup as before.
- *EAM mesa plasma etching*: The EAM mesa is etched by a plasma composed of Cl_2 and N_2, in an Inductive Coupled Plasma Reactive-Ion Etching reactor. The sample is etched until the middle contact layer is reached with the end-point detection system.

4.5.3 EAM-VCSEL middle contact

Metal is deposited on the middle contact layer in the form of a ring circling the EAM mesa (figure 42). It is used as a metal contact, but also as a hard mask for the etching of the second mesa (VCSEL). VCSELs' mesa diameters range from 67 to $71\mu m$.

- *Sample cleaning*
- *Photolithography #3*: LOR30B then SPR700.
- *Metalisation #2*: Ti $50nm$ and Au $500nm$.
- *Lift-off*

4.5.4 EAM passivation, VCSEL etching and oxidation

The EAM mesa is passivated by a deposition of SiO_x and extends by encroaching partially over to the intracavity contact. Then the second mesa is plasma etched (figure 43).

- *Sample cleaning*: It is important to not overlook the dehydration step, as if some micro drops of water gets trapped under the SiO_x deposit, during the several next steps where the sample is heated, the water becomes steam and creates bubbles of SiO_x, and eventually lift-off chunks of SiO_x.
- *SiO_x deposit*: $400nm$ of SiO_x is deposited by Capacitive Coupled Plasma Enhanced Chemical Vapor Deposition (CCPECVD) all over the sample. The CCPECVD deposit is conformal, meaning that the material deposited is being applied in a uniform thickness across all surfaces, regardless of the shape or complexity of the sample. Thus we also have $400nm$ of SiO_x on the slope of the mesa.
- *Photolithography #4*: Only SPR700.
- *SiO_x plasma etching*: The SiO_x is etched by a plasma of tetrafluoromethane CF_4, in an Inductive Coupled Plasma Reactive-Ion Etching reactor. The sample is etched until the end-point detection system detects that no SiO_x remains in the zone with no resist.
- *Second mesa plasma etching*: We can finally etch the second mesa, using the same conditions as the first mesa etch. The etching lasts until the end-point detection system detects that we etched beyond the VCSEL cavity, in the bottom DBR to make sure that the to-be-oxidized Al-rich layer just above the cavity has been reached.
- *Oxide aperture*: See 4.3.1 and 4.3.2.

Figure 44 shows a SEM picture of the EAM-VCSEL double mesa with both $TiAu$ annular contacts, and the EAM SiO_x passivation. Note how the SiO_x pattern slightly covers the middle contact to avoid any short-circuit.

4.5.5 VCSEL passivation

In order to be effective, the microstrip access requires a ground plane of metal below the high frequency pads. This area consist in a rectangle of $450 \times 200\mu m$ centered on the VCSEL mesa as seen in figure 39. To provide a ground contact, this metal layer must be connected to the middle contact, but to avoid any short-circuit, it must be

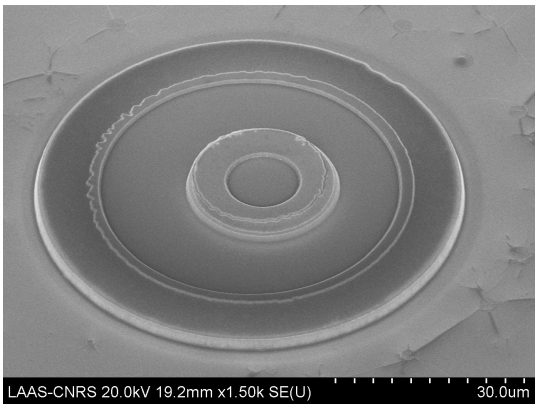

Figure 44: SEM picture of the EAM-VCSEL double mesa with both $TiAu$ annular contacts, and the EAM SiO_x passivation.

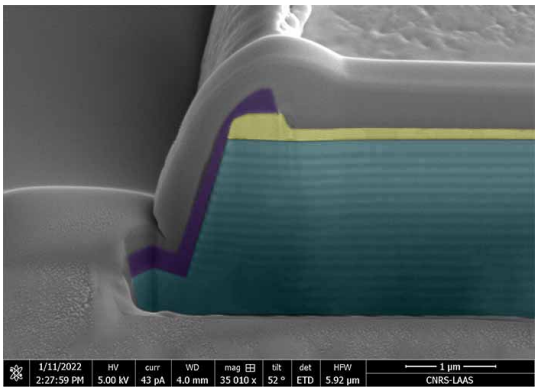

Figure 45: Colorized SEM picture of a FIB etch of the VCSEL after SiO_x passivation.

isolated from the flanks of the VCSEL. For this purpose, a layer of dielectric SiO_x is deposited on the whole surface of the sample, and then apertured at the middle annular contact. The SEM picture in figure 45 shows a colorized FIB cut of the VCSEL mesa after SiO_x passivation. The yellow layer is the $TiAu$ middle contact, the cyan layers are the VCSEL DBRs, and the dark purple is the SiO_x passivation layer. A 3D model of the result can be seen in figure 46.

- *Sample cleaning*
- SiO_x *deposit*: $400nm$
- *Photolithography #5*: Only SPR700. A precise alignement is critical here to avoid any short-circuit
- SiO_x *plasma etching*

4.5.6 Ground contact

Metal is deposited to make a ground plane contact. The metal pattern is in contact with the ring deposited in the second metallization, which is the middle contact in the shared DBR. Outside this ring, the metal pattern sits on the SiO_x to avoid short circuit with the VCSEL cavity. A 3D model of the result can be seen in figure 47.

- *Sample cleaning*

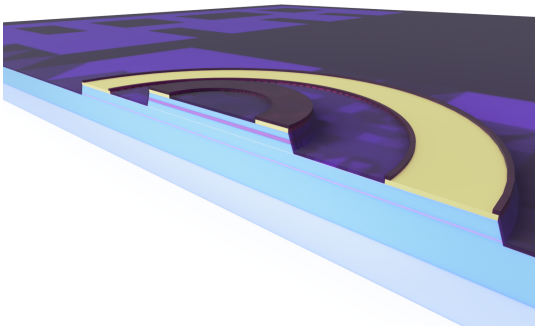

Figure 46: The second mesa has been passivated with SiO_x.

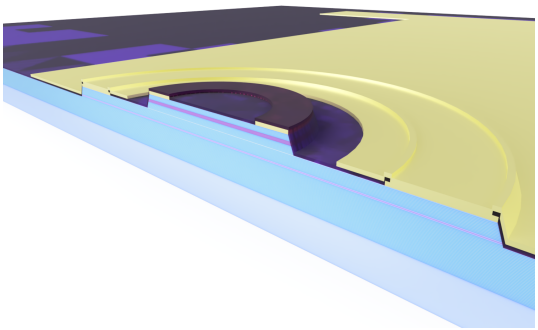

Figure 47: The ground plane deposited on top of the SiO_x layer, in contact with the annular middle contact.

- *Photolithography #6*: LOR30B then SPR700.
- *Metalisation #3*: Ti 50nm and Au 500nm.
- *Lift-off*

4.5.7 BCB planarization

For the operation at high-frequency, the device needs to be driven with RF probes. Therefore, the EAM-VCSEL has been designed with a microstrip access. The microstrip electrical transmission line requires the conductor line to be at the same height level of the top mesa, and a isolating gap with the ground plane formed by a highly dielectric material. The chosen dielectric material is a benzocyclobutene (BCB) resist that can be spin-coated. However, since the BCB is very viscous, and the spin-coating is not completely even across the sample, the BCB needs to be planarized above the EAM-VCSEL devices.

- *Sample cleaning*
- *BCB spin-coating*: First an adhesion promoter (AP3000) is applied on the sample, then BCB is spin-coated at a speed of 6000rpm for 30s, and finally baked at 80°C for 1 minute.
- *Nano-imprint*: For the planarization, the sample is placed on a clean silicon wafer on which perfluorodecyltrichlorosilane (FDTS) has been deposited by Atomic Layer Deposition (ALD) to make it hydrophobic and non-adhesive. Then the

whole is introduced in the nano-printer, where a pressure of $250PSI$ is applied for 6 minutes at $120°C$.

4.5.8 BCB via opening preparation and annealing

The BCB requires to be heated in order to harden and to promote the stickiness of the RF metal pads. This annealing step reduces the BCB thickness of a fraction of approximately 20%. Thus this steps needs to be done before the vias opening by plasma-etching, but after the photolithography since the hardening makes the resin resistant to the developper.

- *Photolithography #7*: The BCB is insulated at $360mJ/cm^2$, and then developped in DS3000 heated at $36°C$ for 10 minutes, and then rinsed in clean DS3000 and then water. Since the DS3000 is not miscible in water, rinsing and drying are difficult. The sample is placed in the spinner, and nitrogen is pulverized on it for further drying action.

- *Annealing*: It is mandatory to anneal the BCB in order to harden it and remove the contained solvent, as it improves its mechanical strength and electrical properties. The Sample is placed in a furnace and is heated up to $250°C$ in N_2 atmosphere to prevent oxygen contamination for 30 minutes. To avoid temperature overshoot and thermal shock that could induce defects, the sample is heated and then cooled with a slope of $100°C/h$.

4.5.9 BCB and silicon oxide plasma etching

The BCB layer and then the SiO_x layer are etched in order to completely open the vias and remove the BCB residuals in it, but also removing the SiO_x that remained on the top of the EAM mesa, which is in the emission window path (figure 48).

- *BCB plasma etching*: The BCB is etched in a plasma of sulphur hexafluoride SF_6 and O_2, in an Inductive Coupled Plasma Reactive-Ion Etching reactor at $17°C$, until the BCB has been etched down to the same level of the top mesa, which is detected with an end-point detection system on a dedicated pattern on the sample.

- *SiO_x plasma etching*: With the same configuration as previous SiO_x etchings, a dedicated pattern on the sample is used to detect when there is no more SiO_x left at the top of the mesas.

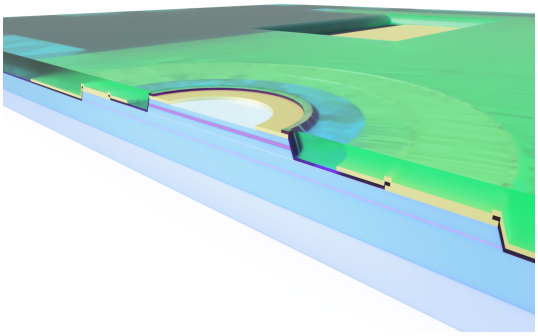

Figure 48: Planarized BCB (in translucid green), and opened vias.

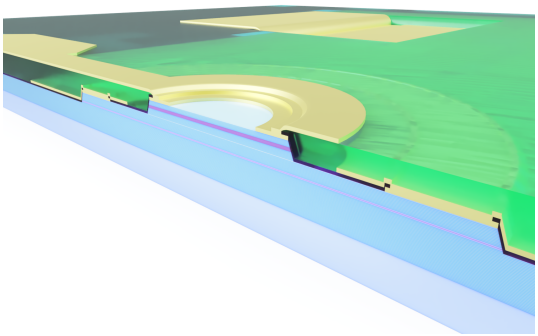

Figure 49: Finished EAM-VCSEL with the micro-strip access deposited on the BCB.

4.5.10 Top HF contact

At this final step we deposit the metal in a pattern compatible with high-frequency probing tests (GSG configuration), which extends into the vias (figure 49). A top-view SEM picture of the completed EAM-VCSEL can be found in 50a. In the zoom of the EAM access in figure 50b, we can see that the microstrip line is actually very close to the middle contact. In this zone, the gap between the two metal layer is of only $\approx 2\mu m$, which put emphasis on how critical the BCB planarization step is.

- *Sample cleaning*
- *Photolithography #8*: LOR30B then SPR700.
- *Metallization #4*: $50nm$ of titanium, then $500nm$ of gold is deposited. The pattern is a planar micro-strip access for the purpose of high-frequency operation. At this point, it is important for the BCB to be correctly annealed in order for it to harden, and to allow the metal to adhere to its surface. The BCB should be hard enough for the metal to stick on, however excessive applied force such as during spin-coating can cause metal to rip off.
- *Lift-off*

4.6 Conclusion

In this chapter, we have presented the entire manufacturing process for an EAM-VCSEL. While many of the steps resemble those encountered during the fabrication of

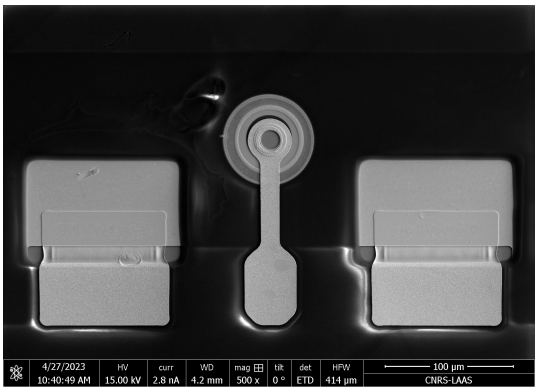

(a) Top overview.

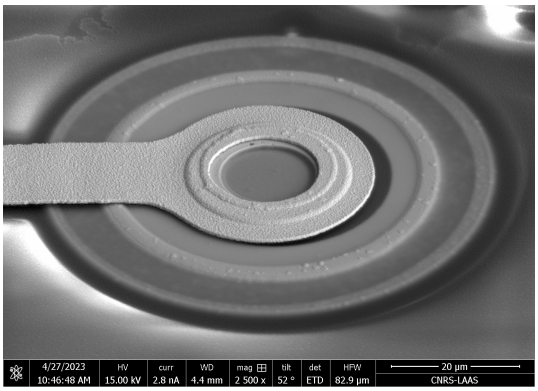

(b) Zoom on the EAM mesa.

Figure 50: SEM pictures of the finished EAM VCSEL with the micro-strip access.

a standard VCSEL, we emphasized the specific details relevant to the EAM-VCSEL.

In the epitaxy phase, we produced five different samples, all of which achieved an FP resonance close to the targeted $850nm$. Notably, Sample EAM-VCSEL 2 demonstrates significant potential due to its effective tuning of optical cavities. This achievement is attributed to a method that combines in-situ reflectivity measurements with the TMM to correct the growth rate of a cell, resulting in improved tuning.

We successfully achieved the oxidation of a high aluminum fraction layer, resulting in an ideal oxide aperture measuring just a few micrometers for the VCSEL. This accomplishment was made possible through the extensive use of a dedicated in-situ measurement technique for monitoring the oxidation process. Additionally, we conducted FIB etching to confirm that the visualized aperture aligned accurately with the actual oxide aperture.

The BCB packaging step has seen substantial enhancements. We have improved the nanoimprint process to enhance the adhesion and durability of microstrip metal access on BCB, all while maintaining the resin's sensitivity to photolithography. Furthermore, we've revised the plasma etching process to minimize contamination during BCB etching.

As anticipated, achieving the optimal tuning between the optical cavities during the epitaxial process proved to be challenging. This tuning is highly sensitive to variations in layer thicknesses, meaning that calibration errors and growth rate fluctuations can significantly affect the configuration of FP resonances. Regrettably, only one sample with satisfactory tuning was successfully produced. However, we developed a method to adjust the tuning of the EAM-VCSEL during the epitaxial growth process. This involves modifying the growth rate of an effusion cell based on TMM reflectivity simulations to shift the FP resonance wavelength of a cavity, guided by in-situ measurements.

To enhance the effectiveness of this method, we could further refine it by incorporating a reliable model for the AlGaAs complex refractive index at $550°C$. This model, used in conjunction with optimization algorithms (e.g., those available in the scipy library [79]) and the TMM, would enable us to more precisely determine the actual growth rates and the necessary corrections to apply. Note that tuning adjustment could be achieved post epitaxy by using an oxide aperture in the EAM.

Overall, we have made significant improvements to the EAM-VCSEL fabrication process. The next phase involves characterizing the device's performance and comparing it with standard VCSEL performances. It is crucial to assess the quality of electrical contacts using dedicated TLM patterns, perform static electrical characterizations, and conduct high-frequency characterizations to validate the relevance of our design choices.

5 Characterisations

In the preceding chapters, we detailed our approach to enhance the bandwidth of the EAM-VCSEL through design improvements. We put emphasis on the challenges posed by the coupling between the cavities and its impact on high-frequency performance. We highlighted the critical role of the epitaxial growth process in achieving the desired coupling. Additionally, we discussed the optimization of the EAM structure's design to maximize high-frequency absorption modulation.

In this chapter, we present the electrical and optical characteristics of the manufactured EAM-VCSEL. The static and high-frequency operation of the components are fully characterized.

The first section presents the characterisations related to the coupling between the cavities. We see which device shows the best potential from a detuning perspective, and thus for high-frequency operation, then we study the homogeneity of the coupling on the wafer.

The second section presents the static electrical results. After examining the quality of the metal contacts, we investigate the current voltage response of the EAM to deduce the available bias range of the EAM. Then we check whether the VCSEL can be used to inject light into the EAM.

The third section presents the high-frequency operation of the device. After explaining the $67GHz$ setup, we present a method to extract the transfer function of the EAM as a function of the voltage rather than typical VNA's powerwaves. Then we show the result of this method, investigate the EAM high-frequency response, and visualize its bandwidth for several biases.

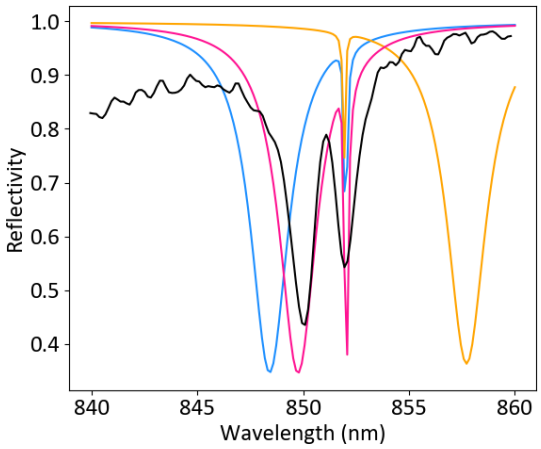

Figure 51: Room temperature post-growth FTIR reflectivity measurement of the grown EAM-VCSEL structure (black). Numerical reflectivity calculation in the case of: strong coupling (magenta), moderate coupling (blue, EAM cavity deviation of $-3nm$), overcoupling (orange, deviation of $+7.5n$m)

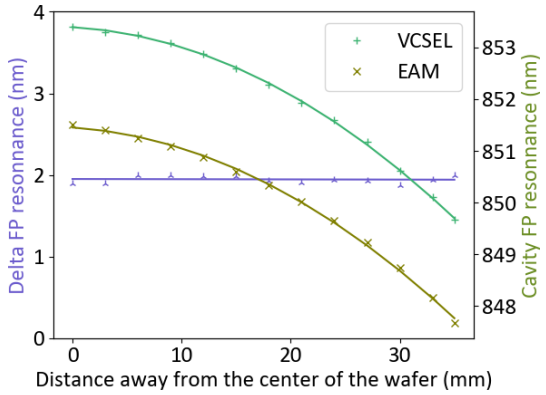

Figure 52: Room temperature post-growth measurements of the cavities FP resonance by FTIR at different locations on the wafer

5.1 Cavities coupling

Since the amount of coupling between the cavities is linked to their relative thicknesses, any growth offset implies that the cavities thicknesses can differ from the designed structure, resulting in a different coupling than expected. Figure 51 shows the reflectivity of the EAM-VCSEL for different couplings. The case for moderate coupling, with the highest difference between the respective EAM and VCSEL FP resonances (cavity deviation of $-3nm$) has been simulated using TMM in blue, while a simulated strong coupling reflectivity is in magenta. The orange reflectivity curve simulates the case of overcoupling where the EAM FP resonance wavelength is redshifted beyond the VCSEL FP resonance (deviation of $+7.5nm$), making absorption modulation inefficient. Unfortunately, the EAM-VCSEL 1 exhibits overcoupling. It is thus unusable. The FTIR measurement of the EAM-VCSEL 2 is depicted on figure 51 in black, with an EAM FP resonance between the case of moderate coupling, and the VCSEL FP resonance. The EAM-VCSEL sample 2 lands in the category of strongly coupled cavities, and, while it is not optimal, shows potential and should be able to achieve absorption modulation.

5.1.1 Coupling variations with wafer location

During epitaxy, the molecular beam emerging from an effusion cell is inherently non-uniform in spatial distribution. The growth rate peaks along the effusion cell's central axis and gradually diminishes as it moves away from this axis. Consequently, on a 4-inch substrate, a minor variation in growth rate exists, characterized by an angular distribution [80] [60].

This implies that the FP resonance wavelength of the cavities, as well as coupling might vary depending on location on the wafer. The FP resonance of each cavity of the EAM-VCSEL 2 sample has been measured with FTIR, as well as the resulting gap (figure 52). The VCSEL has a very good configuration: while the FP resonance wavelength indeed decreases the closer to the edge of the wafer we get, it ranges from 850 to $853nm$. The EAM exhibits the same trend, ranging from 848 to $851nm$. More importantly, the gap between the two FP resonances, and thus the coupling, is actually constant ($2nm$) all over the 4 inch wafer, showing the stability of the growth conditions during the several hours' growth.

This last result means that if the optimal coupling is achieved for a wafer, since the coupling is constant all over the wafer, all the EAM-VCSEL devices that will be processed from this wafer will have the same coupling. Thus, the coupling problematic is not detrimental to the fabrication yield, making our device potentially compatible with production on an industrial scale.

5.2 Static electrical results

5.2.1 Contacts electrical properties

To ensure the best performances, ohmic low resistance electrical contacts are crucial. There are three metal-semiconductor contacts on the EAM:

- The back-face contact (cathode) for the forward biasing of the VCSEL. Since the contact covers the entire backside of the sample, the total resistance of the contact is low because there are multiple paths for current flow in parallel. It is an N-type contact, the substrate is doped with a concentration of $5 \times 10^{18} at.cm^{-3}$.
- The top contact for the reverse biasing of the EAM. This contact is the most critical, is silicon N-type with a doping amount of $5 \times 10^{18} at.cm^{-3}$ with the smallest contact surface.
- The middle contact for the ground plane. It is a carbon P-type contact, with a

doping amount of $5 \times 10^{18} at.cm^{-3}$ and has a slightly larger contact surface than the top contact.

For all these contacts, doping is realised during the epitaxy, then $50nm$ of titanium and $500nm$ of gold are deposited by evaporation. For the N-type contacts, a deposit of $AuGe/Ni$ would provide a better contact [81], however only PVD of $AuGe/Ni$ by sputtering is available for this alloy in the LAAS cleanroom. Since sputtering deposition is diffuse and not directional, considering the size of the top contact pattern (a ring of $20\mu m$ diameter), this process is not compatible with lift-off, as metal can be deposited on the sides of the sacrificial layer, preventing it from lifting off. The N-type Ti/Au contacts could be improved with an annealing of $10mins$ beyond $473K$ [82] in N_2 atmosphere. While the samples did not undergo a dedicated annealing step, during the aluminium oxidation step to create the aperture, the sample is heated at $430°C$ for more than an hour in similar atmosphere conditions, which should contribute to the quality of the contact.

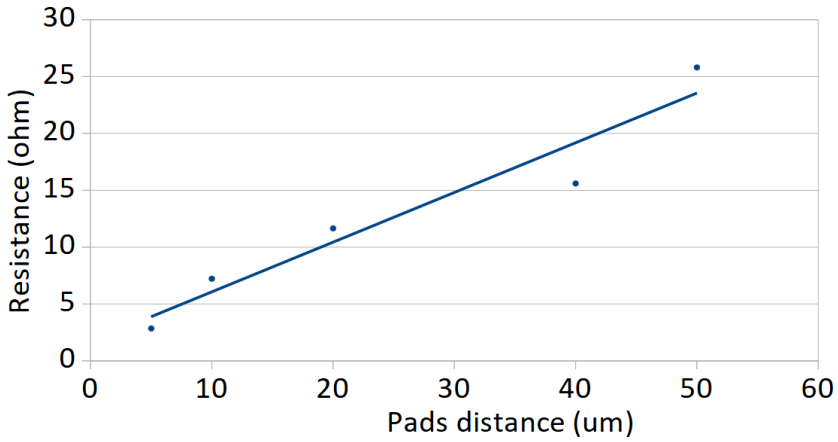

Figure 53: Transfer Length Method (TLM) measurement of the top contact of the EAM.

While the top contact has a decent contact resistance $R_c = 0.85\Omega$, $L_T = 1.94 \times 10^{-4} cm$, $\rho_c = 1.55 \times 10^{-6} \Omega.cm^2$, $Z_{pad} = 94\mu m$, as it can be seen on figure 53, the middle contact exhibits Schottky behavior, with a forward voltage $V_{th} = 3V$. Despite this inconvenience, the effect brought by this defective contact is actually negligible since, as we will see chapter 5.3.4, the strongest photocurrent is achieved with a bias of $\approx 6V$, and the best RF performance are achieved with a bias ranging from $5V$ to $7V$.

For the sake of improving future design and process, we nonetheless investigated the origin of this problem. We carried out a Secondary Ion Mass Spectrometry (SIMS) of the device to measure the variation of aluminium fraction (figure 54 and the concentration of dopants (figure 55) with depth. While the aluminium fraction measured is the one expected, the device is most likely underdoped. Indeed, even though the top contact

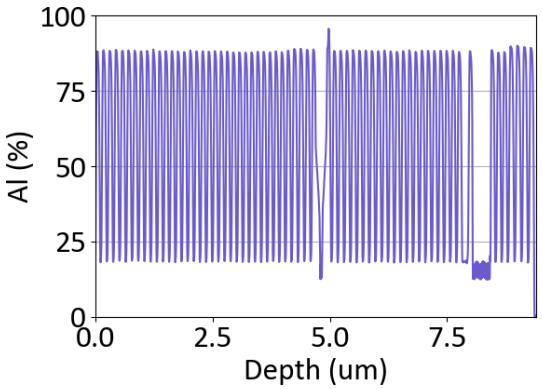

Figure 54: SIMS measurement of the aluminium fraction as a percentage of the $AlGaAs$ alloy along the EAM-VCSEL, with the substrate on the left, the VCSEL in the middle, and the EAM on the right

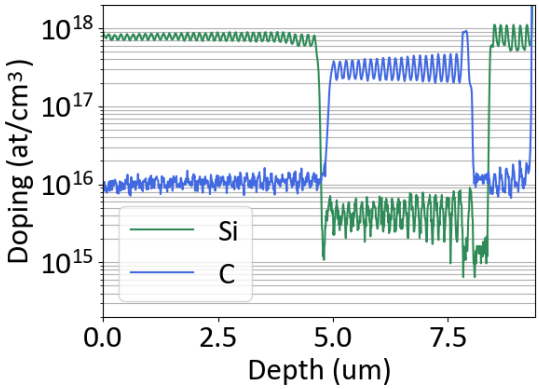

Figure 55: SIMS measurement of the dopant concentration along the EAM-VCSEL, with the substrate on the left, the VCSEL in the middle, and the EAM on the right

has the expected doping of $5 \times 10^{18} at.cm^{-3}$ of silicon, the middle contact barely reaches $1 \times 10^{18} at.cm^{-3}$ of carbon. This could be explained by a lower dopant incorporation in $AlGaAs$ than $GaAs$ on which the doping calibrations were done. In the future, a target of $1 \times 10^{19} at.cm^{-3}$ in the design could be pertinent. Nonetheless, since during the RF characterisation the EAM exhibits the highest bandwidth with a constant bias of $\approx 4.5V$, this defect is not severe.

5.2.2 EAM and VCSEL static current-voltage response

The EAM is a p-i-n junction thus has a diode behavior. Its electro-absorption behavior has similarities with photodiodes behavior. When the photons are absorbed, they create an electron-hole pair (or exciton). In order to sweep them away and spatially separate them, we need to apply an electric field in reverse bias. For an incident optical power P_0, there is an optimal bias voltage at which the highest photocurrent is achieved, however we need to watch out for the avalanche threshold, as once the threshold is exceeded, the EAM is quite likely to be destroyed.

DC current voltage measurements were carried out in order to investigate the different static operating electrical behaviors. Figure 56 present the current-voltage curve of the EAM, and figure 57 its logarithmic counterpart. The typical diode behavior of the EAM is confirmed. In forward mode the threshold voltage is $V_{th} \approx 1.5V$. In reverse bias, we can clearly see an avalanche threshold $V_{avalanche} \approx -22V$. This provides us quite a large zone to investigate the optimal bias in reverse to achieve the highest photocurrent and thus the highest sensitivity to voltage fluctuations to modulate the

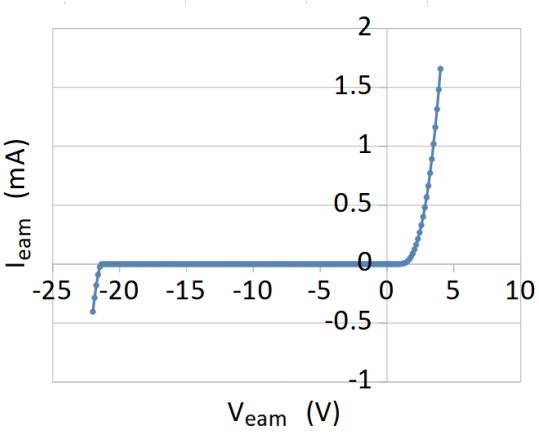

Figure 56: Current-voltage curve of the EAM.

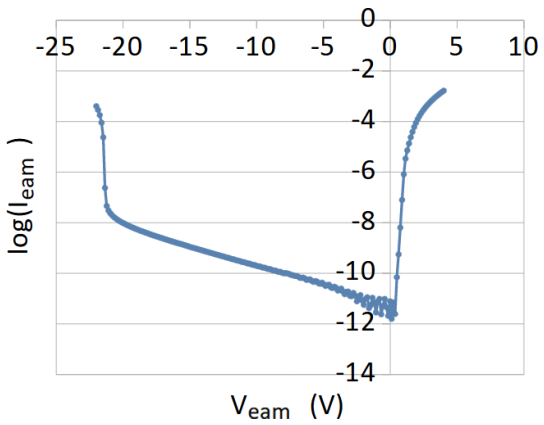

Figure 57: Logarithm of the current-voltage curve of the EAM.

absorption.

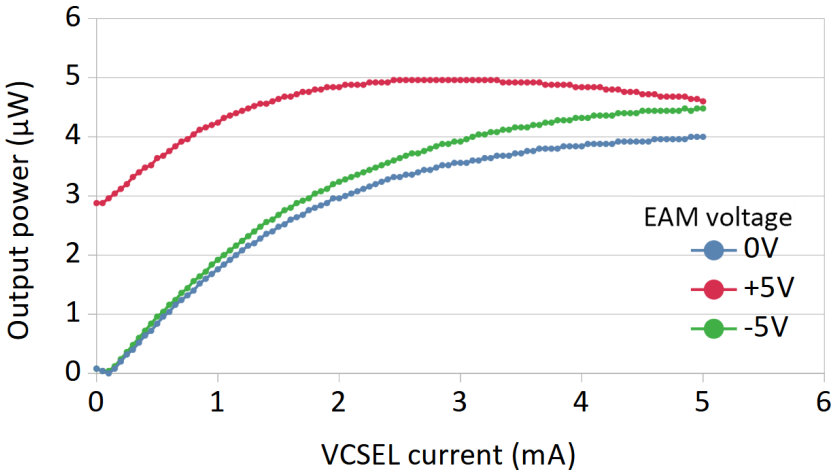

Figure 58: L-I curve of the EAM-VCSEL structure for several EAM biases.

Another important characterisation to carry out is the measurement of the emitted optical power of the VCSEL as a function of its injection current (or L-I curve). Since biasing the EAM shifts the absorption peak, and modify the coupling between the two cavities, the voltage of the EAM needs to be taken into account for such a measurement.

L-I curve of the EAM-VCSEL structure for several EAM biases is depicted in figure 58, and unfortunately shows that the VCSEL is unable to achieve lasing, and emits light only by electroluminescence. A possible explanation is that since the coupling between the cavities is strong, the light emitted by the VCSEL is partially reflected back into the cavity and perturbs the carrier density, preventing the VCSEL from achieving population inversion. Reverse biasing the EAM doesn't do much, however, forward bias increase the light emission. Since the absorption peak of the EAM redshifts when

reverse biased, forward biasing might reduce the absorption and decrease the coupling between the cavities, which ease the light emission.

Many EAMs on the sample exhibited a short electrical characteristic rather than the expected diode behavior. This issue can be attributed to a problem during the SiO_x passivation of the VCSEL mesa, resulting in a SiO_x deposition of $900nm$ instead of the intended $400nm$. Consequently, the ground contact was positioned closer to the RF microstrip access. This, combined with the variations in mesa heights reported in Chapter 4.2.3, and potential disparities in the planarization of the BCB, likely contributed to the occurrence of these shorts.

The inability of the VCSEL to achieve lasing implies that we cannot utilize it to inject laser light into the EAM for RF characterizations. Consequently, we must rely on an external tunable laser and an optical fiber positioned vertically to couple the external laser beam onto the top of the mesa.

5.3 High-frequency operation

5.3.1 Experimental setup

In the experimental setup, the focus is on characterising the Electro-Absorption Modulator (EAM). Due to the strong coupling, preventing the VCSEL from achieving lasing, a short circuit is applied to the VCSEL, allowing the sole EAM to be effectively characterised.

Figure 59 depicts the electro-optic characterization setup for the EAM. On the electric side, a Vector Network Analyzer (VNA Agilent PNA-X) is used to generate the RF power wave, while a Power Supply Unit (PSU) provides a constant reverse bias on the EAM. These two signals are combined using a bias tee, followed by a StabilityPlus $67GHz$ 50Ω cable. The cable is subsequently connected to CascadeMicrotech Z67-XVF-GSG-150 RF probes, positioned down on the micro-strip EAM access.

On the optical side a tunable semiconductor light source Superlum Broad Sweeper 840-1 capable of emitting coherent single-mode beam between 820 and $870nm$ is employed, to inject light into the EAM. The laser is connected to a single-mode polarisation-maintaining FC/APC $1m$-long optical fiber, which in turn is connected to a 50-50 coupler. The resulting signal is then transmitted through another optical fiber mounted on a micropositioner carefully aligned perpendicular to the EAM. To capture the optical response, a photodiode (Newfocus 1014 $45GHz$ $0.25A/W$) is connected to the other end of the 50-50 coupler. This converted electrical photocurrent is then directed to the second port of the VNA.

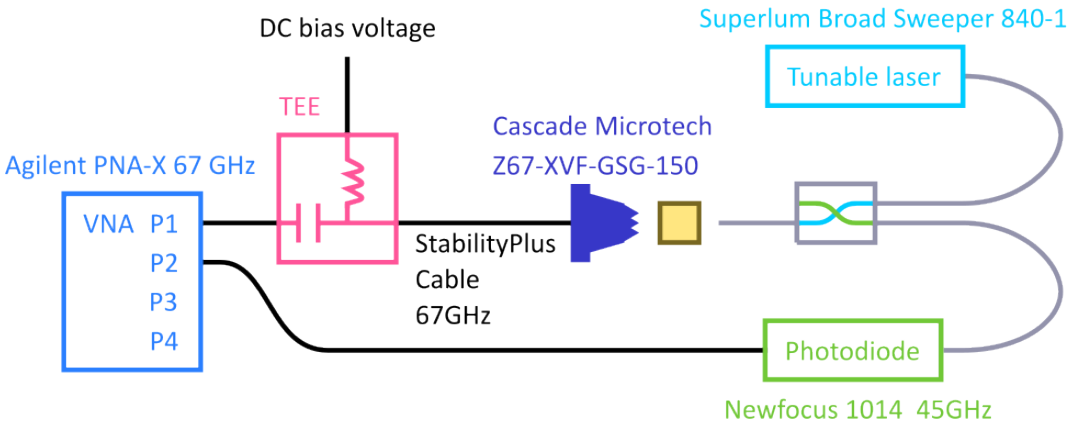

Figure 59: Diagram of the electro-optic characterization of the EAM with a VNA and external laser injection.

5.3.2 Optical path verification

In our characterisation of the modulator, we employ an external laser followed by an optical fiber and a 50-50 optic coupler to introduce light into the system, which is then measured back after reflection from the EAM. It is important to note that losses occur along the optical path : at the butt-coupling with the fiber on top of the EAM, and due to reflected signal and the mismatch between the numerical apertures and effective areas of the cleaved fiber facet and the EAM. The different interfaces also introduce coupling losses. Therefore, we intend to meticulously measure the optical power at each juncture within the optical section of our setup to accurately assess and account for these losses.

The laser is generated at $4mW$. It then travels in an optical fiber, then the 50-50 coupler which decreases the optical output power to $1.52mW$. After being reflected, and travelling through the coupler once again, the laser reaches an optical power of $223\mu W$. After travelling through the last optical fiber section, the laser power goes down to $220\mu W$ before reaching the photodiode.

5.3.3 RF setup calibration

Calibrating high-frequency measurement instruments, including network analyzers, before each measurement is mandatory to ensure accurate results. High-frequency measurements are susceptible to various factors that can introduce errors, such as systematic errors, environmental effects, and component drift. By calibrating the instrument before each measurement, any potential deviations or inaccuracies are corrected, ensuring the validity of the measurement data obtained from the network analyzer in the studied frequency range.

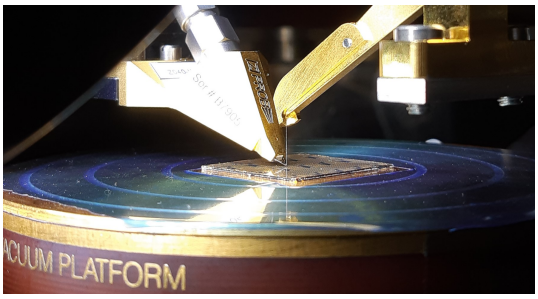

(a) Overview with the sample on the chuck.

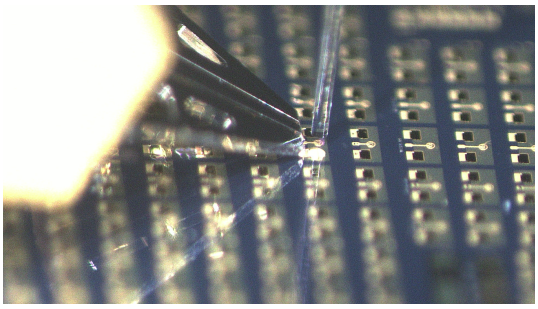

(b) Zoom on the optical fiber.

Figure 60: RF probe and vertically aligned optical fiber on the EAM-VCSEL.

The network analyzer undergoes a power calibration with a power meter Agilent N1913A and an average power sensor Agilent N8488A ($10MHz - 67GHz$) ($-35dBm$ to $20dBm$) plugged to the port 1 in order to make sure that the signal generated by the VNA is $0dBm$ for every frequency.

Now if we put down the probes on the EAM and measure S-parameters, these parameters would actually represent the ensemble of the straight cable, the RF probes, and the EAM. In order to remove the contribution of the cables and probes from the device S-parameters measurement, an open short load calibration is carried out at the end of the cable with a Data-based Maury kit, then at the end of the probes with a calibration kit FormFactor 101-190D, and the data-based VNA algorithm.

5.3.4 Optical fiber alignment

In order to inject light into the EAM, we use an optical fiber which is cleaved at the end to expose its core, allowing for light transmission as seen in figure 60. We need to align this fiber with the EAM while being perpendicular However, achieving precise alignment solely based on visual inspection through a microscope is difficult.

In order to find the optimal fiber position, the laser is enabled to emit light, and a DC voltage is applied to reverse-bias the EAM (around $6V$ to achieve the highest current). Since the EAM is a p-i-n diode, by biasing it in reverse, the amount of photons absorbed increases, leading to a higher current. Therefore, a higher current reading indicates better alignment between the optical fiber and the EAM. To determine the optimal alignment position, the optical fiber is gradually and meticulously scanned along the x, y, and z axes while monitoring the photo-current. Once the peak current is achieved (around $300\mu A$ or $0.66mW$ in our case), the best alignment between the optical fiber and the EAM is obtained.

5.3.5 Optimal injected laser wavelength

While the EAM is supposed to be optimal to modulate a laser with a wavelength of $850nm$ as designed, with the slight deviations of layers dimensions and composition induced by the epitaxy, the actual optimal wavelength at which the EAM has the highest contrast ratio is probably not exactly at $850nm$. To investigate the optimal injected laser wavelength, we inject light into the EAM by setting up the Broadsweeper laser into a sweep mode, from 848 to $855nm$ as depicted in figure 61, while the EAM is biased at the same voltage than earlier in order to achieve the highest photocurrent possible. Then the EAM photocurrent is measured by a Keysight oscilloscope set up with a Teledyne PA-6-60 transimpedance amplifier.

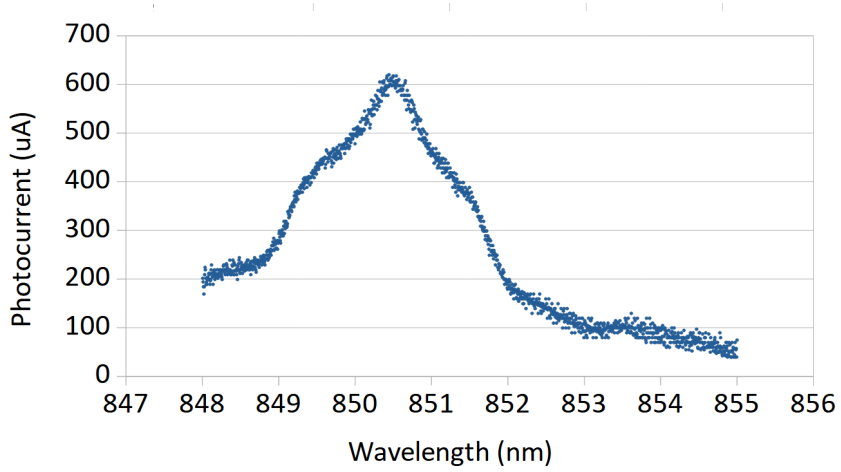

Figure 61: Photocurrent of the EAM as a function of the wavelength of the injected laser.

The highest value of photocurrent ($620\mu A$) is achieved at $850.45nm$, which is actually quite close to the targeted $850nm$ wavelength. For the following high-frequency characterisations, the laser wavelength will be indeed fixed at $850.45nm$.

5.3.6 EAM-VCSEL RF characterisation context

When we characterise a quadripole whose impedance is matched with its access, the power applied on the quadripole Device Under Test (DUT), and the corresponding bias voltage are known and constant, as the input impedance is set to 50Ω. In our setup for the EAM-VCSEL characterisation, the power delivered to the DUT is indeed calibrated to be constant at every frequency when the load impedance is 50Ω. Once connected to the EAM, the applied power, and thus the voltage, is not constant anymore, since the EAM is not 50Ω and its impedance depends on the frequency.

First of all, in order to characterize the EAM, we need to make sure to remove the contribution of the RF probes to the measurement, and thus, move the reference plane to the end of the probe tips. This implies the extraction of the S-parameters of the RF probes. Moreover, since the absorption is correlated to the voltage rather than power, we need to extract the transfer function of the EAM as a function of its small-signal voltage V_{eam}.

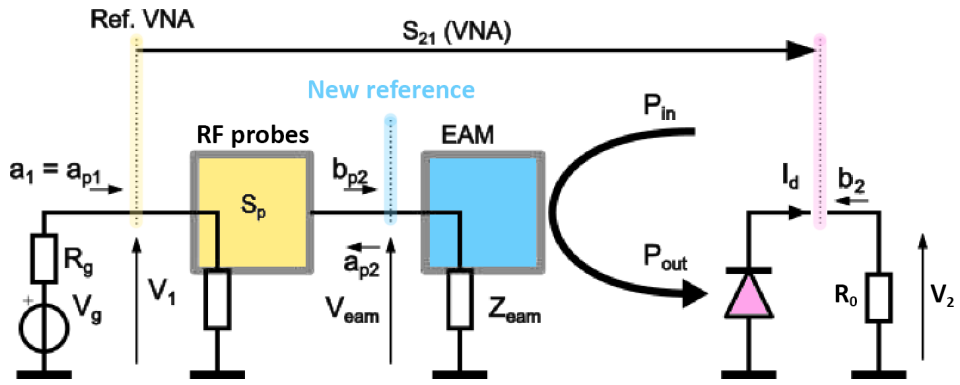

Figure 62: Diagram of the electro-optic characterization of the EAM with indication of the incident and reflected voltage waves.

The electro-optic transfer function of the EAM (figure 62) is:

$$P_{out} = f(P_{in}, V_{eam}) = \alpha V_{eam} \tag{42}$$

The current of the photodiode is:

$$I_d = f(P_{out}) = \beta P_{out} \tag{43}$$

The VNA's port 1 is connected to the EAM following: Port 1 → cable → RF probe → EAM. On the other side, the VNA's port 2 is directly connected to the photodiode's 50Ω output.

5.3.7 Extraction of the RF probe S-parameters

As explained earlier, for the sake of a proper characterisation of the EAM, we need to move the reference plane to the output of the probes, which means measuring their S-parameters. Obviously, since they are probes, we can't simply connect them to Port 1 and 2, but can only connect them to Port 1.

Hence, we require a method for reconstructing the scattering matrix of a multiport network using a series of one-port measurements [83]. This method involves the use of

auxiliary circuits, including open-circuit, short-circuit, and a 50Ω load, to solve the S-matrix of a two-port network. Subsequently, the S-parameters of the two-port network are calculated using the port reduction method. The S-parameters refer to:

- S_{11}: the input reflection coefficient at port 1
- S_{21}: the forward transmission coefficient from port 1 to port 2
- S_{12}: the reverse transmission coefficient from port 2 to port 1
- S_{22}: the output reflection coefficient at port 2

The reflection coefficient at port 1 of a two-port Device Under Test (DUT), when its port 2 is terminated with the load reflection coefficient Γ_a, is expressed as follows:

$$S_{11}^a = S_{11} + \frac{S_{12}S_{21}\Gamma_a}{1 - S_{22}\Gamma_a} \tag{44}$$

Or:

$$S_{11} + S_{11}^a\Gamma_a S_{22} + \Gamma_a(S_{12}S_{21} - S_{11}S_{22}) = S_{11}^a \tag{45}$$

Here S_{11}^a is the measured reflection coefficient, and S_{11}, S_{22}, $S_{12}S_{21} - S_{11}S_{22}$ are the unknown S-parameters of the DUT. Assuming the DUT is reciprocal ($S_{12} = S_{21}$) three unknowns have to be retrieved. This is done using three different Γ terminations, which results in the following matrix equation:

$$\begin{pmatrix} 1 & S_{11}^{open}\Gamma_{open} & \Gamma_{open} \\ 1 & S_{11}^{short}\Gamma_{short} & \Gamma_{short} \\ 1 & S_{11}^{load}\Gamma_{load} & \Gamma_{load} \end{pmatrix} \begin{pmatrix} \\ S_{11} \\ S_{22} \\ S_{12}S_{21} - S_{11}S_{22} \end{pmatrix} = \begin{pmatrix} S_{11}^{open} \\ S_{11}^{short} \\ S_{11}^{load} \end{pmatrix} \tag{46}$$

This system is a classic $Ax = b$ linear matrix equation, and can be solved using standard algorithmic methods such as 'numpy.linalg.solve' [84].

Once we measure the reflection coefficient for each known termination, we can then calculate the S-parameters of the RF probes, and proceed to the next step.

5.3.8 EAM transfer function extraction

The EAM absorption is driven by the applied voltage V_{EAM} rather than power. We need to extract the voltage transfer function of the EAM H_{EAM} from the available data measured with the VNA. From figure 62 follows:

$$b_{p2} = S_{p21}a_{p1} + S_{p22}a_{p2} \tag{47}$$

$$a_{p2} = \Gamma_{eam} b_{p2} \tag{48}$$

Thus:

$$b_{p2} = \frac{S_{p21}}{1 - S_{p22}\Gamma_{eam}} a_{p1} \tag{49}$$

or:

$$a_1 = a_{p1} = b_{p2} \frac{1 - S_{p22}\Gamma_{eam}}{S_{p21}} \tag{50}$$

We can then re-write b_{p2} as a function of V_{eam}:

$$b_{p2} = \frac{V_{eam} + R_0 I_{eam}}{2\sqrt{R_0}} = \frac{V_{eam}}{2\sqrt{R_0}}(1 + \frac{R_0}{Z_{eam}}) \tag{51}$$

Lets write a_1 without being a function of b_{p2}:

$$a_1 = \frac{V_{eam}}{2\sqrt{R_0}}(1 + \frac{R_0}{Z_{eam}}) \frac{1 - S_{p22}\Gamma_{eam}}{S_{p21}} \tag{52}$$

From figure 62 it follows:

$$b_2 = \frac{V_2 + R_0 I_2}{2\sqrt{R_0}} = \frac{V_2}{\sqrt{R_0}} \tag{53}$$

Let's deduce S_{21} from a_1's and b_2's respective expression as a function of V_2 and V_{eam}:

$$S_{21} = \frac{b_2}{a_1} = \frac{\frac{V_2}{\sqrt{R_0}}}{\frac{V_{eam}}{2\sqrt{R_0}}(1 + \frac{R_0}{Z_{eam}}) \frac{1 - S_{p22}\Gamma_{eam}}{S_{p21}}} \tag{54}$$

Finally, we can obtain the EAM's voltage gain H_{eam} with:

$$H_{eam} = \frac{V_2}{V_{eam}} = \frac{S_{21}}{2}(1 + \frac{R_0}{Z_{eam}}) \frac{1 - S_{p22}\Gamma_{eam}}{S_{p21}} \tag{55}$$

5.3.9 EAM high-frequency characterisation

High-frequency characterisation of the EAM have been carried out with the previously described setup. While the power transfer function S_{21} was directly measured by the VNA, the voltage transfer function H_{eam} has been calculated using the S_{21} measurement with equation 55, and the probes' S parameters using equation 46. Figure 63 shows a comparison, with a reverse bias of $7V$, of the two normalized transfer functions

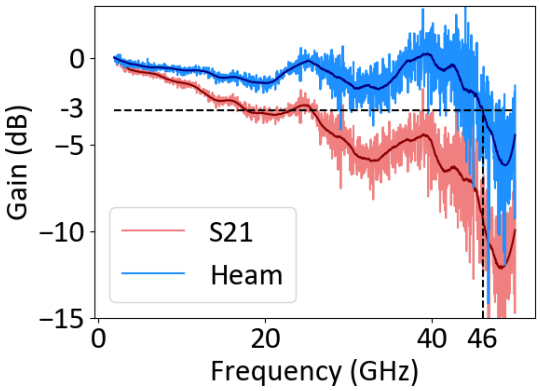

Figure 63: Comparison of S_{21} and the corrected voltage transfer function of the EAM with a bias of 7V.

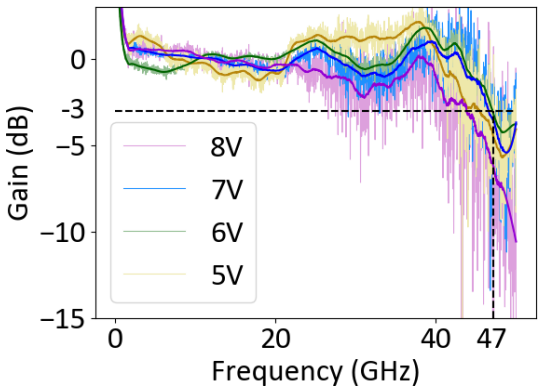

Figure 64: Voltage transfer function of the EAM, at different biases.

of the same EAM. The difference between both transfer functions illustrates the necessity to take into account the impedance mismatch. At $7V$, the EAM response is rather flat and shows low noise until $\approx 25GHz$, and drops significantly after $\approx 42GHz$, which corresponds to the photodiode bandwidth limit. Therefore, the characterisation could be further improved, by a rigorous characterization of the photodiode, and normalizing S_{21} according to its response.

Measurement of the voltage transfer function H_{eam} has been carried out for several DC voltage biases. Figure 64 presents H_{eam} at biases ranging from $5V$ to $8V$ including the smoothen response using a Savitzky–Golay filter. Below $5V$ and above $8V$, responses were very noisy, and close to the noise floor. The best bandwidth is obtained with a bias of $6V$ as it can be seen in figure 65. The response shows very low noise, and is rather flat until $35GHz$, then drops as expected above $42GHz$. When the measurement is normalized to $0dB$ using the average value in the flat range ($1GHz$ - $20GHz$), the voltage transfer function reaches the $-3dB$ at $47GHz$. In comparison with the best results previously achieved with this kind of structure [36], we can consider that we increased the bandwidth by $18GHz$.

While the voltage transfer functions exhibit a trend similar to that of a low-pass curve, featuring a relatively flat response within the bandwidth followed by a negative slope, they also manifest irregularities in the form of several minor dips and peaks, each on the order of magnitude of a decibel. Moreover, as shown in Figure 64, these irregularities vary depending on the constant bias value. Given the reproducibility of these irregularities, it is likely that they are correlated with specific physical parameters of the EAM-VCSEL. Understanding their origin is crucial for achieving bandwidth flattening. This would require a more comprehensive simulation of the electrical behavior of the EAM-VCSEL. One possible approach is to employ an analytical simulation, focusing on photon and charge carrier dynamics, as exemplified by the model presented

by V. Torrelli et al. [85]. However, such modeling may not encompass various electrical phenomena, such as parasitic capacitances, doping effects, metal-semiconductor junctions, and quantum wells behavior. Another option to consider these phenomena is finite-element method simulation, using tools like nextnano [86]. Nevertheless, it should be noted that due to the complexity of the EAM-VCSEL, achieving convergence in numerical solutions of discrete methods tends to be challenging.

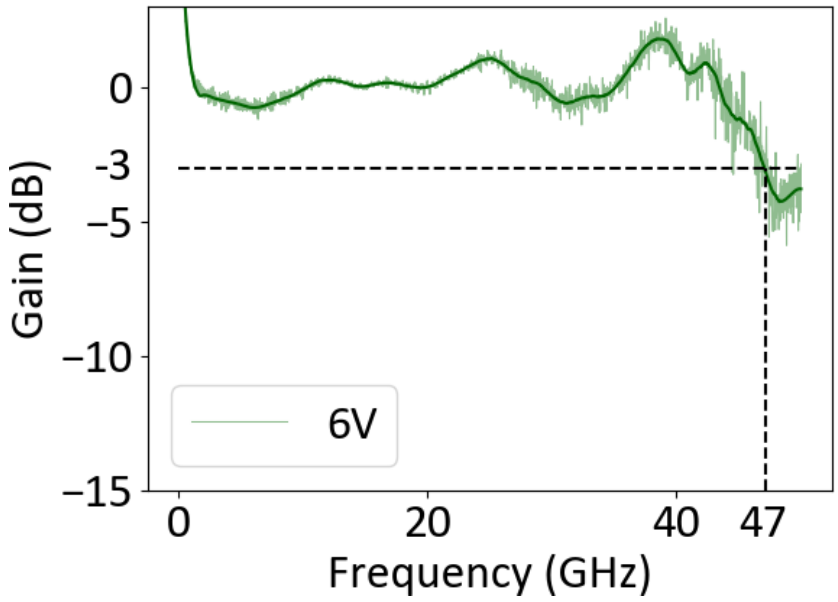

Figure 65: Voltage transfer function of the EAM with a bias of 6V.

Regarding the measurement setup, there is still room for improvement. Firstly, the laser injection can be enhanced by securing the optical fiber more effectively. The photocurrent is exceptionally sensitive to the position of the cleaved edge of the optical fiber. Even minor adjustments to the fiber using the micro-positioners on the fiber holder have a significant impact on the measured response. Given that the distance between the fiber grip and the cleaved edge is approximately $1cm$, we suspect that micro air currents or variations in air conditioning could negatively affect measurement accuracy. This issue could be mitigated by using a firmer and shorter grip for the optical fiber.

Another factor that degrades the measurement accuracy is the 50-50 coupler. This component allows the generated laser light to travel to the EAM and its reflection to reach the photodiode. However, it splits the incoming optical signal into two equal parts, each carrying at most 50% of the input power. Consequently, the total losses introduced by this component exceed $6dB$. To enhance the setup for EAM characterisation, replacing the 50-50 coupler with a 3-port optical circulator is advisable. Ideally, an EAM-VCSEL with a properly functioning VCSEL wouldn't even require external laser injection, a coupler, or a circulator.

As mentioned earlier, the photodiode has a specified bandwidth of $3dB$ at $45GHz$. Given that the EAM's bandwidth extends up to $47GHz$, it's evident that the photodiode is limiting the EAM's bandwidth. One approach to obtain a more accurate estimation of the EAM's bandwidth is to characterise the frequency response of the photodiode and then use it for normalising the EAM measurements. However, it is worth noting that this approach may lead to increased noise at frequencies beyond the photodiode's bandwidth.

5.4 Conclusion

In this chapter we measured the different characteristics of the EAM we realised according to our design methods, and fabrication processes. Static electrical measurements such as i-v curve, and TLM have been carried out, as well as FTIR reflectivity, SIMS, and VNA S-parameters measurements.

On the downside, the coupling between the cavities of the best sample remained strong and constant across different wafer locations. The integrated VCSEL was unable to achieve lasing emission and emitted solely through electroluminescence, likely due to its strong coupling with the EAM cavity. Additionally, the metal middle contact exhibited Schottky behavior owing to insufficient doping. While the coupling could potentially be improved through better epitaxy calibration, enhancing the contact quality would require an increase in doping concentration to at least $1 \times 10^{19} at.cm^{-3}$.

On the bright side, the EAM exhibited excellent high-frequency performance with a bandwidth of $47GHz$, surpassing the previous highest recorded performance for an EAM-VCSEL ($29GHz$). However, there is still room for improvement in the high-frequency characterization. Since the EAM bandwidth is limited by the photodiode's $45GHz$ bandwidth, considering the photodiode response could lead to a more accurate characterization of the EAM. Furthermore, laser injection could be enhanced through minor modifications of the optical setup.

The characteristics of our device have demonstrated performance levels that are very close to the latest VCSEL developments, which boast bandwidths ranging from 40 to $70GHz$. These results are particularly encouraging, given the potential for further enhancements through various improvement strategies. A more comprehensive comparison with competitor solutions could be conducted, but it would necessitate characterizations involving encoding methods such as PAM-4 or QAM-OFDM. With these methods, we could assess spectral efficiency or generate open-eye diagrams, and we would not be restricted by the $45GHz$ bandwidth of the photodiode.

Nonetheless, as we continue to address challenges such as optimizing cavity coupling, improving the metal middle contact, and refining the optical setup, the EAM-VCSEL

configuration holds significant promise for achieving even higher bandwidths in the future. With its current performance already in line with the latest advancements and room for improvement, the EAM-VCSEL showcases its potential as a key player in expanding the capabilities of high-frequency optical communication and related applications.

6 Conclusion and perspectives

The need for faster data access is fueling the growth of massive data centers and delivery infrastructure. Internet traffic has significantly increased from 1995 to 2020, and this demand continues to rise due to factors such as 4K TV, video conferencing, remote work, and gaming. Internet usage is on the upswing, requiring infrastructure to keep pace.

To address the need for increased data rates, data centers and HPC (High-Performance Computing) have widely adopted VCSELs. However, VCSELs are limited to a bandwidth of approximately $35GHz$ due to charge carrier dynamics. As a result, research has explored various approaches, including combining VCSELs with complex encoding formats and driving circuitry or exploring alternative technologies.

To boost bandwidth, one approach entails separating the functions of light emission and light modulation within the VCSEL by employing Electro-Absorption Modulators (EAMs). Here, we present a structure that integrates both functions into a single device known as the EAM-VCSEL. This device offers the advantage of practical integration into a system, akin to a conventional VCSEL, while boasting a theoretical EAM bandwidth exceeding $100GHz$.

The approach of this thesis involved beginning with an existing design that had achieved a bandwidth of $30GHz$ achieved during the previous L. Marigo-Lombart's thesis on this topic at LAAS-CNRS. This design was enhanced through analytical simulations aimed at modeling the optical and electrical behavior of the EAM-VCSEL. The EAM multiple quantum wells (MQWs) were redesigned to improve charge carrier dynamics and maximize absorption modulation depth. Additionally, addressing the issue of coupling between the optical cavities of the EAM and the VCSEL was a key focus in the design phase, aimed at optimizing potential performance. In the end, three distinct structural designs were explored.

The fabrication process was then reviewed and enhanced. Epitaxy was performed with in-situ measurements of wafer reflectivity and relative curvature. This, combined with precise calibration of the effusion cells, resulted in the growth of structures with Fabry-Pérot resonances in the cavities much closer to the targeted wavelength of $850nm$ compared to previous batches. In-situ monitoring of VCSEL oxidation was successfully verified by examining the oxide aperture using FIB etching. Additionally, several fabrication steps were improved, including mesa passivation, BCB packaging, and plasma etching.

Finally, the method for RF characterizations has been significantly enhanced. Several improvement have been brought to the setup, including the use of a high-bandwidth $850nm$ photodiode, improved fiber alignment, and a $67GHz$ microwave analysis setup.

The influence of the RF probes was entirely de-embedded, and the voltage transfer function was extracted to better represent the high-impedance capabilities of the EAM.

Nevertheless, we must acknowledge the limitations encountered during this thesis work. Achieving ideal coupling during epitaxial growth proved challenging due to uncertainties in the growth rate calibration of the effusion cells and growth rate drift. To enhance the reproducibility of ideal coupling during epitaxy, it may be beneficial to develop a refractive index model for $AlGaAs$ at epitaxy temperature. This model could be used in conjunction with in-situ reflectivity monitoring to refine the calibration of the effusion cells during the epitaxial process.

Plasma etching of the mesas presented challenges. The etching depth was uneven across the sample surface, resulting in excessive etching along the sample edges. Consequently, several structures were over-etched, reducing the yield. Moreover, considering the etching rate, the middle contact layer was too thin, making the timing of plasma etching precarious, and exacerbating the uneven etching. To address this issue, it may be necessary to explore and optimize the etching conditions and consider increasing the thickness of the middle contact layer.

Although the RF characterization setup has seen enhancements, further improvements can be made. Given the photodiode's bandwidth of $45GHz$, measurements should be normalized, taking into account the photodiode's response. It would be beneficial to replace the coupler with a circulator and ensure a secure grip on the optical fiber for laser injection. Ideally, additional measurements involving more complex encoding formats, such as PAM-2 or open-eye diagram measurements, should be conducted to provide a more comprehensive comparison of EAM-VCSEL performance with current alternative technologies.

To optimize the EAM-VCSEL design and develop a deeper understanding of RF characterizations, it is advisable to conduct more complex simulations. Specifically, exploring various multiple quantum well (MQW) designs, such as coupled quantum wells, and simulating the EAM impedance would be beneficial.

Nevertheless, the EAM-VCSEL exhibits promising results. With a bandwidth of $47GHz$, it competes favorably with other technologies. Its inherent integration of light emission and optical absorption for data transmission makes it easy to implement, especially in areas where VCSELs are already established. Furthermore, the insights provided in this thesis suggest that it has significant untapped potential for further improvement and enhanced performance.

7 Bibliography

[1] Cisco. *Cisco Annual Internet Report (2018–2023) White Paper*. https://www.cisco.com/c/en/us/solutions/collateral/executive-perspectives/annual-internet-report/white-paper-c11-741490.html. 2018.

[2] Jim Tatum. "VCSEL Fundamentals". In: *VCSEL Industry*. John Wiley & Sons, Ltd, 2021. Chap. 4, pp. 73–104. ISBN: 9781119782223. DOI: https://doi.org/10.1002/9781119782223.ch2.

[3] Yole Développement. *OPTICAL TRANSCEIVERS FOR DATACOM & TELECOM MARKET 2021*. https://medias.yolegroup.com/uploads/2021/07/YINTR21176-Optical-Transceivers-for-Datacom-Telecom-Market-2021_Flyer.pdf. 2021.

[4] Michael Larabel. *AMD-Powered Frontier Supercomputer Tops Top500 At 1.1 Exaflops, Tops Green500 Too*. https://web.archive.org/web/20220606064113/https://www.phoronix.com/scan.php?page=news_item&px=Top500-Green500-Frontier. Accessed: 2023-02. 2022.

[5] Daniel M. Kuchta. "High Capacity VCSEL-based links". In: *Optical Fiber Communication Conference*. Optica Publishing Group, 2017, Tu3C.4. DOI: 10.1364/OFC.2017.Tu3C.4.

[6] Chih-Hsien Cheng et al. "Review of VCSELs for Complex Data-Format Transmission Beyond 100-Gbit/s". In: *IEEE Photonics Journal* 13.5 (2021), pp. 1–13. DOI: 10.1109/JPHOT.2021.3104647.

[7] Petter Westbergh et al. "Large aperture 850 nm VCSELs operating at bit rates up to 25 Gbit/s". In: *Electronics Letters* 44 (2008), pp. 907–908.

[8] Sergey Blokhin et al. "Oxide-confined 850 nm VCSELs operating at bit rates up to 40 Gbit/s". In: *Electronics Letters* 45 (June 2009), pp. 501–503. DOI: 10.1049/el.2009.0552.

[9] P. Moser et al. "81 fJ/bit energy-to-data ratio of 850 nm vertical-cavity surface-emitting lasers for optical interconnects". In: *Applied Physics Letters* 98.23 (2011), p. 231106. DOI: 10.1063/1.3597799.

[10] P. Westbergh et al. "High-speed 850 nm VCSELs with 28 GHz modulation bandwidth operating error-free up to 44 Gbit/s". In: *Electronics Letters* 48 (Aug. 2012), pp. 1145–1147. DOI: 10.1049/el.2012.2525.

[11] Petter Westbergh et al. "High-Speed Oxide Confined 850-nm VCSELs Operating Error-Free at 40 Gb/s up to 85°C". In: *IEEE Photonics Technology Letters* 25.8 (2013), pp. 768–771. DOI: 10.1109/LPT.2013.2250946.

[12] Lukasz Chorchos et al. “Energy Efficient 850 nm VCSEL Based Optical Transmitter and Receiver Link Capable of 80 Gbit/s NRZ Multi-Mode Fiber Data Transmission”. In: *J. Lightwave Technol.* 38.7 (Apr. 2020), pp. 1747–1752.

[13] Krzysztof Szczerba et al. “30 Gbps 4-PAM transmission over 200 m of MMF using an 850 nm VCSEL”. In: *Opt. Express* 19.26 (Dec. 2011), B203–B208. DOI: 10.1364/OE.19.00B203.

[14] Tianjian Zuo et al. “Single-lane 200-Gbps PAM-4 transmission for Datacenter Intra-Connections employing 850-nm VCSEL”. In: *Asia Communications and Photonics Conference/International Conference on Information Photonics and Optical Communications 2020 (ACP/IPOC)*. Optica Publishing Group, 2020, S3H.2. DOI: 10.1364/ACPC.2020.S3H.2.

[15] Wei-Chi Lo et al. “Effect of Chirped Dispersion and Modal Partition Noise on Multimode VCSEL Encoded With NRZ-OOK and PAM-4 Formats”. In: *IEEE Journal of Selected Topics in Quantum Electronics* 28.1: Semiconductor Lasers (2022), pp. 1–9. DOI: 10.1109/JSTQE.2021.3086056.

[16] Businesswire. *Seoul Viosys Begins Mass Production of 25Gbps VCSELs for 5G Communication Applications*. https://www.businesswire.com/news/home/20210128005444/en/Seoul-Viosys-Begins-Mass-Production-of-25Gbps-VCSELs-for-5G-Communication-Applications. 2021.

[17] Nikolay N. Ledentsov et al. “Serial data transmission at 224 Gbit/s applying directly modulated 850 and 910 nm VCSELs”. In: *Electronics Letters* (2021).

[18] Nasibeh Haghighi et al. “35 GHz Bandwidth with Directly Current Modulated 980 nm Oxide Aperture Single Cavity VCSELs”. In: *2018 IEEE International Semiconductor Laser Conference (ISLC)*. 2018, pp. 1–2. DOI: 10.1109/ISLC.2018.8516258.

[19] Krassimir Panajotov and Richard Schatz. “Coupled-Cavity VCSEL with an Integrated Electro-Absorption Modulator: Small- and Large-Signal Modulation Analysis”. In: *Applied Sciences* 10.17 (2020). ISSN: 2076-3417. DOI: 10.3390/app10176128.

[20] Ross M. Audet et al. “Surface-Normal Ge/SiGe Asymmetric Fabry–Perot Optical Modulators Fabricated on Silicon Substrates”. In: *Journal of Lightwave Technology* 31.24 (2013), pp. 3995–4003. DOI: 10.1109/JLT.2013.2279174.

[21] Patrick Iannone et al. “PAM-4 transmission up to 160Gb/s with surface-normal electro-absorption modulators”. In: *Opt. Lett.* 45.16 (Aug. 2020), pp. 4484–4487. DOI: 10.1364/OL.399280.

[22] Stefano Grillanda et al. “107 Gb/s Ultra-High Speed, Surface-Normal Electroabsorption Modulator Devices”. In: *Journal of Lightwave Technology* 38.4 (2020), pp. 804–810. DOI: 10.1109/JLT.2019.2951290.

[23] P. Pellandini et al. “Dual-wavelength laser emission from a coupled semiconductor microcavity”. In: *Applied Physics Letters* 71.7 (Aug. 1997), pp. 864–866. ISSN: 0003-6951. DOI: 10.1063/1.119671.

[24] J. van Eisden et al. “Modulation properties of VCSEL with intracavity modulator”. In: *Vertical-Cavity Surface-Emitting Lasers XI*. Ed. by Kent D. Choquette and James K. Guenter. Vol. 6484. International Society for Optics and Photonics. SPIE, 2007, 64840A. DOI: 10.1117/12.701516.

[25] Hamed Dalir et al. “Compact electro-absorption modulator integrated with vertical-cavity surface-emitting laser for highly efficient millimeter-wave modulation”. In: *Applied Physics Letters* 105.8 (Aug. 2014). 081113. ISSN: 0003-6951. DOI: 10.1063/1.4894716.

[26] L Marigo-Lombart et al. “Vertical electro-absorption modulator design and its integration in a VCSEL”. In: *Journal of Physics D: Applied Physics* 51.14 (Mar. 2018), p. 145101. DOI: 10.1088/1361-6463/aab1dc. URL: https://dx.doi.org/10.1088/1361-6463/aab1dc.

[27] Naci Balkan and Ayşe Erol. *Semiconductors for Optoelectronics*. Springer, 2021.

[28] Jim Tatum. “VCSEL Fundamentals”. In: *VCSEL Industry*. John Wiley & Sons, Ltd, 2021. Chap. 2, pp. 29–45. ISBN: 9781119782223. DOI: https://doi.org/10.1002/9781119782223.ch2.

[29] T. Yoshikawa et al. “Polarization-controlled single-mode VCSEL”. In: *IEEE Journal of Quantum Electronics* 34.6 (1998), pp. 1009–1015. DOI: 10.1109/3.678597.

[30] B. Weigl et al. “High-performance oxide-confined GaAs VCSELs”. In: *IEEE Journal of Selected Topics in Quantum Electronics* 3.2 (1997), pp. 409–415. DOI: 10.1109/2944.605686.

[31] H. C. Casey, D. D. Sell, and K. W. Wecht. “Concentration dependence of the absorption coefficient for n- and p-type GaAs between 1.3 and 1.6 eV”. In: *Journal of Applied Physics* 46.1 (1975), pp. 250–257. DOI: 10.1063/1.321330.

[32] C. Weisbuch and B. Vinter. “Chapter III - Optical Properties of Thin Heterostructures”. In: *Quantum Semiconductor Structures*. Ed. by C. Weisbuch and B. Vinter. San Diego: Academic Press, 1991, pp. 57–100. ISBN: 978-0-08-051557-1. DOI: https://doi.org/10.1016/B978-0-08-051557-1.50007-X.

[33] S Giugni and T L Tansley. “Comment on the compositional dependence of bandgap in AlGaAs and band-edge discontinuities in AlGaAs-GaAs heterostructures”. In: *Semiconductor Science and Technology* 7.8 (Aug. 1992), p. 1113. DOI: 10.1088/0268-1242/7/8/015.

[34] S. Schmitt-Rink, D.S. Chemla, and D.A.B. Miller. “Linear and nonlinear optical properties of semiconductor quantum wells”. In: *Advances in Physics* 38.2 (1989), pp. 89–188. DOI: 10.1080/00018738900101102.

[35] Nacer Debbar et al. “Coupled GaAs/AlGaAs quantum-well electroabsorption modulators for low-electric-field optical modulation”. In: *Journal of Applied Physics* 65.1 (Jan. 1989), pp. 383–385. ISSN: 0021-8979. DOI: 10.1063/1.342554.

[36] Ludovic Marigo-Lombart. “Vertical integration of an electro-absorption modulator onto a VCSEL for high-speed communications”. PhD thesis. Université Toulouse 3, 2018.

[37] G. lengyel, K.W. Jelley, and R.W.H. Engelmann. “A semi-empirical model for electroabsorption in GaAs/AlGaAs multiple quantum well modulator structures”. In: *IEEE Journal of Quantum Electronics* 26.2 (1990), pp. 296–304. DOI: 10.1109/3.44961.

[38] Andrea Irace et al. “Light Modulation with Silicon Devices”. In: *Silicon Photonics*. Berlin, Heidelberg: Springer Berlin Heidelberg, 2004, pp. 361–391. ISBN: 978-3-540-39913-1. DOI: 10.1007/978-3-540-39913-1_11.

[39] M.E. Chin and W.S.C. Chang. “Theoretical design optimization of multiple-quantum-well electroabsorption waveguide modulators”. en. In: *IEEE Journal of Quantum Electronics* 29.9 (Sept. 1993). Number: 9, pp. 2476–2488. ISSN: 00189197. DOI: 10.1109/3.247705. (Visited on 07/15/2020).

[40] M.K. Chin, P.K.L. Yu, and W.S.C. Chang. “Optimization of multiple quantum well structures for waveguide electroabsorption modulators”. In: *IEEE Journal of Quantum Electronics* 27.3 (1991), pp. 696–701. DOI: 10.1109/3.81379.

[41] T.G. Beck Mason. “Chapter 7 - Electroabsorption Modulators”. In: *WDM Technologies*. Ed. by Achyut K. Dutta, Niloy K. Dutta, and Masahiko Fujiwara. San Diego: Academic Press, 2002, pp. 249–314. ISBN: 978-0-12-225261-7. DOI: https://doi.org/10.1016/B978-012225261-7/50009-9.

[42] M. Whitehead et al. “Effects of well width on the characteristics of GaAs/AlGaAs multiple quantum well electroabsorption modulators”. In: *Applied Physics Letters* 53.11 (1988), pp. 956–958. DOI: 10.1063/1.100080.

[43] Richard T. Sahara, Ken Morito, and Haruhisa Soda. “Engineering of barrier band structure for electroabsorption MQW modulators”. In: *Electronics Letters* 30 (1994), pp. 698–699.

[44] A. M. Fox et al. “Excitons in resonant coupling of quantum wells”. In: *Phys. Rev. B* 42 (3 July 1990), pp. 1841–1844. DOI: 10.1103/PhysRevB.42.1841.

[45] Dong-Soo Shin. “Reduction in Escape Times of Photogenerated Charge Carriers with Asymmetric Intrastep Quantum Wells and Subsequent Improvement in Saturation Optical Intensity”. In: *Japanese Journal of Applied Physics* 45.12R (Dec. 2006), p. 9063. DOI: 10.1143/JJAP.45.9063.

[46] Takuya Ishikawa and Kunio Tada. “Observation of Quantum-Confined Stark Effect in a Graded-Gap Quantum Well”. en. In: *Japanese Journal of Applied Physics* 28.Part 2, No. 11 (). Publisher: JAPAN SOCIETY OF APPLIED PHYSICS,

pp. L1982–L1984. ISSN: 1347-4065. DOI: 10.1143/jjap.28.l1982. (Visited on 11/30/2022).

[47] L. D. Zhu et al. "GaAs/GaAlAs graded index separate confinement single quantum well single-mode waveguide electroabsorption light modulator". In: *IEE Proceedings J: Optoelectronics* 138.5 (Oct. 1991), pp. 313–318.

[48] M. Shahin et al. "80-Gbps NRZ-OOK Electro-Absorption Modulation of InP-on-Si DFB Laser Diodes". In: *IEEE Photonics Technology Letters* 31.7 (2019), pp. 533–536. DOI: 10.1109/LPT.2019.2900518.

[49] R.-H. Yan, R.J. Simes, and L.A. Coldren. "Surface-normal electroabsorption reflection modulators using asymmetric Fabry-Perot structures". In: *IEEE Journal of Quantum Electronics* 27.7 (1991), pp. 1922–1931. DOI: 10.1109/3.83394.

[50] Dr. Raymond C. Rumpf. *Transfer Matrix Method*. 2022. URL: https://empossible.thinkific.com/courses/tmmmatlab.

[51] Bardia Pezeshki, Dominique Thomas, and James S. Harris Jr. "Optimization of reflection electro-absorption modulators". In: *Physical Concepts of Materials for Novel Optoelectronic Device Applications II: Device Physics and Applications*. Ed. by Manijeh Razeghi. Vol. 1362. International Society for Optics and Photonics. SPIE, 1991, pp. 559–565. DOI: 10.1117/12.24565.

[52] D.S. Gerber, R. Droopad, and G.N. Maracas. "A GaAs/AlGaAs asymmetric Fabry-Perot reflection modulator with very high contrast ratio". In: *IEEE Photonics Technology Letters* 5.1 (1993), pp. 55–58. DOI: 10.1109/68.185059.

[53] J. A. Trezza et al. "High contrast asymmetric Fabry–Perot electro-absorption modulator with zero phase change". In: *Applied Physics Letters* 63.4 (1993), pp. 452–454. DOI: 10.1063/1.110021.

[54] Henry Kwong Hin Choy. "Design and fabrication of distributed Bragg reflectors for vertical-cavity surface-emitting lasers". PhD thesis. Massachusetts Institute of Technology, 1998.

[55] P. G. Newman et al. "Molecular beam epitaxial growth of vertical cavity surface emitting lasers with digital alloys and digital gradings". In: *Journal of Vacuum Science & Technology B: Microelectronics and Nanometer Structures Processing, Measurement, and Phenomena* 18.3 (2000), pp. 1619–1622. DOI: 10.1116/1.591439.

[56] Ron Kaspi and Giovanni P. Donati. "Digital alloy growth in mixed As/Sb heterostructures". en. In: *Journal of Crystal Growth* 251.1-4 (Apr. 2003), pp. 515–520. ISSN: 00220248. DOI: 10.1016/S0022-0248(02)02185-1. (Visited on 08/13/2020).

[57] P. Pellandini et al. "Dual-wavelength laser emission from a coupled semiconductor microcavity". In: *Applied Physics Letters* 71.7 (1997), pp. 864–866. DOI: 10.1063/1.119671.

[58] J. van Eisden et al. “Optically Decoupled Loss Modulation in a Duo-Cavity VCSEL”. In: *IEEE Photonics Technology Letters* 20.1 (2008), pp. 42–44. DOI: 10.1109/LPT.2007.912693.

[59] Marcel Brunner. “Design and characterization of single and dual cavity oxyde-apertured VCSELs”. In: (2000), p. 207. DOI: 10.5075/epfl-thesis-2290.

[60] Marian A. Herman and H. Sitter. “Molecular Beam Epitaxy: Fundamentals and Current Status”. In: 1989.

[61] Wikipedia contributors. *Molecular-beam epitaxy — Wikipedia, The Free Encyclopedia*. 2023. URL: https://en.wikipedia.org/wiki/Molecular-beam_epitaxy.

[62] A. Y. Cho and I. Hayashi. “Epitaxy of silicon doped gallium arsenide by molecular beam method”. In: *Metallurgical Transactions* 2.3 (Mar. 1971), pp. 777–780. ISSN: 2379-0083. DOI: 10.1007/BF02662735.

[63] Riber. *CBr4 Module for Gas Injector*. Technical Report. Riber, 2023. URL: https://www.riber.com/wp-content/uploads/2020/11/RIBER_CBr4-Module-for-Gas-Injector.pdf.

[64] K. Ben Saddik et al. “Growth of silicon- and carbon-doped GaAs by chemical beam epitaxy using H2-diluted DTBSi and CBr4 precursors”. In: *Journal of Crystal Growth* 571 (2021), p. 126242. ISSN: 0022-0248. DOI: https://doi.org/10.1016/j.jcrysgro.2021.126242.

[65] Alexandre Arnoult and Jonathan Colin. “Magnification inferred curvature for real-time curvature monitoring”. In: *Scientific Reports* 11 (Apr. 2021). DOI: 10.1038/s41598-021-88722-6.

[66] Kévin Louarn. “Development of tunnel junctions based on III-V semiconductors heterostructures for high efficiency multi-junction solar cells”. PhD thesis. Université Toulouse 3, 2018.

[67] Sadao Adachi. “GaAs, AlAs, and AlxGa1-xAs: Material parameters for use in research and device applications”. In: *Journal of Applied Physics* 58.3 (1985), R1–R29. DOI: 10.1063/1.336070.

[68] Lucas Laplanche et al. *Monolithically integrated 850-nm VCSEL / Electro-Absorption Modulator structures grown by MBE*. 22nd International Conference on Molecular Beam Epitaxy (ICMBE 2022). Poster. Sept. 2022. URL: https://laas.hal.science/hal-03727282.

[69] Anders Larsson and Johan S. Gustavsson. “Single-Mode VCSELs”. In: *VCSELs: Fundamentals, Technology and Applications of Vertical-Cavity Surface-Emitting Lasers*. Ed. by Rainer Michalzik. Berlin, Heidelberg: Springer Berlin Heidelberg, 2013, pp. 119–144. ISBN: 978-3-642-24986-0. DOI: 10.1007/978-3-642-24986-0_4.

[70] Yu-Chia Chang and Larry A. Coldren. “Efficient, High-Data-Rate, Tapered Oxide-Aperture Vertical-Cavity Surface-Emitting Lasers”. In: *IEEE Journal of Selected*

Topics in Quantum Electronics 15.3 (2009), pp. 704–715. DOI: 10.1109/JSTQE.2008.2010955.

[71] Gaël Lafleur. "Nouvelles architectures de composants photoniques par l'ingénierie du confinement électrique et optique". Theses. Université Paul Sabatier - Toulouse III, Dec. 2016.

[72] YC Chang et al. "High-efficiency, high-speed VCSELs with deep oxidation layers". In: *Electronics Letters* 42.22 (2006), p. 1.

[73] Robert W. Herrick et al. "Corrosion-Based Failure of Oxide-Aperture VCSELs". In: *IEEE Journal of Quantum Electronics* 49.12 (2013), pp. 1045–1052. DOI: 10.1109/JQE.2013.2285572.

[74] Ricardo Rosales, Martin Zorn, and James A. Lott. "30-GHz Bandwidth With Directly Current-Modulated 980-nm Oxide-Aperture VCSELs". In: *IEEE Photonics Technology Letters* 29.23 (2017), pp. 2107–2110. DOI: 10.1109/LPT.2017.2764626.

[75] Natan Monvoisin et al. "Improved optical inspection of lateral III-V-semiconductor oxidation afforded by a spectrally-shaped illumination". In: *Conference on Lasers and Electro-Optics/Europe (CLEO/Europe 2023) and European Quantum Electronics Conference (EQEC 2023)*. Optica Publishing Group, 2023.

[76] Ludovic Marigo-Lombart et al. "Electro-Absorption Modulator Vertically Integrated on a VCSEL: Microstrip-Based High-Speed Electrical Injection on Top of a BCB Layer". In: *Journal of Lightwave Technology* 37.15 (2019), pp. 3861–3868. DOI: 10.1109/JLT.2019.2921806.

[77] He Gao et al. "Air Cushion Press for Excellent Uniformity, High Yield, and Fast Nanoimprint Across a 100 mm Field". In: *Nano Letters* 6.11 (Nov. 2006). Publisher: American Chemical Society, pp. 2438–2441. ISSN: 1530-6984. DOI: 10.1021/nl0615118.

[78] Dow Chemical Company. *CYCLOTENE 4000 Series Advanced Electronic Resins (Photo BCB)*. 2005. URL: https://wiki.nanofab.ucsb.edu/w/images/b/b6/Cyclotene_4000_Resin_MSDS.pdf.

[79] Scipy Developers. *scipy.optimize*. 2023. URL: https://docs.scipy.org/doc/scipy/tutorial/optimize.html.

[80] Udo W. Pohl. "Methods of Epitaxy". In: *Epitaxy of Semiconductors: Introduction to Physical Principles*. Berlin, Heidelberg: Springer Berlin Heidelberg, 2013, pp. 275–313. ISBN: 978-3-642-32970-8. DOI: 10.1007/978-3-642-32970-8_7.

[81] H. Goronkin et al. "Ohmic contact penetration and encroachment in GaAs/AlGaAs and GaAs FETs". In: *IEEE Transactions on Electron Devices* 36.2 (1989), pp. 281–288. DOI: 10.1109/16.19927.

[82] D.H Zhang. “Metal contacts to n-type AlGaAs grown by molecular beam epitaxy”. In: *Materials Science and Engineering: B* 60.3 (1999), pp. 189–193. ISSN: 0921-5107. DOI: https://doi.org/10.1016/S0921-5107(99)00076-8.

[83] Yen-Chung Lin and Tah-Hsiung Chu. “Multiport Scattering Matrix Determination From One-Port Measurements”. en. In: *IEEE Transactions on Microwave Theory and Techniques* 63.7 (July 2015). Number: 7, pp. 2343–2352. ISSN: 0018-9480, 1557-9670. DOI: 10.1109/TMTT.2015.2436400. (Visited on 04/13/2022).

[84] NumPy Developers. *numpy.linalg.solve*. 2023. URL: https://numpy.org/doc/stable/reference/generated/numpy.linalg.solve.html.

[85] Valerio Torrelli et al. “Analytical model of the Ultrabroadband Operation of Transverse-Coupled-Cavity VCSELs”. In: ().

[86] Stefan Birner et al. “nextnano: General Purpose 3-D Simulations”. In: *IEEE Transactions on Electron Devices* 54.9 (2007), pp. 2137–2142. DOI: 10.1109/TED.2007.902871.

8 Annex

8.1 EAM-VCSEL process

Process : EAM – VCSEL

	N-Type substrate	GaAs			Laplanche

Date	Step	Details	Device	Parameters	Notes

1. EAM top contact

1.1. Sample Cleaning

	Cleaning	Acetone Isopropanol				
	Drying	N2				
	Heating	100°C		2min		

1.2. Photolithography

	Spin-coating	LOR 30B 2.4µm	Recipe #40	3000rpm 30s 4000rpm 1s	Spray N2 before applying resin	
	Bake	170°C		5min		
	Spin-coating	SPR 700 2.3µm	Recipe #42	1200rpm 30s 3500rpm 1s		
	Bake	95°C		60s		
	Insulation	Hard contact	Gen4 MA6	190mJ/cm2	Mask L1	
	Post-exposure baking	115°C		60s		
	Development	Mf Cd-26		35s		
	Rinsing	DI H2O				
	Drying	N2				
	Optical microscope check		MX50			
	Resin thickness measurement		TENCOR			

1.3. Metallization Ti Au

	Deoxidization	HCL:H2O 1:10		1min	Right before introduction in the deposit frame	
	Rinsing	DI H20				
	Drying	N2				
	Heating	100°C		2min		
	Deposit	Ti	EVA600	50nm		
	Deposit	Au	EVA600	500nm		

1.4. Metal lift-off

	Lift-Off	DMSO		80°C		
	Cleaning	Acetone Isopropanol				
	Drying	N2				
	Heating	100°C		2min		
	Optical microscope check		MX50			
	Metal thickness measurement		TENCOR			

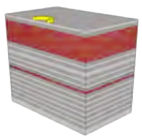

Date	Step	Details	Device	Parameters	Notes

2. EAM mesa etch

2.1. Sample Cleaning

	Cleaning	Acetone Isopropanol				
	Drying	N2				
	Heating	100°C		2min		

2.2. Photolithography

	Spin-coating	SPR 700 2.3µm	Recipe #42	1200rpm 30s 3500rpm 1s	Spray N2 before applying resin	
	Bake	95°C		60s		
	Insulation	Hard contact	Gen4 MA6	190mJ/cm2	Mask L2	
	Development	Mf Cd-26		~60s	Stop when resin visually disappear	
	Rinsing	DI H2O				
	Drying	N2				
	Optical microscope check		MX50			
	Resin thickness measurement		TENCOR			

2.3. Dry etching

	Stick sample on susceptor	Fomblin oil				
	Mesa etching	Cl2 20sccm N2 50sccm	ICP3	several minutes	Recipe T1E2050 with end-point detection system to stop the etching at the middle contact	
	Transport in acetone	Acetone			Put in **fomblin contaminated** acetone bottle	
	Remove fomblin oil	PFS 1min HFE 1min Acetone 1min				
	Transport in acetone	Acetone			Put in **non**-fomblin contaminated acetone bottle	
	Remove resin	DMSO		80°C		
	Mesa thickness measurement		TENCOR			

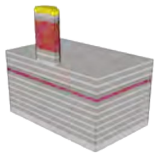

Date	*Step*	*Details*	*Device*	*Parameters*	*Notes*	

3. VCSEL top contact

3.1. Sample Cleaning

	Cleaning	Acetone Isopropanol				
	Drying	N2				
	Heating	100°C		2min		

3.2. Photolithography

	Spin-coating	LOR 30B 2.4µm	Recipe #40	3000rpm 30s 4000rpm 1s	Spray N2 before applying resin	
	Bake	170°C		5min		
	Spin-coating	SPR 700 2.3µm	Recipe #42	1200rpm 30s 3500rpm 1s		
	Bake	95°C		60s		
	Insulation	Hard contact	Gen4 MA6	190mJ/cm2	Mask L3	
	Post-exposure baking	115°C		60s		
	Development	Mf Cd-26		30s		
	Rinsing	DI H2O				
	Drying	N2				
	Optical microscope check		MX50			
	Resin thickness measurement		TENCOR			

3.3. Metallization Ti Au

	Deoxidization	HCL:H2O 1:10		1min	Right before introduction in the deposit frame	
	Rinsing	DI H20				
	Drying	N2				
	Heating	100°C		2min		
	Deposit	Ti	EVA600	50nm		
	Deposit	Au	EVA600	500nm		

3.4. Metal lift-off

	Lift-Off	DMSO		80°C		
	Cleaning	Acetone Isopropanol				
	Drying	N2				
	Heating	100°C		2min		
	Optical microscope check		MX50			
	Metal thickness measurement		TENCOR			
	Electron beam microscopy		C-FIB			

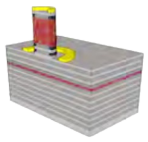

Date	*Step*	*Details*	*Device*	*Parameters*	*Notes*	

4. EAM passivation, VCSEL etching and oxidation

4.1. Sample Cleaning

	Cleaning	Acetone Isopropanol				
	Drying	N2				
	Heating	100°C		2min		

4.2. SiOx deposit						
	ICPECVD	SiOx	T-CVD	300nm 8nm/min	Recipe adr-SiOxGuilhem100C-cor	

4.3. Photolithography						
	Spin-coating	SPR 700 2.3µm	Recipe #42	1200rpm 30s 3500rpm 1s		
	Insulation	Hard contact	Gen4 MA6	190mJ/cm2	Mask L4	
	Development	Mf Cd-26		30s		
	Rinsing	DI H2O				
	Drying	N2				
	Optical microscope check		MX50			
	Resin thickness measurement		TENCOR			

4.4. SiOx etching						
	Stick sample on susceptor	Fomblin oil				
	SiOx etching	CF4 40sccm	SI-500 Fluor	ICP:RF 500:40 5mTorr 17°C	In-situ measurement on ground plane zone ; Chiller set up on 0°C	
	Remove fomblin oil	PFS 1min HFE 1min Acetone 1min IPA 1min				
	Rinsing	DI H2O				
	Mesa thickness measurement		TENCOR			

4.5. Mesa etching						
	Stick sample on susceptor	Fomblin oil				
	Mesa etching	Cl2 20sccm N2 50sccm	ICP3	several minutes	Recipe T1E2050 with end-point detection system to stop the etching at the middle contact	
	Transport in acetone	Acetone			Put in **fomblin contaminated** acetone bottle	
	Remove fomblin oil	PFS 1min HFE 1min Acetone 1min				
	Transport in acetone	Acetone			Put in **non**-fomblin contaminated acetone bottle	
	Remove resin	DMSO		80°C		
	Mesa thickness measurement		TENCOR			

4.6. Oxide aperture						
	Deoxidization	HCL:H2O 1:10		30s	Right before introduction in the deposit frame	
	Rinsing	DI H20				
	Drying	N2				
	Heating	100°C		2min		
	Oxydation					

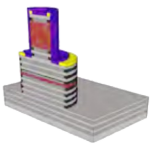

Date	*Step*	*Details*	*Device*	*Parameters*	*Notes*

5. VCSEL passivation

5.1. Sample Cleaning						
	Cleaning	Acetone Isopropanol				
	Drying	N2				
	Heating	100°C		2min		

5.2. SiOx deposit						
	ICPECVD	SiOx	T-CVD	300nm 8nm/min		

5.3. Photolithography						
	Spin-coating	SPR 700 2.3µm	Recipe #42	1200rpm 30s 3500rpm 1s		
	Insulation	Hard contact	Gen4 MA6	190mJ/cm2	Mask L5	
	Development	Mf Cd-26		30s		
	Rinsing	DI H2O				
	Drying	N2				
	Optical microscope check		MX50			

	Resin thickness measurement		TENCOR			

5.4. Dry etching

	Stick sample on susceptor	Fomblin oil				
	SiOx etching	CF4 40sccm	SI-500 Fluor	ICP:RF 500:40 5mTorr 17°C	In-situ measurement on middle contact test pattern; Chiller set up on 0°C	
	Remove fomblin oil	PFS 1min HFE 1min Acetone 1min IPA 1min				
	Rinsing	DI H2O				
	Mesa thickness measurement		TENCOR			

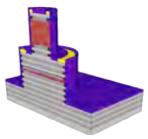

Date	*Step*	*Details*	*Device*	*Parameters*	*Notes*	

6. Ground contact

6.1. Sample Cleaning

	Cleaning	Acetone Isopropanol				
	Drying	N2				
	Heating	100°C		2min		

6.2. Photolithography

	Spin-coating	LOR 30B 2.4µm	Recipe #40	3000rpm 30s 4000rpm 1s	Spray N2 before applying resin	
	Bake	170°C		5min		
	Spin-coating	SPR 700 2.3µm	Recipe #42	1200rpm 30s 3500rpm 1s		
	Bake	95°C		60s		
	Insulation	Hard contact	Gen4 MA6	190mJ/cm2	Mask L6	
	Post-exposure baking	115°C		60s		
	Development	Mf Cd-26		30s		
	Rinsing	DI H2O				
	Drying	N2				
	Optical microscope check		MX50			
	Resin thickness measurement		TENCOR			

6.3. Metallization Ti Au

	Deoxidization	HCL:H2O 1:10		1min	Right before introduction in the deposit frame	
	Rinsing	DI H20				
	Drying	N2				
	Heating	100°C		2min		
	Deposit	Ti	EVA600	50nm		
	Deposit	Au	EVA600	500nm		

6.4. Metal lift-off

	Lift-Off	DMSO		80°C		
	Cleaning	Acetone Isopropanol				
	Drying	N2				
	Heating	105°C		2min		
	Optical microscope check		MX50			
	Metal thickness measurement		TENCOR			

Date	*Step*	*Details*	*Device*	*Parameters*	*Notes*	

7. BCB planarization

7.1. Sample Cleaning

	Cleaning	Acetone Isopropanol				
	Drying	N2				
	Heating	100°C		2min		

7.2. Spin-coating

	Adhesion promoter	AP3000	Tournette	Recipe “spincoat AP3000”	Blue tape	
	Spin-coating	BCB		6000rpm 600rpm/s 40s		
	Bake	80°C		1min		

7.3. Nano-imprint

	Pump		Nanonex	2min		
	Pre-imprint	100°C	Nanonex			
	Pre-pressure	120PSI	Nanonex			
	Nano-imprint	120°C 250PSI	Nanonex	6min		
	Vent		Nanonex		Wait for temperature to decrease to 50°C	

Date	*Step*	*Details*	*Device*	*Parameters*	*Notes*

8.1. BCB photolithography and via opening

	Insulation	Hard contact	Gen4 MA6	360mJ/cm2	Mask L7	
	Development	DS3000		30-35°C 10min	Use a test sample before	
	Rinsing	DS3000		Ambiant 2min		
	Rinsing	DI H2O		2min		
	Drying	N2	Tournette	6000rpm 600rpm/s 2min	Spray N2 above sample while rotating in spin coater	
	Optical microscope check		MX50			
	Resin thickness measurement		TENCOR			

8.2. BCB annealing

	Annealing		T-FOUR T9	250°C	Recipe ludo test2 BCB	

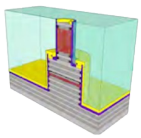

Date	*Step*	*Details*	*Device*	*Parameters*	*Notes*

9. BCB and SiOx etching

9.1. Dry etching

	Stick sample on susceptor	Fomblin oil				
	BCB etching	O2 99sccm SF6 2sccm	SI-500 Fluor	ICP:RF 500:40 70mTorr 17°C	In-situ measurement on “BCB etch / Au” pattern ; BCB 220nm/min ; SiOx 27nm/min ; Chiller set up on 0°C	
	SiOx etching	CHF3	SI-500 Fluor	ICP:RF 17°C	In-situ measurement on “BCB etch / Au + SiOx” pattern ; SiOx 120nm/min ; Chiller set up on 0°C	
	Remove fomblin oil	PFS 1min HFE 1min Acetone 1min IPA 1min				
	Rinsing	DI H2O				
	Mesa thickness measurement		TENCOR			

Date	*Step*	*Details*	*Device*	*Parameters*	*Notes*

10. Top HF contact

10.1. Sample Cleaning

	Cleaning	Acetone Isopropanol				
	Drying	N2				
	Heating	100°C		2min		

10.2. Photolithography

	Spin-coating	LOR 30B 2.4µm	Recipe #40	3000rpm 30s 4000rpm 1s	Spray N2 before applying resin	
	Bake	170°C		5min		
	Spin-coating	SPR 700 2.3µm	Recipe #42	1200rpm 30s 3500rpm 1s	Spray N2 before applying resin	
	Bake	95°C		60s		
	Insulation	Hard contact	Gen4 MA6	190mJ/cm2	Mask L8	
	Post-exposure baking	115°C		60s		
	Development	Mf Cd-26		30s		
	Rinsing	DI H2O				

	Drying	N2				
	Optical microscope check		MX50			
	Resin thickness measurement		TENCOR			

10.3. Metallization Ti Au

	Deoxidization	HCL:H2O 1:10		1min	Right before introduction in the deposit frame	
	Rinsing	DI H20				
	Drying	N2				
	Heating	100°C		2min		
	Deposit	Ti	EVA600	50nm		
	Deposit	Au	EVA600	500nm		

10.4. Metal lift-off

	Lift-Off	DMSO		80°C		
	Cleaning	Acetone Isopropanol				
	Drying	N2				
	Heating	100°C		2min		
	Optical microscope check		MX50			
	Metal thickness measurement		TENCOR			

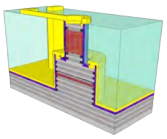

Date	*Step*	*Details*	*Device*	*Parameters*	*Notes*

8.2 Résumé en français

Table

1 Introduction et contexte

La demande persistante d'un accès plus rapide aux données a stimulé la croissance des centres de données massifs et des infrastructures associées en raison de l'augmentation du trafic internet. Des facteurs tels que l'augmentation du nombre d'utilisateurs d'internet, la connectivité des appareils, les connexions de machine à machine et l'augmentation des débits ont contribué à cette croissance. L'expansion du standard 4K, des vidéoconférences, du travail à distance, des jeux vidéos ont encore stimulé la demande mondiale en bande passante. Toutefois, cette demande a dépassé l'augmentation des débits des lignes, ce qui nécessite des interconnexions supplémentaires.

Le marché des émetteurs-récepteurs optiques, en particulier dans les centres de données et les télécommunications, est crucial. Le chiffre d'affaires des émetteurs-récepteurs optiques dans les centres de données devrait connaître une croissance substantielle. Les lasers à cavité verticale (VCSEL) jouent un rôle clé dans la résolution des problèmes rencontrés par les centres de données et les ordinateurs à haute performance (HPC).

1.1 Centre de données et ordinateurs haute-performance

Un centre de données est une installation centralisée utilisée pour stocker, traiter et distribuer de grands volumes de données, à des fins diverses telles que le commerce électronique, la vidéo à la demande, la vidéoconférence, et le stockage de données. Les centres de données varient en taille, allant de petites salles dédiées à des bâtiments massifs. Les dix plus grands centres de données au monde couvrent une superficie combinée de 2,3 millions de mètres carrés et s'appuient sur les interconnexions optiques pour leur rentabilité, leur flexibilité et la réduction de l'encombrement.

Les ordinateurs haute performance (HPC) se composent de processeurs en parallèle pour des réaliser des calculs difficiles, tels que les simulations, la conception de médicaments, la cosmologie et l'informatique cloud. En 2022, le HPC "Frontier" atteindra pour la première fois une puissance de calcul exaflopique. Les interconnexions optiques sont cruciales pour le calcul intensif, en raison de facteurs tels que l'intégration compacte des émetteurs-récepteurs, la flexibilité mécanique des fibres optiques et la nécessité de réduire au minimum la latence dans la transmission des données entre les processeurs et la mémoire. Les centres de calcul intensif nécessitent généralement un débit de un byte par opération à virgule flottante (FLOP), et l'on estime que les centres de données et les centres de calcul intensif utilisent près d'un milliard de VCSELs dans le monde entier.

1.2 Progrès des VCSEL pour les applications de modulation directe

1.2.1 Formats d'encodage

Les trois méthodes d'encodage les plus courantes pour moduler directement les VCSELs sont les suivantes :

NRZ-OOK : Codage simple à deux niveaux avec une faible efficacité spectrale (1 bit/s/Hz).

PAM-4 : modulation d'amplitude d'impulsion à quatre niveaux, qui augmente l'efficacité spectrale mais nécessite un rapport signal/bruit plus élevé et des circuits plus complexes que le NRZ-OOK.

QAM-OFDM : modulation d'amplitude en quadrature avec multiplexage par répartition orthogonale de la fréquence, qui offre l'efficacité spectrale la plus élevée mais nécessite des circuits complexes.

1.2.2 VCSELs dans le cas de l'encodage NRZ-OOK

Concernant le NRZ-OOK, il est difficile d'atteindre le plafond de 100 Gbit/s en raison de sa faible efficacité spectrale. Pour dépasser cette limite, deux options sont possibles : utiliser un réseau de VCSEL pour agréger les débits de données ou opter pour des formats de codage différents tels que PAM-4 ou QAM-OFDM.

1.2.3 VCSELs dans le cas de l'encodage PAM-4 et QAM-OFDM

Le PAM-4, comparé au NRZ-OOK, double généralement les débits de données, franchissant la barre des 100 Gbit/s. Les VCSEL, lorsqu'ils sont utilisés avec le PAM-4, ont atteint des débits de données impressionnants, avec des exemples récents atteignant 200 Gbit/s sur 100 m de fibre multimode.

Le QAM-OFDM est généralement choisi en raison de son efficacité spectrale élevée, permettant des débits de données allant jusqu'à 100 Gbit/s. Les circuits de commande nécessaires à son utilisation entraînent des coûts, une consommation d'énergie, une production de chaleur et un encombrement, ce qui en fait un facteur critique pour les centres de données et les applications HPC. La transition du NRZ-OOK au PAM-4 est en cours dans les centres de données, et le M-QAM-OFDM commence à s'implémenter progressivement.

1.3 Potentiel des EAMs

1.3.1 Etat de l'art des modulateurs à lumière incidente normale

Le débit de données obtenu avec les VCSEL a régulièrement augmenté, et la recherche se concentre désormais sur des méthodes telles que le dopage métallique et l'optimisation des capacités parasites pour améliorer la bande passante.

Une approche innovante consiste à séparer les fonctions d'émission et de modulation, en utilisant des modulateurs à électro-absorption (EAM) dédiés à la modulation. Les EAMs à lumière incidente normale, connus sous le nom de SNEAMs, présentent des avantages tels qu'une intégration simplifiée, une taille compacte, une faible consommation d'énergie et une vitesse de modulation élevée. En 2020, Iannone a atteint 65 Gbit/s avec des SNEAM, et Grillanda a atteint 107 Gbit/s avec des versions à puce nue, démontrant ainsi leur potentiel pour les communications optiques à grande vitesse.

1.3.2 Etat de l'art des modulateurs integrés à un VCSEL

L'intégration d'un VCSEL (Vertical Cavity Surface-Emitting Laser) et d'un EAM (Electro-Absorption Modulator) à surface normale est possible en raison de la similitude de leurs structures de cavité optique Fabry-Pérot. Lorsqu'elles sont épitaxiées, les deux cavités peuvent être alignées avec précision en utilisant les mêmes matériaux.

Dans une cavité, la lumière produit une ondes stationnaire à une fréquence spécifique. Lorsque deux cavités ont une fréquence identique, elles sont couplées. Toutefois, si l'on désaccorde les cavités en ajustant la longueur de l'une d'entre elles, on obtient des fréquences différentes. Si les fréquences deviennent trop différentes, l'EAM ne peut pas absorber efficacement les photons du VCSEL.

Des recherches ont exploré les effets du couplage d'une cavité à un VCSEL, révélant que ce couplage peut entraîner des problèmes de fonctionnement du composant. Ce couplage influence considérablement la conception et les performances du dispositif.

Plusieurs études ont permis d'obtenir des bandes passantes avec des structures VCSEL-EAM intégrées. Par exemple, en 2007, Eisden a obtenu une bande passante de 17 GHz pour un VCSEL de 980 nm avec un EAM intégré. En 2014, Dalir a atteint une bande passante de 35 GHz avec une structure qui intègre latéralement l'EAM sur le côté du VCSEL à une longueur d'onde de 850 nm. En 2018, Marigo-Lombart a démontré un EAM intégré verticalement sur un VCSEL avec une bande passante de 29 GHz.

1.4 Principe de fonctionnement des VCSELs et EAMs

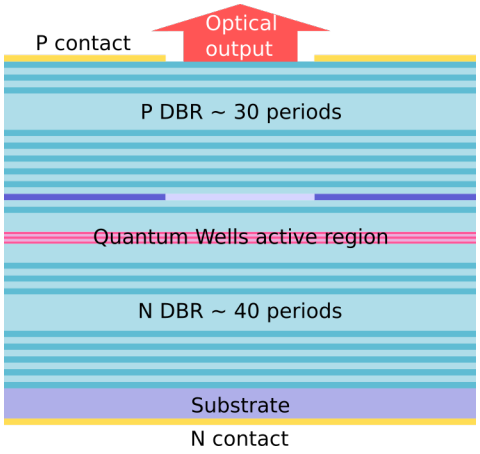

Figure 1: Diagrame d'un VCSEL avec ouverture d'oxide.

1.4.1 VCSELs

Les VCSELs diffèrent des lasers traditionnels émettant par la tranche en émettant de la lumière perpendiculairement à la surface du substrat. Ils utilisent des réflecteurs de Bragg distribués (DBR) pour former une cavité optique avec une réflectivité exceptionnellement élevée. Malgré la faible longueur de la cavité (environ 100 nm), les VCSEL permettent d'obtenir un gain optique grâce à leurs réflecteurs de Bragg distribués très réfléchissants.

Les VCSELs en $AlGaAs$ sont généralement constitués d'un DBR supérieur d'environ 30 périodes et d'un DBR inférieur d'environ 40 périodes. La région active, qui assure le gain, comprend trois puits quantiques d'une épaisseur de 5 à 15 nm et des barrières de confinement d'environ 10 nm avec une teneur en aluminium de 20 à 40%. La longueur d'onde d'émission est déterminée par la bande interdite des puits quantiques, généralement autour de 850 nm.

Les VCSEL ont gagné en popularité en raison de leur intégration, des faibles courants de seuil, de leur fiabilité et de la possibilité de créer des matrices de VCSELs, ce qui les rend polyvalents et bien adaptés aux applications de communication optique. Leur faible divergence et leur compatibilité avec les fibres monomodes les rendent encore plus adaptés aux systèmes optiques.

1.4.2 EAMs

L'effet Stark à confinement quantique (QCSE) permet de moduler l'absorption dans les matériaux semi-conducteurs. En créant un puits de potentiel dans un matériau tel que $Al_{0.3}Ga_{0.7}As$ avec une couche de $GaAs$ entre deux couches de $AlGaAs$, on obtient un confinement quantique. Lorsqu'un champ électrique est appliqué, le QCSE déplace les fonctions d'onde des électrons et des trous, modifiant leur superposition et donc l'absorption des photons. L'application du champ électrique parallèlement ou perpendiculairement aux couches du puits quantique conduit à un comportement d'absorption distinct, les champs électriques perpendiculaires offrant une modulation de l'absorption plus prononcée et convenant aux dispositifs d'électro-absorption.

1.5 Conclusion

La demande croissante d'un accès plus rapide aux données, due à l'augmentation de l'utilisation de l'internet et des activités nécessitant une grande largeur de bande, a conduit à l'expansion des centres de données et des installations de calcul à haute performance (HPC). Pour répondre à cette demande, les stratégies actuelles consistent à combiner la technologie VCSEL, des formats d'encodage complexes et des circuits de commande. Cependant, les travaux présentés dans cette thèse proposent une approche alternative, l'EAM-VCSEL, où les fonctions d'émission et de modulation sont découplées pour atteindre des débits de données plus élevés et surmonter les limitations des VCSEL à modulation directe, le tout dans un seul composant intégré.

Cette recherche s'appuie sur une thèse précédente menée au LAAS-CNRS par L. Marigo-Lombart. L'objectif de ce travail est d'améliorer la conception de l'EAM-VCSEL, de résoudre les problèmes de couplage entre les cavités, d'établir des méthodes de couplage précises, de réduire les pertes électriques et d'améliorer les processus de fabrication critiques.

Cette thèse met principalement l'accent sur le modulateur lui-même. Le deuxième chapitre traite de la conception et de la modélisation de l'EAM-VCSEL, en mettant l'accent sur la maximisation de l'effet Stark confiné quantique (QCSE) pour améliorer la dynamique d'absorption et atténuer les effets parasites tels que l'impédance du DBR et le couplage. Le troisième chapitre traite du processus de fabrication, couvrant diverses étapes de fabrication et abordant des aspects critiques tels que l'ouverture de l'oxide et le packaging BCB. Le dernier chapitre détaille la caractérisation de l'EAM, y compris son fonctionnement à haute fréquence.

2 Design et modélisation

Ce chapitre explore les considérations de conception de l'EAM-VCSEL dans le but d'optimiser sa réponse optique pour une entrée électrique donnée. La modulation de l'absorption optique dans ce dispositif repose sur l'effet Stark confiné quantiquement (QCSE). D'un point de vue électrique, les puits quantiques multiples (MQW) sont les seuls contributeurs à la modulation de l'absorption, la polarisation électrique étant idéalement appliquée aux limites des MQW. Cependant, pour faciliter la fabrication, la polarisation doit traverser les réflecteurs de Bragg distribués (DBR).

Dans la zone de modulation intrinsèque (les MQW), il est essentiel de maximiser le déplacement du pic d'absorption par unité de polarisation électrique pour obtenir un rapport de contraste élevé. Les puits quantiques ont une limite naturelle au nombre de porteurs de charge qu'ils peuvent accueillir. Lorsque la saturation se produit dans un puits quantique, celui-ci ne peut plus absorber de photons, ce qui limite l'absorption ultérieure. Il est donc essentiel de faciliter l'élimination des porteurs de charge pour améliorer le taux de modulation.

Les DBRs servent principalement à confiner la lumière dans l'EAM mais ne contribuent pas directement à la modulation de l'absorption électrique. D'un point de vue électrique, ils sont extrinsèques au contrôle de l'absorption. Une résistance excessive dans les DBRs peut introduire des constantes de temps significatives en raison d'une capacité parasite même mineure, limitant ainsi la largeur de bande du dispositif. Étant donné que les DBRs présentent intrinsèquement une résistance élevée en tant qu'hétérojonctions, la minimisation de cette résistance est un élément clé de la conception du dispositif.

2.1 Design de la cavité de l'EAM

2.1.1 Modélisation de l'absorption

Dans ce chapitre, l'accent est mis sur l'optimisation de l'EAM-VCSEL en tenant compte de l'effet Stark à confinement quantique et de ses facteurs d'influence. Les paramètres critiques pris en compte sont la forme et les dimensions du puits quantique, la teneur en aluminium dans les barrières de confinement et le champ électrique perpendiculaire.

L'étude se concentre sur les puits quantiques réguliers, en mettant en œuvre un modèle semi-empirique développé par Lengyel et al. qui calcule l'absorption dans les puits quantiques en fonction de paramètres essentiels, notamment la teneur en alu-

minium dans les barrières de confinement, l'épaisseur du puits quantique et le champ électrique appliqué.

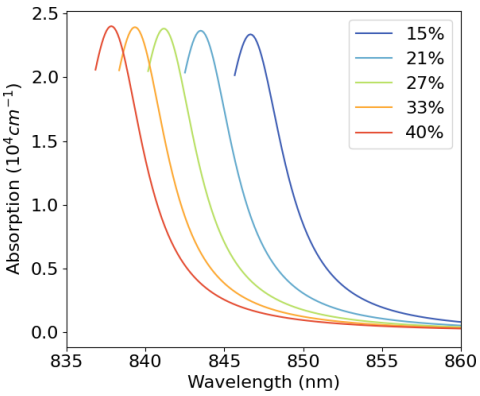

(a) En fonction de différentes fraction d'aluminium.

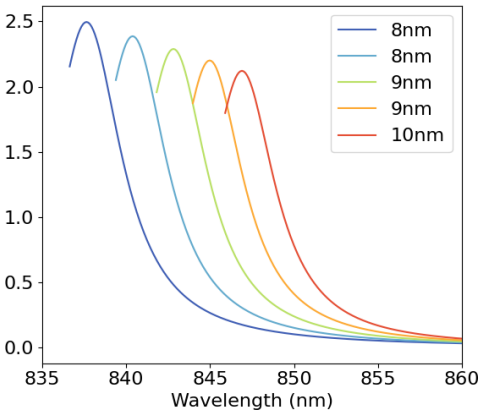

(b) En fonction de l'épaisseur des puits quantiques.

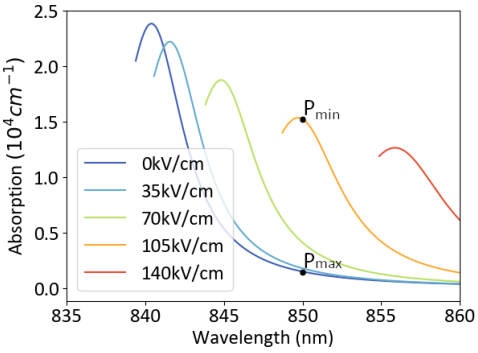

(c) En fonction du champ électrique.

Figure 2: Dépendance spectrale de l'absorption d'un puits quantique seul pour différentes concentrations d'aluminium dans la barrière de confinement (a), largeurs de puits quantique (b) et champs électriques appliqués (c)..

Les résultats du modèle indiquent que la diminution de la barrière de potentiel déplace le pic d'absorption vers le rouge sans en réduire l'ampleur. La réduction de l'épaisseur du puits quantique augmente le pic d'absorption et le déplace vers le bleu. En outre, l'augmentation du champ électrique entraîne une légère réduction et un décalage vers le rouge du pic d'absorption.

2.1.2 Optimisation de la dynamique de modulation

Comme expliqué dans la partie précédente, l'objectif du modulateur d'électro-absorption est de fournir une sortie lumineuse avec deux ou plusieurs puissances optiques différentes, ce qui est obtenu en utilisant différentes valeurs d'absorption. Pour obtenir le meilleur

rapport de contraste, le modulateur d'électro-absorption doit être optimisé de manière à ce que la différence de potentiel électrique minimale entraîne une modulation d'absorption maximale.

La capacité du modulateur à atteindre son objectif est généralement décrite par la profondeur de modulation η :

$$\eta = \frac{P_{max} - P_{min}}{P_{min}} \tag{1}$$

Le facteur m_E quantifie l'augmentation du champ électrique pour une variation donnée de l'absorption. Ainsi, pour obtenir un rapport de contraste élevé, le Δm_E doit être minimisé, tandis que m_α doit être maximisé, ce qui peut être résumé à l'aide du facteur de mérite suivant :

$$f_{merit} = \frac{m_\alpha}{m_E} = \frac{\Delta\alpha^2}{\alpha_{\text{on}}\Delta E^2} \tag{2}$$

Ce facteur de mérite peut être extrait du modèle de Lengyel pour un ensemble de barrières de confinement différentes, la teneur en aluminium, la largeur du puits quantique et le delta du champ électrique, ce qui permet de trouver la configuration optimale des puits quantiques, comme le montre la figure 3.

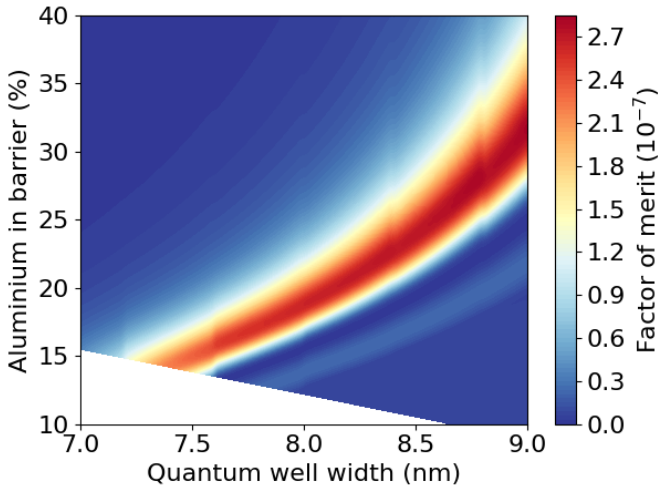

Figure 3: Figure de mérite d'un puits quantique unique du modulateur d'électroabsorption pour un champ électrique delta de $80 - 60kV.cm^{-1}$ à une longueur d'onde de $850nm$.

La zone d'intérêt avec un facteur de mérite élevé est en rouge, donnant un ensemble de configurations optimisées possibles pour les paramètres du puits quantique et de la barrière de confinement, tandis que les zones bleues correspondent aux configurations

à éviter. Les modulateurs à électroabsorption ont généralement des puits quantiques d'une épaisseur d'environ 9 à 12nm, et des barrières de confinement d'une teneur en aluminium d'environ 30%. Mais comme le montre notre figure de mérite, la teneur en aluminium peut être réduite si nécessaire.

2.1.3 Temps de fuite

Dans les puits quantiques semi-conducteurs, l'évacuation des porteurs de charge générés par les photons absorbés est cruciale pour éviter la saturation. Les deux mécanismes d'évacuation sont l'effet tunnel et l'émission thermionique. Dans la configuration proposée, l'émission thermionique domine et dépend de la teneur en aluminium. Une modeste réduction de 10% de la teneur en aluminium diminue considérablement le temps d'évacuation des trous lourds. Les structures $AlGaAs$ VCSEL et EAM ont typiquement des barrières de confinement avec une teneur en aluminium d'environ $30 - 40\%$, qui pourrait être réduite pour améliorer les performances.

Le temps de fuite des porteurs de charge est crucial pour déterminer la fréquence de modulation maximale d'un dispositif, car il régit la vitesse à laquelle les porteurs de charge peuvent sortir du puit quantique. Un temps de fuite de $\tau = 1.10^{-11}$ secondes fixe une limite supérieure pour la fréquence de modulation de $100GHz$.

2.1.4 Structure de la cavité

Pour obtenir des performances de modulation comparables à celles des lasers à émission par la tranche pour les EAM, la cavité optique doit être épaisse, plus d'une centaine de micromètres, ce qui ne peut pas être obtenu par épitaxie. L'encapsulation de la cavité dans une structure Fabry-Perot asymétrique confine la lumière, augmentant l'interaction entre les photons et les puits quantiques.

L'abaissement de la teneur en aluminium dans les barrières de confinement à environ 20% (au lieu des 30% habituels) améliore l'évacuation des porteurs de charge. Le facteur de mérite présente un ensemble de configurations de puits quantiques simples et de barrières de confinement compatibles avec les résultats de l'évacuation des porteurs de charge. Avec une barrière de confinement en aluminium de 22%, une épaisseur de puits quantique de 8,3nm est suggérée.

La cavité optique pour l'EAM, conçue pour une longueur d'onde d'application de 850 nm, devrait avoir une longueur qui est un multiple de l'épaisseur de la demi-onde pour assurer des interférences constructives et la transparence. Compte tenu de la configuration du puits quantique et de la barrière de confinement de 10 nm, une longueur de cavité quatre fois supérieure à l'épaisseur de la demi-onde est choisie. Il en

résulte une cavité contenant 24 barrières de confinement et 25 puits quantiques, avec 36 nm de couches de cladding.

2.2 Design de l'EAM-VCSEL

2.2.1 Structure de l'EAM

La structure standard du modulateur à électro-absorption est basée sur la conception originale de Marigo Lombart. Elle comprend un DBR supérieur à 6 périodes et un DBR inférieur à 8 périodes, incorporant des gradations d'alliage numérique de 20 nm d'épaisseur aux interfaces. Dans la cavité optique, la fraction d'aluminium dans la barrière de confinement est réduite à 21%, et l'épaisseur des puits quantiques est fixée à 8,27 nm pour s'aligner sur la figure de mérite (figure 5). La cavité optique comprend 25 QW et des revêtements de 8 nm.

2.2.2 Structure du VCSEL

La structure VCSEL monomode suit la littérature établie et consiste en un substrat, une couche tampon, un premier DBR avec 35 périodes, une cavité optique avec 3 QWs et des barrières de confinement, une couche d'ouverture d'oxide, et un DBR supérieur avec 20 périodes.

2.2.3 Couplage de l'EAM et du VCSEL

La cavité optique du VCSEL produit une onde stationnaire dû aux réflexions entre les DBR, qui à son tour génère une onde stationnaire à l'intérieur de la cavité EAM. Un couplage très fort entre les cavités se produit lorsque le mode d'émission du VCSEL et le mode de l'EAM partagent précisément la même longueur d'onde. Il est possible de réduire le couplage en désaccordant les cavités, en modifiant l'épaisseur de l'une d'entre elles, ce qui entraîne un couplage modéré.

Un couplage fort entre les cavités VCSEL et EAM peut dégrader les performances en raison de réflexions arrière perturbatrices. Un couplage modéré à faible est plus favorable pour obtenir une fréquence de coupure de modulation plus élevée, comme l'ont démontré K. Panajotov et R. Schatz. Un couplage fort se traduit par une fonction de transfert de modulation décroissante, tandis qu'un couplage modéré maintient une réponse plate à mesure que la fréquence de modulation augmente.

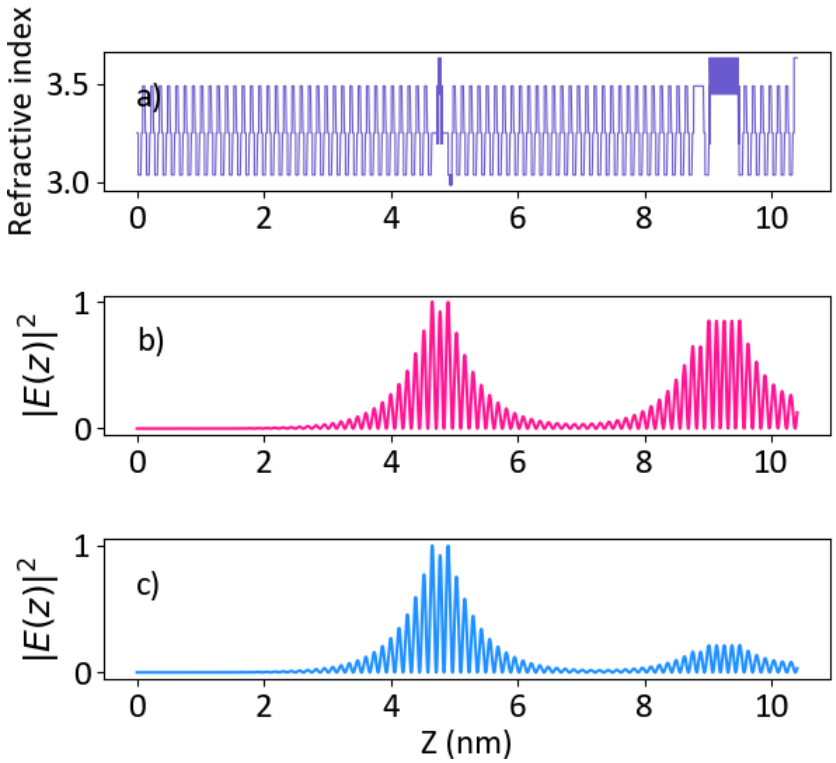

Figure 4: (a) Profil de l'indice de réfraction de la structure EAM-VCSEL avec le VCSEL au milieu et l'EAM à gauche ; distribution de la puissance optique le long du dispositif pour le mode composé de la cavité situé au premier plan dans la cavité du VCSEL pour un couplage fort (b) et modéré (c).

Une méthode pour diminuer le couplage entre les cavités VCSEL et EAM consiste à modifier l'épaisseur des couches de cladding aux extrémités de la cavité EAM afin d'obtenir un désaccord. Cela permet de contrôler les résonances Fabry-Perot et les modes des cavités. Un réglage précis pendant l'étape d'épitaxie est essentiel pour concevoir un dispositif avec un couplage faible à modéré, car un couplage excessif peut conduire à un comportement peu fiable du dispositif.

2.3 Conclusion

Dans ce chapitre, la conception et la modélisation de l'EAM-VCSEL ont été examinées dans le but d'améliorer ses performances RF. La configuration des puits quantiques (QW) et des barrières de confinement a été optimisée pour améliorer la profondeur de modulation de l'absorption et l'évacuation des porteurs de charge, améliorant ainsi le rapport de contraste de l'absorption. Deux nouvelles structures EAM-VCSEL ont été conçues, l'une d'entre elles incorporant une ouverture en oxyde pour un accord potentiel post-épitaxie. En outre, le couplage des cavités optiques a été etudié

pour obtenir un couplage faible à modéré entre les cavités pour un fonctionnement à haute fréquence. La phase suivante consiste à fabriquer le dispositif en veillant à ce que chaque étape corresponde aux objectifs de conception et de performance. Une attention particulière sera accordée au processus d'épitaxie et au maintien de l'intégrité structurelle.

3 Fabrication

La fabrication des EAM-VCSEL fait appel à des processus de fabrication de VCSEL classiques, mais certaines étapes spécifiques restent difficiles. La croissance épitaxiale de nombreuses couches nécessite un calibrage et un contrôle précis. Pour obtenir une émission monomode dans les VCSEL, il faut oxider avec précision une couche d'aluminium afin de créer une ouverture. Pour un fonctionnement à haute fréquence, le dispositif a aussi besoin d'un accès micro-ruban spécifique.

Le chapitre précédent a abordé les propriétés critiques des EAM-VCSEL et les améliorations de la conception, en soulignant l'importance d'une croissance épitaxiale précise. Ce chapitre se concentre sur le processus de fabrication, en visant la compatibilité avec les processus VCSEL standards tout en incorporant des étapes spécifiques pour traiter les propriétés uniques des EAM-VCSEL.

3.1 Epitaxie

3.1.1 Principe

La structure EAM-VCSEL est produite par épitaxie par jet moléculaires (MBE). Ce procédé consiste à diriger des jets moléculaires sur un substrat chauffé sous vide, ce qui permet la formation d'une couche cristalline. Le système MBE-412 de Riber est utilisé. Il comprend une chambre à ultravide, un porte-substrat et des cellules d'effusion dotées de clapets pour contrôler le flux de matériau. Les principaux processus de surface comprennent l'adsorption, la migration de surface, l'incorporation d'atomes dans le réseau cristallin et la désorption. Le système utilise différentes cellules pour le gallium et l'aluminium avec des taux de croissance variables pour obtenir la composition d'aluminium souhaitée. Le dopage de type N est obtenu par évaporation du silicium, tandis que le dopage de type p est obtenu par évaporation du tétrabromure de carbone (CBr_4). Le procédé MBE maintient une température de substrat d'environ $550°C$, avec des concentrations de dopage au silicium allant jusqu'à $1 \times 10^{19} at.cm^{-3}$ et des concentrations de carbone allant jusqu'à $1 \times 10^{20} at.cm^{-3}$.

3.1.1.1 Mesure de courbure

La courbure mesure l'écart d'une courbe ou d'une surface par rapport à une ligne droite ou une surface plane. Pour les surfaces courbes, la courbure est inversement proportionnelle à leur rayon, donc une ligne droite a une courbure nulle. Le contrôle de la courbure pendant l'épitaxie permet de vérifier l'uniformité du dépot dans le temps, de révéler la dérive en vitesse de croissance, et de déterminer si des effets de relaxation ont eu lieu. La courbure est mesurée en projetant une matrice de points sur la plaquette et en analysant leur distorsion de réflexion. Les mesures in situ en temps réel montrent l'évolution de la courbure au cours des différentes phases de croissance, avec des pentes cohérentes pour les DBR, ce qui indique une teneur en aluminium uniforme et l'absence de relaxation mécanique majeure.

3.1.2 Reflectometrie in-situ

Le bâti d'épitaxie subit un étalonnage des taux de croissance des cellules d'effusion avant de produire les structures réelles. Cet étalonnage implique la croissance d'un DBR de base et l'estimation de l'épaisseur des couches par cristallographie aux rayons X et par des algorithmes spécifiques. La réflectométrie est utilisée comme mesure in situ pour contrôler la réflectance de l'échantillon en cours de croissance. Elle permet de s'assurer que l'épitaxie en cours se déroule comme prévu, même si les modèles d'indice de réfraction pour l'AlGaAs à haute température ne sont pas bien établis. La comparaison des données de réflectométrie avec des mesures antérieures de structures similaires permet d'évaluer la résonance FP pendant l'épitaxie.

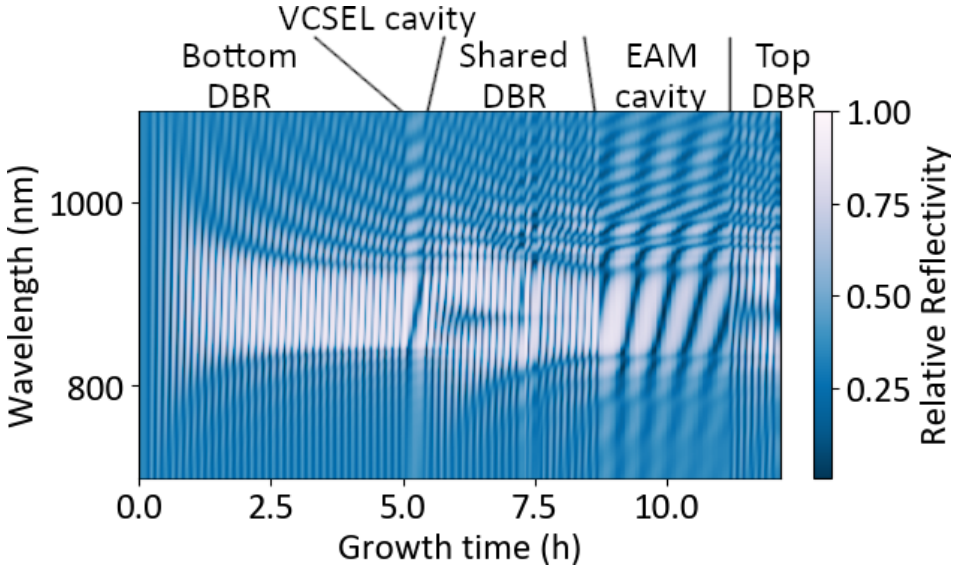

Figure 5: Réflectométrie in situ de l'EAM-VCSEL pendant l'épitaxie.

La réflectométrie du spectre complet en temps réel est utilisée pour surveiller les changements de réflectivité pendant l'épitaxie. Elle fournit des informations sur la longueur d'onde centrale du réflecteur de Bragg distribué (DBR) et permet de prédire la longueur d'onde de résonance de Fabry-Perot dans les cavités. En observant et en analysant la réflectivité du DBR, il est possible d'interrompre le processus d'épitaxie si la longueur d'onde centrale s'écarte de manière significative de la longueur d'onde cible. Ces informations peuvent guider une modification des taux de croissance, garantissant l'obtention de la résonance Fabry-Perot souhaitée.

Les résultats de l'épitaxie, les mesures in situ et leurs implications ont été présentés lors de la 22e conférence internationale sur l'épitaxie par faisceaux moléculaires (ICMBE 2022) [1].

3.2 Gravure du mesa

L'étape initiale après l'épitaxie consiste à graver le mesa de l'EAM, créant ainsi une structure. La partie supérieure du mesa est recouverte d'une couche de titane suivie d'une couche d'or, qui sert de contact supérieur. Une photolithographie de la résistance SPR700 est utilisée pour protéger l'intérieur du mesa. Lors de la gravure, les couches à enlever sont constituées d'AlGaAs avec une teneur en aluminium variable. Un contrôle in situ du processus de gravure est crucial pour éviter une gravure excessive qui pourrait entraver le contact électrique.

La réflectométrie est utilisée pour contrôler la gravure en temps réel, en surveillant les changements de réflectivité de la surface au fur et à mesure que les couches sont gravées. Le processus de gravure concerne le DBR supérieur et la cavité EAM, avec une vitesse de gravure d'environ 7 nm/s. La difficulté réside dans le fait que la couche de contact centrale est mince, seulement 170 nm, et qu'il est donc crucial d'arrêter la gravure dans une fenêtre très courte, environ 10 secondes, pour éviter d'endommager la couche. L'augmentation de l'épaisseur de cette couche, par exemple à 303,66 nm ou 425,12 nm, pourrait permettre un meilleur contrôle.

Dans la gravure ionique réactive par plasma à couplage inductif (ICP-RIE), la profondeur de gravure peut présenter une inhomogénéité en raison de facteurs tels que les variations du champ électrique, la géométrie de l'échantillon et les différences de température à travers l'échantillon. L'amélioration des températures de refroidissement peut aider, mais l'augmentation de l'épaisseur de la couche de contact est la solution la plus simple pour atténuer ce problème.

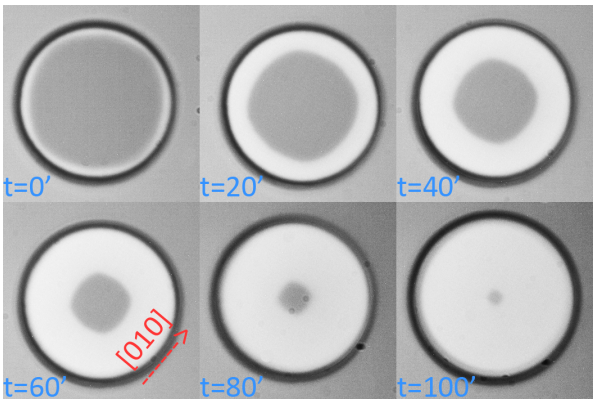

Figure 6: Vue de dessus de la création d'une ouverture d'oxyde en fonction du temps avec des intervalles de $20min$ de la mesa VCSEL.

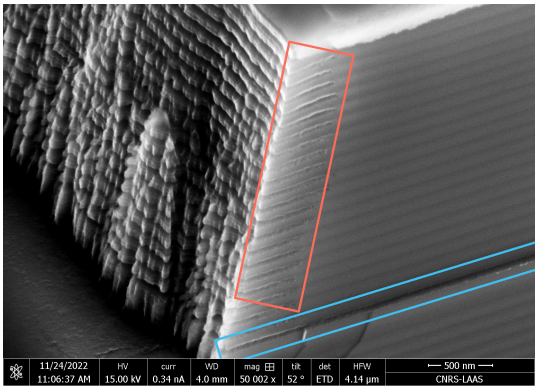

Figure 7: Coupe au faisceau d'ions focalisés d'une mesa oxydée.

3.3 Ouverture d'oxide du VCSEL

Pour une efficacité d'absorption optimale dans l'EAM-VCSEL, il est crucial d'obtenir une émission monomode. Pour ce faire, la lumière et les porteurs de charge sont confinés dans un diamètre étroit à l'aide d'une ouverture d'oxide. L'ouverture d'oxide, avec une fraction élevée d'aluminium $AlGaAs$, garantit une émission VCSEL monomode, essentielle pour une modulation efficace par électro-absorption.

Le taux d'oxidation est essentiellement sensible à deux paramètres : la fraction d'aluminium et la température d'oxydation. Le taux d'oxidation augmente de façon exponentielle avec la fraction d'aluminium. La vitesse d'oxidation est contrôlée par la température fixée dans le four. Toutefois, ce paramètre est difficile à contrôler, car le taux d'oxidation augmente de façon logarithmique avec la température.

Le processus d'oxidation est crucial mais difficile, et il est surveillé en temps réel à l'aide d'une méthode optique. Un four AET expose l'échantillon à des conditions spécifiques, notamment une pression de 500 mbar, un flux gazeux de N_2, H_2 et H_2O, et une température comprise entre 400 et 450°C. Le système de surveillance optique en temps réel observe l'oxidation en mesurant la variation de la réflectivité infrarouge dans la gamme de longueurs d'onde d'éclairage.

Les couches EAM absorbant les infrarouges, il est difficile de visualiser l'oxidation de l'ouverture dans le VCSEL. Pour remédier à ce problème, des structures de motifs spécifiques sont utilisées pour surveiller le taux d'oxidation dans le VCSEL. Le processus d'oxidation réduit le diamètre de l'ouverture de $67\mu m$ à $2\mu m$ à une vitesse moyenne de $570nm/min$.

La méthode d'inspection de l'ouverture de l'oxide à l'aide du FIB afin de la comparer à l'outil de visualisation in situ a été incluse dans une publication résultant d'une collaboration avec le doctorant, N. Monvoisin.

3.4 BCB et contacts micro-rubans

Pour les performances à haute fréquence des dispositifs EAM-VCSEL, des lignes micro rubans sont utilisées. Ces lignes nécessitent un matériau diélectrique plat pour les créer au même niveau que le mesa. Le benzocyclobutène (BCB) est utilisé à cette fin en raison de sa stabilité, de sa résistance à la chaleur et aux produits chimiques, et de sa compatibilité avec les applications à haute fréquence. Après avoir été enduit par centrifugation, le BCB doit être planarisé et gravé à la hauteur du mesa pour créer les lignes de transmission micro ruban.

Pour réaliser la planarisation du BCB, un outil de nano-impression, la presse à coussin d'air (ACP), est utilisé. Cette technique, qui présente plusieurs avantages par rapport aux méthodes traditionnelles, consiste à presser l'échantillon contre un moule à l'aide de couches de gaz ou de fluides conformables. L'utilisation d'une température et d'une pression contrôlées pendant le processus garantit que le BCB devient plus flexible pour une impression efficace tout en maintenant la compatibilité avec la photolithographie ultérieure. Cette technique de planarisation réduit considérablement les irrégularités de surface du mesa, qui passent d'environ $4\mu m$ à environ $50nm$.

Après la planarisation, des vias sont créés à travers le BCB pour permettre à la ligne microruban d'atteindre le plan de masse métallique. Le BCB, qui est un matériau photorésistant négatif, est modelé par photolithographie. Le BCB est isolé puis développé à l'aide d'un processus sensible, où la température joue un rôle critique. Si les vias ne sont pas complètement ouverts, un processus supplémentaire est appliqué. Il s'agit d'une gravure au plasma du BCB à l'intérieur des vias tout en le protégeant ailleurs à l'aide d'un matériau photorésistant différent. Un contrôle minutieux du temps de gravure permet de s'assurer que les vias sont complètement ouverts, révélant le plan de masse et ne laissant aucune trace de contamination par le BCB.

L'utilisation d'un plasma de tétrafluorométhane CF_4 pour graver le SiO_x peut entraîner la formation d'un contaminant orange sur les contacts métalliques. Pour nettoyer ce contaminant, un plasma de CHF_3 est utilisé pour la gravure du SiO_x, et un plasma de O_2 pur est employé pour enlever complètement le dépôt orange, tout en protégeant l'échantillon avec une cage métallique. Malgré les craintes que le plasma de O_2 puisse graver le BCB, les procédures du fabricant confirment que le BCB est insensible au O_2 pur en termes de gravure.

3.5 Processus de fabrication

Au cours de la première étape du processus, du métal est déposé sur la couche de contact de l'EAM pour l'accès au signal RF et sert de masque pour la gravure au plasma. Les étapes clés comprennent le nettoyage de l'échantillon à l'acétone, suivi d'un rinçage à l'isopropanol et d'un séchage. L'étape de photolithographie consiste à appliquer la résine LOR30B et la résine photosensible SPR700, en créant une contre-dépouille pour une meilleure pénétration des solvants. L'étape de métallisation comprend la désoxidation de l'échantillon, le dépôt de titane et d'or et l'utilisation de l'évaporation par faisceau d'électrons. Enfin, le processus de décollement du métal consiste à utiliser du DMSO chauffé pour dissoudre la résine LOR30B.

Le premier mesa est ensuite gravé jusqu'à la couche de contact centrale entre l'EAM et le VCSEL. Les étapes clés comprennent le nettoyage de l'échantillon, une étape de photolithographie pour protéger les zones de la gravure, et la gravure au plasma de la mésa de l'EAM à l'aide d'un mélange de gaz composé de Cl2 et de N2, jusqu'à ce que la couche de contact médiane soit atteinte, avec une détection du point final pour garantir la précision.

Le métal est déposé sur la couche de contact centrale sous la forme d'un anneau entourant le mesa EAM. Il est utilisé comme contact métallique, mais aussi comme masque pour la gravure du deuxième mésa (VCSEL). Les diamètres des mesa des VCSELs varient de 67 à 71.

Le mésa EAM est passivé par un dépôt de SiO_x, suivi d'une gravure au plasma du second mésa. Les étapes clés comprennent le nettoyage de l'échantillon, le dépôt de SiO_x, la photolithographie, la gravure au plasma de SiO_x, la gravure au plasma du deuxième mésa et la création de l'ouverture d'oxide.

Nous nous concentrons ensuite sur la création d'un plan de masse sous les plots haute fréquence pour permettre un accès efficace au microruban. Cela implique le dépôt d'une couche de SiO_x, la photolithographie et la gravure au plasma qui s'ensuit. La couche de SiO_x assure l'isolation et la connexion du plan de masse.

Du métal est déposé pour établir un contact avec le plan de masse. Le motif métallique est en contact avec l'anneau déposé dans la deuxième métallisation, qui est le contact central dans le DBR partagé. En dehors de cet anneau, le motif métallique repose sur le SiO_x pour éviter tout court-circuit avec la cavité du VCSEL.

La phase suivante consiste à préparer le dispositif EAM-VCSEL pour un fonctionnement à haute fréquence avec des sondes RF en mettant en œuvre un accès microruban. Elle nécessite l'utilisation d'une passivation en benzocyclobutène (BCB) pour le matériau diélectrique, qui doit être planarisé.

Il s'agit ensuite de durcir le matériau BCB utilisé pour l'accès microruban en le soumettant à un processus de recuit. Cette étape est cruciale pour améliorer la résistance mécanique et les propriétés électriques du matériau.

L'étape suivante consiste à graver les couches BCB et SiO_x afin d'ouvrir complètement les vias et d'en retirer les restes de matériau BCB. Elle permet également d'éliminer le SiO_x de la partie supérieure du mesa EAM, qui pourrait obstruer la fenêtre d'émission.

La dernière étape consiste à déposer les accès micro rubans.

3.6 Conclusion

Dans ce chapitre, le processus de fabrication d'un EAM-VCSEL a été décrit, en mettant l'accent sur les détails spécifiques à ce dispositif. La phase d'épitaxie a été réalisée grâce à une méthode combinant des mesures de réflectivité in situ pour corriger le taux de croissance de la cellule, ce qui a permis d'améliorer la précision du réglage.

L'oxidation d'une couche à forte fraction d'aluminium a été réalisée avec succès, ce qui a permis d'obtenir une ouverture d'oxide idéale pour le VCSEL. Le processus a été suivi à l'aide d'une technique de mesure in situ, et la gravure par FIB a confirmé l'alignement entre l'ouverture d'oxide visualisée et l'ouverture réelle.

Des améliorations ont été apportées à l'étape de conditionnement du BCB, notamment en améliorant le processus de nanoimpression pour une meilleure adhérence et une plus grande durabilité de l'accès métallique microruban, tout en conservant la sensibilité à la photolithographie. Les processus de gravure au plasma ont également été affinés pour minimiser la contamination pendant la gravure du BCB.

L'obtention d'un réglage optimal pendant le processus d'épitaxie s'est avérée difficile et sensible aux variations de l'épaisseur de la couche. Une méthode de réglage pendant la croissance épitaxiale a été mise au point, impliquant la modification des taux de croissance des cellules guidée par des mesures in situ.

Le chapitre a mis l'accent sur la nécessité de caractériser les performances du dispositif, de le comparer aux VCSELs standard et de valider les choix de conception par des caractérisations électriques et des tests à haute fréquence.

4 Caractérisation

Dans les chapitres précédents, nous nous sommes concentrés sur l'amélioration de la largeur de bande de l'EAM-VCSEL par le biais d'améliorations de la conception, en abordant en particulier les défis liés au couplage de la cavité et à la performance à haute fréquence. Nous avons également souligné l'importance du processus de croissance épitaxiale pour obtenir le couplage souhaité et optimiser la structure EAM pour une modulation efficace de l'absorption à haute fréquence.

Ce chapitre se concentre sur la caractérisation complète de l'EAM-VCSEL fabriqué. Nous examinons les caractéristiques opérationnelles statiques et à haute fréquence de ces composants.

4.1 Fonctionnement à haute fréquence

4.1.1 Configuration experimentale

Du côté électrique, un analyseur de réseau vectoriel (VNA Agilent PNA-X) génère l'onde de puissance RF, et une unité d'alimentation (PSU) fournit une polarisation inverse constante à l'EAM. Ces signaux sont combinés à l'aide d'un T de polarisation et connectés aux pointes RF Cascade Microtech Z67-XVF-GSG-150 sur l'accès à l'EAM.

Du côté optique, un laser accordable (Superlum Broad Sweeper 840-1) émet de la lumière dans l'EAM. Le faisceau laser est transmis par des fibres optiques, un coupleur 50-50 et fini par arriver dans une photodiode (Newfocus 1014 $45GHz$ $0.25A/W$). La sortie électrique de la photodiode est connectée au VNA.

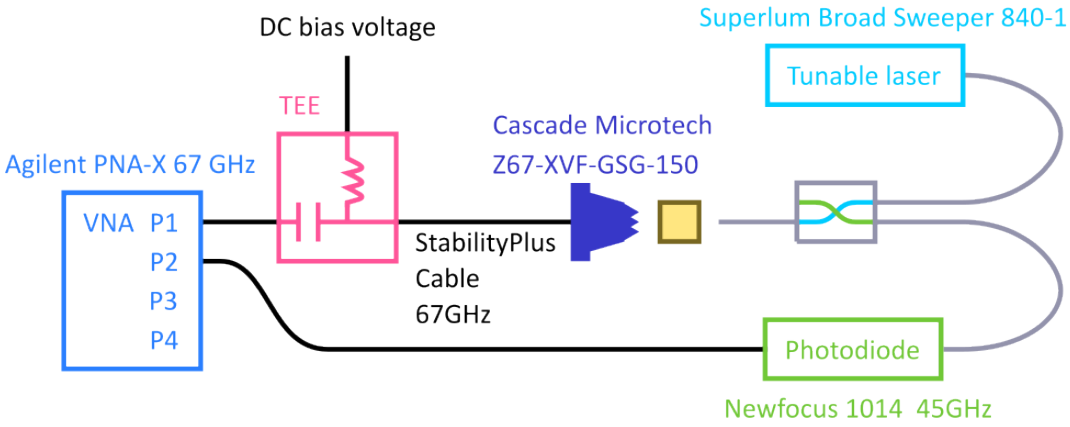

Figure 8: Schéma de la caractérisation électro-optique de l'EAM avec un VNA et une injection laser externe.

Lors de la caractérisation du modulateur, la lumière laser externe est introduite via une fibre optique et un coupleur optique 50-50, avec plusieurs pertes optiques dans l'installation. Le laser généré à $4mW$ subit des réductions de puissance à différentes interfaces, y compris le coupleur, ce qui donne une puissance finale de $220\mu W$ à la photodiode.

Un étalonnage de la puissance est effectué pour régler le signal du VNA à $0dBm$. Pour éliminer les contributions des câbles et des pointes dans la mesure des paramètres S du dispositif, des étalonnages de circuit ouvert, de court-circuit et de charge sont effectués aux extrémités du câble et de la pointe à l'aide de kits d'étalonnage et d'algorithmes spécifiques.

Pour aligner précisément la fibre optique avec le modulateur à électro-absorption (EAM), une fibre optique dont le cœur est exposé est utilisée pour la transmission de la lumière. Pour trouver la position d'alignement optimale, le laser émet de la lumière tandis qu'une tension continue est appliquée en inverse (environ $-6V$ pour un courant maximal). La polarisation de l'EAM augmente l'absorption des photons, ce qui se traduit par un courant plus élevé. L'alignement est déterminé en balayant méticuleusement la fibre optique le long des axes x, y et z tout en surveillant le photocourant. Le meilleur alignement est atteint lorsque le courant maximal est atteint, typiquement autour de $300\mu A$ ou $0.66mW$.

4.1.2 Contexte de la caractérisation RF des EAM-VCSEL

Lors de la caractérisation d'un quadripôle dont l'impédance est adaptée à son accès, nous disposons d'une puissance et d'une tension de polarisation connues et constantes. Dans notre configuration EAM-VCSEL, la puissance appliquée est initialement constante lorsque l'impédance de charge est de 50Ω. Cependant, une fois connectée à l'EAM, l'impédance varie avec la fréquence, ce qui entraîne une fluctuation de la tension. Pour caractériser précisément l'EAM, nous supprimons les contributions des pointes RF, établissons les paramètres S des pointes RF et extrayons la fonction de transfert de l'EAM en fonction de sa tension à petit signal V_{eam}.

Le port 1 du VNA est connecté à l'EAM comme suit : Port 1 → câble → pointe RF → EAM. De l'autre côté, le port 2 du VNA est directement connecté à la sortie 50Ω de la photodiode.

Pour caractériser correctement l'EAM, il est essentiel d'établir un plan de référence à la sortie des pointes. Comme les pointes ne peuvent être connectées qu'au port 1, une méthode est nécessaire pour reconstruire les paramètres S sur la base d'une série de mesures à un port. Cette approche implique l'utilisation de circuits auxiliaires tels que des circuits ouverts, des courts-circuits et une charge de 50Ω. Ensuite, les paramètres

S sont calculés à l'aide de la méthode de réduction des ports.

4.1.3 Caractérisation EAM à haute fréquence

On notera que la caractérisation en statique a révélé un couplage fort entre le VCSEL et l'EAM empêchant l'émission laser du VCSEL, et un la présence d'un contact Schottky.

Les fonctions de transfert de tension ont été mesurées à différentes polarisations de tension continue, la meilleure largeur de bande étant obtenue avec une polarisation de $-6V$. Lorsqu'elle est normalisée, la fonction de transfert de tension atteint $-3dB$ à $47GHz$, ce qui indique une largeur de bande accrue de $18GHz$ par rapport aux résultats précédents.

Les fonctions de transfert de tension présentent quelques irrégularités, avec des creux et des pics mineurs dans la bande passante. Ces variations sont probablement corrélées avec des paramètres spécifiques de l'EAM-VCSEL. La compréhension de ces irrégularités et l'aplanissement de la bande passante nécessiteraient des simulations complètes, éventuellement à l'aide de modèles analytiques et de simulations par la méthode des éléments finis.

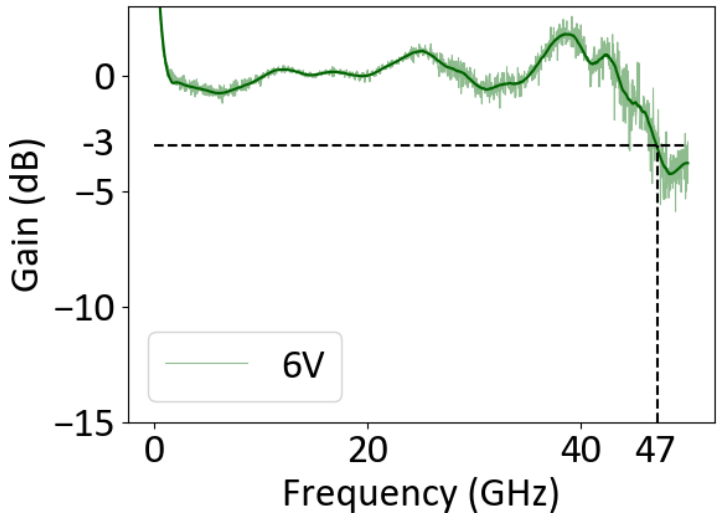

Figure 9: Fonction de transfert en tension de l'EAM avec une polarisation de 6V.

Le dispositif de mesure de l'EAM-VCSEL peut être amélioré de plusieurs façons. Tout d'abord, en fixant la fibre optique de manière plus efficace afin de minimiser la sensibilité des mesures à des changements de position mineurs. Une prise plus stable et plus courte pour la fibre pourrait contribuer à atténuer ces problèmes.

Le coupleur 50-50 dans l'installation introduit des pertes significatives, supérieures

à $6dB$. Il est recommandé de le remplacer par un circulateur optique à trois ports pour améliorer les caractérisations EAM. Dans un scénario idéal, un VCSEL fonctionnant correctement ne nécessiterait pas d'injection laser externe, de coupleur ou de circulateur.

La largeur de bande limitée de la photodiode ($3dB$ à $45GHz$) limite les performances de l'EAM, qui peut atteindre $47GHz$. Pour obtenir une estimation plus précise de la largeur de bande de l'EAM, il est suggéré de caractériser la réponse en fréquence de la photodiode et de normaliser les mesures de l'EAM avec ces données, bien que cela puisse introduire du bruit à des fréquences plus élevées.

4.2 Conclusion

Dans ce chapitre, diverses caractérisations et mesures du dispositif EAM-VCSEL ont été effectuées, sur la base des processus de conception et de fabrication. Parmi les difficultés rencontrées, citons le couplage fort et constant de la cavité empêchant l'émission de l'effet laser et un comportement Schottky dans le contact central métallique en raison d'un dopage insuffisant.

Sur le plan positif, l'EAM a présenté d'excellentes performances à haute fréquence, avec une bande passante de 47 GHz, dépassant les précédents records de l'EAM-VCSEL. D'autres améliorations de la caractérisation à haute fréquence ont été recommandées, comme la prise en compte de la bande passante de la photodiode et l'amélioration de l'injection laser.

Les caractéristiques du dispositif s'approchent des niveaux de performance des derniers développements VCSEL. Pour effectuer une comparaison plus complète avec les concurrents, des caractérisations impliquant des méthodes d'encodage avancées sont envisageables.

En relevant les défis et en apportant des améliorations au couplage des cavités, aux contacts métalliques et aux configurations optiques, la configuration EAM-VCSEL offre la possibilité d'atteindre des largeurs de bande encore plus élevées à l'avenir. Avec ses performances actuelles et ses possibilités d'amélioration, elle a le potentiel de répondre aux récents besoin des centres de données et HPCs.

5 Conclusion et perspectives

La demande d'un accès plus rapide aux données, motivée par des facteurs tels que la télévision 4K, la vidéoconférence, le travail à distance et les jeux vidéos, a conduit à la croissance des centres de données et de l'informatique à haute performance. Les

VCSELs traditionnels ont été largement utilisés dans ces applications, mais leur bande passante est limitée à environ 35 GHz en raison de la dynamique des porteurs de charge.

Pour remédier à cette limitation et augmenter la bande passante, une nouvelle approche consiste à séparer les fonctions d'émission et de modulation de la lumière à l'aide de modulateurs d'électro-absorption (EAM). L'EAM-VCSEL combine ces fonctions en un seul dispositif, offrant une intégration pratique comme les VCSELs tout en atteignant une bande passante EAM théorique supérieure à 100 GHz. Cette technologie vise à répondre à la demande croissante de débits de données plus élevés dans les centres de données et autres applications.

L'approche de la thèse a commencé par une conception EAM-VCSEL existante avec une bande passante de 30 GHz. La conception a été améliorée par des simulations analytiques afin d'améliorer la dynamique des porteurs de charge, de maximiser la profondeur de modulation de l'absorption et d'aborder le couplage de la cavité optique. Le processus de fabrication a été affiné par des mesures in situ pendant l'épitaxie, ce qui a permis d'obtenir des structures plus proches de la longueur d'onde ciblée de 850 nm. Le suivi in situ de l'oxidation du VCSEL a été validé en utilisant la gravure FIB. Des améliorations ont été apportées à la passivation des mesas, au packaging BCB et à la gravure au plasma.

Les caractérisations RF ont été considérablement améliorées grâce à une photodiode à large bande passante de 850 nm, à un meilleur alignement des fibres et à une configuration d'analyse RF de 67 GHz. La fonction de transfert en tension a été extraite pour mieux représenter les capacités de haute impédance de l'EAM.

Ce travail de thèse a rencontré plusieurs limites qui offrent des possibilités d'améliorations futures. L'obtention d'un couplage idéal pendant la croissance épitaxiale a été difficile en raison des incertitudes et de la dérive de l'étalonnage du taux de croissance. Pour améliorer cela, un modèle d'indice de réfraction pour $AlGaAs$ à la température d'épitaxie, couplé à une surveillance de la réflectivité in-situ, peut affiner l'étalonnage de la cellule d'effusion.

Des difficultés ont été rencontrées lors de la gravure au plasma des mesas, entraînant des profondeurs de gravure inégales. L'optimisation des conditions de gravure et l'augmentation de l'épaisseur de la couche de contact intermédiaire pourraient contribuer à résoudre ce problème.

Bien que le dispositif de caractérisation RF ait été amélioré, d'autres améliorations sont possibles, notamment la normalisation des mesures en fonction de la réponse de la photodiode, l'utilisation d'un circulateur au lieu d'un coupleur et l'exploration de formats d'encodage complexes tels que le PAM-4.

Pour optimiser la conception de l'EAM-VCSEL et les caractérisations RF, des sim-

ulations plus complexes devraient être effectuées, en explorant diverses conceptions de puits quantiques multiples (MQW) et en simulant l'impédance de l'EAM.

Malgré ces difficultés, l'EAM-VCSEL est prometteur avec une bande passante de 47 GHz, compétitive par rapport à d'autres technologies. Ses capacités intégrées d'émission de lumière et d'absorption optique le rendent facile à déployer, en particulier dans les zones où le VCSEL est déjà établi. Les résultats de ce travail indiquent un potentiel important d'amélioration des performances.